ABSTRACT

EXPERIMENTAL AND NUMERICAL CHARACTERIZATION OF MULTIPHASE SUBSURFACE OIL RELEASE

by
Feng Gao

Subsurface oil release is commonly encountered in the natural environment and engineering applications and has received the substantial attention of researchers after the disastrous Deepwater Horizon Blowout oil spill in 2009. The main focus on the present research is to systematically study the hydrodynamics of underwater oil jet under a variety of conditions, including the effect of dispersant and different gas to oil ratios (GOR) by using experimental measurement as well as a Computational Fluid Dynamics (CFD) approach, from which the measured turbulent characteristics (e.g., velocity, turbulent kinetic energy, turbulence dissipation rate, etc.) of underwater oil jet are thoroughly examined and compared. A Lagrangian Particle Tracking Model that coupled with CFD data is used to simulate the trajectories and movement of individual oil droplets under the effect of turbulence and comprehensive physical forces. The trajectories of oil droplets can be very different depending on the droplet diameter and physical force condition, which may bring insight into understanding the fate of oil droplets after the oil release. Large Eddy Simulation (LES) suggests that the oil and gas jet in the Deepwater Horizon Blowout can be churn rather than bubbly, which provides new perspectives on the estimation of the total oil flow rate during the blowout as well as the evaluation of dispersant effectiveness. Furthermore, a laboratory scale multiphase jet experiment by using Particle Imaging Velocimetry (PIV) as well as CFD simulation is conducted to understand and compare the

hydrodynamics between the bubbly and churn jets, which shows that the churn jet may result in more entrainment from the ambient environment compared with the bubbly jet.

EXPERIMENTAL AND NUMERICAL CHARACTERIZATION OF MULTIPHASE SUBSURFACE OIL RELEASE

by
Feng Gao

A Dissertation
Submitted to the Faculty of
New Jersey Institute of Technology
in Partial Fulfillment of the Requirements for the Degree of
Doctor of Philosophy in Mechanical Engineering

Department of Mechanical and Industrial Engineering

December 2018

APPROVAL PAGE

EXPERIMENTAL AND NUMERICAL CHARACTERIZATION OF MULTIPHASE SUBSURFACE OIL RELEASE

Feng Gao

Dr. Michel Boufadel, Dissertation Advisor — Date
Professor of Civil and Environmental Engineering, NJIT

Dr. I. Joga Rao, Co-Dissertation Advisor — Date
Chair and Professor of Mechanical and Industrial Engineering, NJIT

Dr. Pushpendra Singh, Committee Member — Date
Professor of Mechanical and Industrial Engineering, NJIT

Dr. Zhiming Ji, Committee Member — Date
Professor of Mechanical and Industrial Engineering, NJIT

Dr. Richard Miller, Committee Member — Date
Associate Professor of Mechanical Engineering, Clemson University

BIOGRAPHICAL SKETCH

Author: Feng Gao

Degree: Doctor of Philosophy

Date: December 2018

Undergraduate and Graduate Education:

- Doctor of Philosophy in Mechanical Engineering,
  New Jersey Institute of Technology, Newark, NJ, United States, 2018

- Master of Science in Mechanical Engineering,
  Clemson University, Clemson, SC, 2014, United States, 2018

- Bachelor of Science in Mechanical Engineering,
  Dalian University of Technology, Dalian, People's Republic China, 2012

Major: Mechanical Engineering

Presentations and Publications:

Gao, F., Shoai Naini, S., Wagner, J., and Miller, R., 2017, An experimental and numerical study of refrigerator heat leakage at the gasket region: International Journal of Refrigeration, v. 73, no. Supplement C, p. 99-110.

Gao, F., Zhao, L., Boufadel, M. C, Robinson, B., and Miller, R., 2017, Hydrodynamics of oil jets without and with dispersant: Experimental and numerical characterization: Applied Ocean Research, v. 68, p. 77-90.

Zhao, L., Gao, F., Boufadel, M., King, T., Robinson, B., Lee, K., and Conmy, R., 2017, Oil jet with dispersant: Macro-scale hydrodynamics and tip streaming: AIChE Journal, v. 63, no. 11, p. 5222-5234.

Boufadel, M., Gao, F., Zhao, L., Özgökmen, T., Miller, R., King, T., Robinson, B., Lee, K., and Leifer, I., 2018, Was the DeepWater Horizon well discharge churn flow? Implications on the estimation of the oil discharge and droplet size distribution: Geophysical Research Letters, v. Accepted.

Zhao, L., Boufadel, M. C., King, T., Robinson, B., Gao, F., Socolofsky, S. A., and Lee, K., 2017, Droplet and bubble formation of combined oil and gas releases in subsea blowouts: Marine Pollution Bulletin, v. 120, no. 1, p. 203-216.

Golshan, R., Boufadel, M., Rodriguez, V., Geng, X., Gao, F., King, T., Robinson, B., and Tejada-Martínez, A., 2018, Oil droplet transport under non-breaking waves: An Eulerian RANS approach combined with a Lagrangian particle dispersion model: Journal of Marine Science and Engineering, v. 6, no. 1, p. 7.

Zhao, L., Shaffer, F., Robinson, B., King, T., D'Ambrose, C., Pan, Z., Gao, F., Miller, R. S., Conmy, R. N., and Boufadel, M. C., 2016, Underwater oil jet: Hydrodynamics and droplet size distribution: Chemical Engineering Journal, v. 299, p. 292-303.

Gao, F., Zhao, L., Shaffer, F., Golshan, R., Boufadel, M., King, T., Robinson, B., and Lee, K., 2017, Prediction of oil droplet movement and size distribution: Lagrangian method and VDROP-J model International Oil Spill Conference Proceedings, v. 2017, no. 1, p. 1194-1211.

Gao, F., Zhao, L., Shaffer, F., Golshan, R., Boufadel, M., King, T., Robinson, B., and Lee, K., 2017, CFD simulation of the behavior of droplet rising in water column with the effect of surfactant. International Oil Spill Conference Proceedings: May 2017, v. 2017, no. 1, p. 2017289.

Zhao, L., Gao, F., Boufadel, M. C., King, T., Robinson, B., and Lee, K., 2017, Effects of tip streaming on the prediction of droplet size distribution in the presence of dispersants during subsea blowouts: International Oil Spill Conference Proceedings, v. 2017, no. 1, p. 1212-1229.

Special dedication to parents and grandparents,
who love and support me unconditionally all the time.

謹以此論文獻給我的青春
我的父母高佩全朱淑平
我最親密的朋友吳少亘

ACKNOWLEDGEMENT

I would like to express my sincere gratitude to Dr. Michel Boufadel, who patiently instructed me during my Ph.D. research. Dr. Boufadel is a very passionate person that devotes himself to research to make a difference in his field, which inspired me greatly during my Ph.D. study. Meanwhile, he unconditionally supported me to chase my career goal with great understanding and advice.

I am also very grateful to my committee members: Dr. I. Joga Rao, Dr. Pushpendra Singh, Dr. Zhiming Ji and Dr. Miller for reading my thesis and giving insightful suggestions with their expertise.

I would like to thank my colleagues and friends at the Center for Natural Resources (CNR): Dr. Lin Zhao, Dr. Fangda Cui, Wen Ji, Hamed Behzad, Brian Wartell and Marilyn Quiles, who make an awesome research team in providing support and help when I am needed it.

I would like to thank my parents, Peiquan Gao and Shuping Zhu, who are very supportive of my going to the United States for the graduate program and always encourage me in time of challenges and difficulties. I also would like to acknowledge my friend/roommate, Shaogen Wu; I sincerely appreciate the time and fun we had.

TABLE OF CONTENTS

TABLE OF CONTENTS
(Continued)

Chapter **Page**

LIST OF TABLES

LIST OF FIGURES
(Continued)

Figure **Page**

LIST OF FIGURES
(Continued)

LIST OF FIGURES
(Continued)

Figure **Page**

LIST OF FIGURES
(Continued)

Figure **Page**

97

LIST OF FIGURES
(Continued)

Figure **Page**

LIST OF FIGURES
(Continued)

Figure **Page**

LIST OF FIGURES
(Continued)

Figure **Page**

LIST OF FIGURES
(Continued)

Figure **Page**

LIST OF FIGURES
(Continued)

Figure **Page**

CHAPTER 1

INTRODUCTION

1.1 Significance of Studying Subsurface Oil and Gas Release

A jet is liquid discharge dominated by momentum force from an orifice into a flow of similar flow characteristics. Similar to a jet, a plume is introduced by the potential energy source that provides buoyancy forces with respect to the surrounding environment. Many buoyant jets are discharged from the orifice driven by momentum and finally evolve into plumes as distant away from the orifice.

The research of jets and plumes dates back to early 20th century, during which time people showed significant interests in understanding turbulent flow, ever since then, there is a number of related research performed focusing on various aspects of theoretical, experimental and numerical methods of studying turbulent jets and plumes.

Most of the heavily studied field in the turbulent jet is in the combustion engine in automotive and aerospace engineering. The jet is injected into the combustion chamber that subjected to high pressure and temperature with the injection nozzle diameter of a few millimeters and high injection speed. Although the turbulent jets in combustion engines is the main stream of jet study, jets and plumes are commonly encountered in other natural systems and engineering application, such as underwater hydrothermal-vents (Norman and Revankar, 2010), wastewater discharge from outfalls (Hunt et al., 2010), oil-leakage/blowout during off-shore drilling (Chen and Yapa, 2004a), production and transportation (Bosanquet et al., 1961) with the development of modern technology and the high demand of petroleum energy. As the underwater environment is in the complicated

physical and chemical condition, there is even more possibilities of minor oil release due to metal corrosion and wear in the transportation system. There is not much literature available for subsurface (in water) oil jet release until the very recent incident of the Deepwater Horizon oil spill in 2010. The crude oil blowout from the riser at more than 2000 m down the sea surface has caused the spillage of more than 200 million gallons of crude oil into the Gulf of Mexico for a total of 87 days, making it the biggest oil spill in U.S. history (NRC, 2003, 2013; Ramseur, 2010). Moreover, the incident makes people realize the importance of understanding the oil jet release from the underwater condition with respect to oil mitigation and oil spill prevention. The subsurface oil release is complex in nature as it involves the immiscible multiphase flow of energy mixing, oil droplet breakup and coalescence, and surrounding water entrainment such that it requires the collaborative and interdisciplinary understanding in various subject fields.

1.2 Literature View of Research of Subsurface Jet

1.2.1 Overview of Turbulent Jet

This chapter reviews the main and the latest research on turbulent jets and plumes. The aim of this chapter is to provide a unified fundamental and research progress on the turbulent jet and define the methodology of researching the subsurface oil release.

Most of the jets in engineering applications are in turbulent flow regime with a Reynold number larger than 3000 (Pope, 2000). The turbulent jet along the axial distance can be classified into three regions: the near field region, intermediate field region, and the far-field region, as indicated in Figure 2.1. When the jet is initially released from the orifice, there is a region with almost uniform velocity in the radial direction, known as the potential

core, whose length decreases with increasing Reynold number (Sivakumar et al., 2012). The length of the near field region is usually within $\frac{x}{D} < 7$ (where x is the distance from the orifice along the jet centerline and D is the jet orifice diameter). The near field region is where the turbulent flow starts to develop and the initial condition (such as the geometry of the orifice) of the turbulent jet has a significant influence on the flow development in the near field region. The impact of the jet initial condition is alleged to disappear as the flow goes further downstream, however, the recent research claimed that the jet initial condition has an impact on the entire flow development process (Ball et al., 2012).

Turbulent jet reaches far field region at $\frac{x}{D} > 70$, where the turbulent flow is fully-developed with self-preserving behavior exhibited, which indicates that the flow structure is independent of the initial condition at the jet source while only determined by the local change of the length and velocity scale (Versteeg and Malalasekera, 1996), shown as follows:

$$\frac{\mathrm{u}}{U_{\max}} = f(\frac{y}{b}) \tag{1.1}$$

where u is the local velocity in the radial direction, $U_{\max}$ is the maximum mean velocity at a distance of x downstream of the jet orifice along the centerline, y is the distance in the radial direction from the centerline and b is half-width (the location where the local velocity is half of the mean velocity at the centerline). Self-preserving also indicates that any flow characteristics, such as turbulent intensity and Reynold stress, can be written as a function of local velocity and length scale, which follows a similar relationship to Equation (1.1). Meanwhile, the turbulent jet in the far-field region, whose axial velocity follows a Gaussian

profile, can be considered as isotropic (no directional preference) as most anisotropic large eddies already cascade into smaller eddies in the far-field region where the flow is fully-developed.

The transitional region, where $30 < \frac{x}{D} < 70$, is the least researched flow region for the turbulent jet (Ball et al., 2012). In this region, the turbulent jet is highly anisotropic (with directional preference) and the new large eddies generated via pairing strongly interact with one another. The transitional region of the turbulent jet is mainly governed by large scale flow fluctuations due to instability, however, the influence of cascaded small scale eddies is increasingly significant as going further downstream until reaching the fully-developed region (Yamashita et al., 1996).

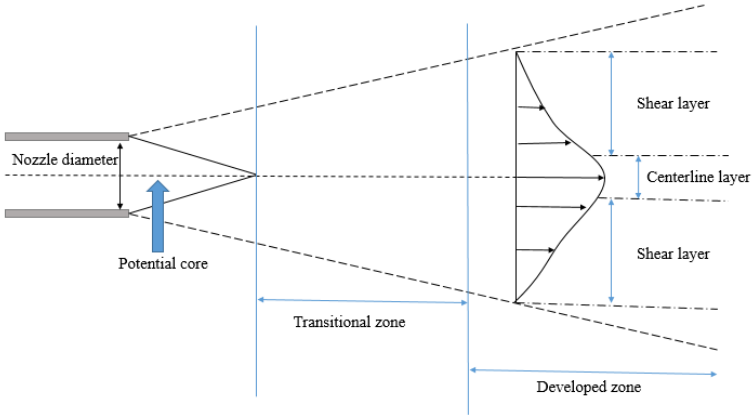

Figure 1.1 Schematic view of the turbulent jet released from a round orifice with the potential core, transitional zone, and the developed zone.

The subsurface oil/gas release is an inherently buoyant jet and has the behavior of plume as well. Most oil/gas is initially released at the orifice with momentum flux dominant as turbulent jet, however, with some distances (either horizontal or vertical), the jet gradually loses momentum flux and the plume-like characteristics are developed due to the

buoyancy flux. If given a distance large enough, all buoyant jet finally develop into the plume, therefore, the subsurface oil/gas flow release is a combination of buoyant jet and plume.

For most subsurface gas/oil release, the buoyant jet released at the orifice rapidly evolves into plume dominated by buoyancy flux. The transition length (e.g., the distance from the orifice to the transition point), L_M, can be estimated as follows (Fabregat et al., 2015):

$$L_M = M_o^{3/4} B_o^{-1/2} \tag{1.2}$$

where M_o is momentum flux and B_o is buoyancy flux. L_M is usually a few diameters in length for the most buoyant jet (Rodi, 1982).

In modeling the subsurface oil/gas release, the Gaussian profiles are usually assumed for calculating the buoyant jet velocity and oil/gas holdup (e.g., oil and gas volume fraction). The local jet velocity and oil/gas holdup as a function of the distance from the orifice (z) and radial distance from the centerline (r) are normally written as (Olsen and Skjetne, 2016):

$$\mathrm{u(z,r)} = \mathrm{u_c}(z) e^{-r^2/b^2} \tag{1.3a}$$

$$\phi(\mathrm{z,r}) = \phi_{\mathrm{c}}(z) e^{-r^2/\lambda^2 b^2} \tag{1.3b}$$

where u_c and ϕ_c are the centerline velocity and holdup, respectively. b is the half-width, which is the distance from the centerline of the jet where the local velocity is reduced to half of the centerline velocity. The parameter λ <1 determines the relative width of the velocity distribution versus the oil/gas distribution.

The experimental study of turbulent jet largely depends on the utilization of accurate devices to measure flow velocity. The major experimental methods for measuring turbulent jet can be classified into two categories: intrusive and non-intrusive methods. The intrusive method places a probe and wire in the jet/plume to measure the instantaneous velocity. The typical intrusive method based velocity measurement instruments are hot wire anemometry and Acoustic Doppler Velocimetry (ADV) and the typical non-intrusive method based velocity measurement instrument is Particle Imaging Velocimetry (PIV).

The hot wire anemometry is popularly used in studying turbulent jet in the 1960th. The hot wire anemometry is usually consisted of two metal probes with a thin string to let the electric current to go through such that the flow velocity can be estimated by converting the proportional energy loss at the thin string through heat convection (Lomas, 2011). The advantages of hot wire anemometry include low cost, high response frequency, and good spatial and temporal resolution while the main disadvantage of hot wire anemometry lies in its incapability of measuring high turbulence intensity due to the fragileness of the thin string. Meanwhile, the thin string is easy to be contaminated by the impurities in the turbulent flow such that the accuracy deteriorates over the time of turbulent jet flow measurement.

The principle of Acoustic Doppler Velocimetry (ADV) is based on the Doppler shift effect, whose working principle is sending out a short acoustic pulse from the transmit

element and the acoustic echo is recorded by the receiver elements when the pulse travels through the receiver beams, and the Doppler shift is processed to determine the turbulent flow velocity. Seeding particles must be added for the ADV measurement and the size of seeding particles are limited to five times of Kolmogorov scale in general (Toschi and Bodenschatz, 2009). The main advantages of ADV are the high response frequency and accurate spatial and temporary resolution while the main disadvantage of ADV is the sensors inherently present measurement noise to negatively affect the flow dynamics (Richard et al., 2013), such as containing signals of spikes with large amplitudes (Birjandi and Bibeau, 2009).

Particle imaging velocimetry (PIV) is a typical non-intrusive method for measuring turbulent flows by using laser and cameras to take images of seeding particles (usually 10-100 *um* in diameter, with similar properties as measured flow) to approximate the Lagrangian motion of the fluid flow at consecutive time levels. The flow velocity is calculated based on the sensing the displacement of particles over the time levels. Compared with hot wire velocimetry and ADV, PIV provides the velocity of the whole flow field and thus is no single point measurement. The seeding particles for PIV should be carefully chosen such that those particles closely flow the flow dynamics. However, PIV only provides two-dimensional velocity field in general (while three-dimensional velocity measurement can be achievable by using multiple cameras).

Extensive numerical and experimental measurements of the turbulent jet/plume were reported in open literature. Smith and Mungal (1998) concluded that the entrainment process might influence the jet penetration into the cross-flow. Murphy et al. (2016) conducted detailed experiments of oil released from a vertical jet in cross flow as well as

investigating the migration and entrapment of oil droplets in countercurrent vortices with the consideration of dispersant premixed with the oil. Kotsovinos (1975) observed that the axial velocity of buoyant jet stably follows a Gaussian distribution in the radial direction at more than six diameters from the jet orifice and persists before it deteriorates at larger than 80 diameters from the orifice. Falcone and Cataldo (2003) measured the mean radial and turbulent radial velocity profiles in a circular jet at up to 40 jet diameters downstream of the jet exit and established a relationship between mean radial velocity and jet entrainment. In general, most velocity measurements were taken within 80 diameters of the orifice (El-Amin et al., 2014; Suyambazhahan et al., 2009). Thus, there might be an interest in obtaining information at larger distances, especially from a horizontal jet in the presence of buoyancy.

The plume trajectory of the miscible buoyant jet is commonly modeled by a Lagrangian approach (Cheung and Lee, 1990), also known as JETLAG model, which predicts the trajectory and dilution of the buoyant jet in an ambient current. The Lagrangian approach disseminates the plume body into elements for numerical integration such that this model only provides the averaged flow characteristics of the buoyant jet body. Similar models were developed by Johansen (2000) and (Zheng et al., 2003). Yapa et al. (2008) further take consideration of the influence of non-ideal gas, gas dissolution and gas hydrate based on the Lagrangian framework. The Lagrangian based models are most popularly used to estimate the buoyant jet trajectories and dilution. Although Lagrangian model provides the averaged value of key parameters of the jet/plume, such as velocity and dilution rate, it does not solve the the detailed turbulent flow characteristics (e.g., turbulent intensity, Reynold stress, and dissipation rate). Furthermore, the Lagrangian approach

cannot capture the separation of droplets from the horizontal plumes to account for the movement of individual droplets under the influence of the turbulent flow (Zhao et al., 2016b).

Due to the rapid development of computational technology, Computational Fluid Dynamics (CFD) has emerged as the most widely used numerical method to solve turbulent flows. CFD approach can be classified into three main categories: Direct Numerical Simulation (DNS), Large Eddy Simulation (LES) and Reynold Averaged Navier-Stokes Equations(RANS).

Direct Numerical Simulation (DNS) differs from all the other approaches in that DNS is independent of any turbulence models in that the full range of spatial and temporary turbulence scales are resolved to provide the most accurate solution to the flow field. DNS is thus able to provide turbulence structure at the interface of two fluids along with information on detailed entrainment processes (Westerwheel et al., 2009). However, DNS is the most computationally expensive method within CFD approach and thus only limited to low to moderate Reynold number flow (e.g., limited to Reynold number of 5,000) (Boersma et al., 1998; Picano and Casciola, 2007). The computational cost of DNS grows at the scale of Re^3 such that DNS approach is currently limited to academic research to provide scientists of the understanding of fundamentals of turbulence instead of actual engineering applications as most engineering flows are highly turbulent flows (with Re exceeds 3000) (Pope, 2000).

Reynold Averaged Navier-Stokes Equation (RANS) model solves the Reynold averaged Navier-Stokes equations. RANS solves the time average flow instead of accounting for the turbulence at various scales(Kumar and Dewan, 2014; Rathore and Das,

2016; Yan and Holmstedt, 1999). RANS is the most popularly used CFD method in engineering and industrial applications for its robustness in capturing the overall dynamics for even very large Reynolds numbers. RANS inherently cannot handle complex turbulent flow with massively separated flows (Georgiadis, et al 2010), streamline curvatures, and swirling flows with rotations. Meanwhile, the RANS method does not calculate the detailed spatial and temporary turbulence structures as RANS only solves for the filtered average turbulent flow in nature.

Large Eddy Simulation (LES) emerged as a compromise between DNS and RANS. LES typically employs filter function (e.g., Gaussian filter function, square filter function, etc.) to determine the large turbulence scale solved fully in Navier Stokes equation and the small turbulence scale modeled by sub-grid modeling (SGS) (Sagaut, 2005). Thus, the LES approach eventually approximates to DNS if the filtered scale is increasingly small. The resolution of large scale turbulence while modeling the small scale turbulence provides access to the unsteady turbulence motion is an advantage of LES compared to RANS. The recent trend is that LES has been more widely used in engineering fields where RANS method is traditionally used thanks to the rapid development and progress of computation power, memory and storage (Georgiadis et al., 2010).

1.2.2 Oil Droplet Breakup

The initial stage of the jet is subjected to the strong influence of shear force and instability at the edge of the discharged jet, which results in the primary breakup of droplets for the multiphase flow (Xiao et al., 2014). The subsequent entrainment after primary breakup leads to a secondary breakup, which results in the formation of smaller oil droplets (Shinjo

and Umemura, 2010). In the process of droplet breakup, the mixing and entrainment can be further complicated at the interface during jet breakup as this process is dominated by small-scale turbulent structure(Carazzo et al., 2006).

The droplet breakup of oil jets is mainly determined by the balance of destructive forces due to turbulence to those resisting breakup due to interfacial tension. This is well represented by the Weber Number (We), which represents the ratio of inertial force to surface tension. The Weber number at the orifice is calculated as:

$$W_e = \frac{\rho_o U_o^{\,2} D_o}{\sigma_{ow}} \tag{1.4}$$

where ρ_o is the oil density, U_o is oil velocity, D_o is oil orifice diameter and σ_{ow} is oil-water interfacial tension. Three regimes of droplet breakup can be established based on We number: bag breakup, stripping breakup and catastrophic breakup, as shown in Figure 1.2.

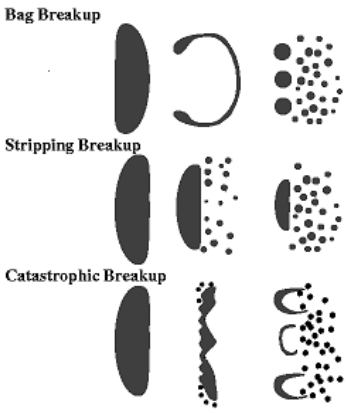

Figure 1.2 Schematic view of drop breakup regimes (Liu and Reitz, 1997): bag breakup: 6<We<80, stripping breakup: 80<We<350, catastrophic breakup: We >350.

In the subsurface oil jet discharge, the breakup process of oil droplet is dominating compared to coalescence. After a few diameters, the oil droplet breakup process becomes less obvious, indicating the diminishing trend of continuing droplet breakup (Liu and Reitz, 1997).

The Weber number can be further scaled by Reynold number to obtain the Ohnesorge number (Oh) to relate the viscous forces to inertial and surface tension forces:

$$Oh = \frac{\sqrt{We}}{\mathrm{Re}} \tag{1.5}$$

The subsurface oil discharge condition can be determined by Ohnesorge number vs. Reynolds number diagram. When the oil jet discharge condition is beyond the turbulent zone, the oil jet is fully atomized, indicating the formation of fine droplets after breakup. The oil droplets quickly breakup after initially released from the orifice and reached steady state(e.g., no more continuing breakup)after a few diameters downstream the orifice (Zhao et al., 2016b).

1.2.3 Dispersant Applied in Oil Spill Mitigation

Dispersant is mixtures of solvents, surfactants, and other additives that are applied to oil slicks to reduce the oil-water interfacial tension (NRC, 1989). The surfactant is the main effective component of dispersant to reduce the surface tension of oil droplets to allow the large oil droplets to be dispersed into smaller droplets in the open water field.

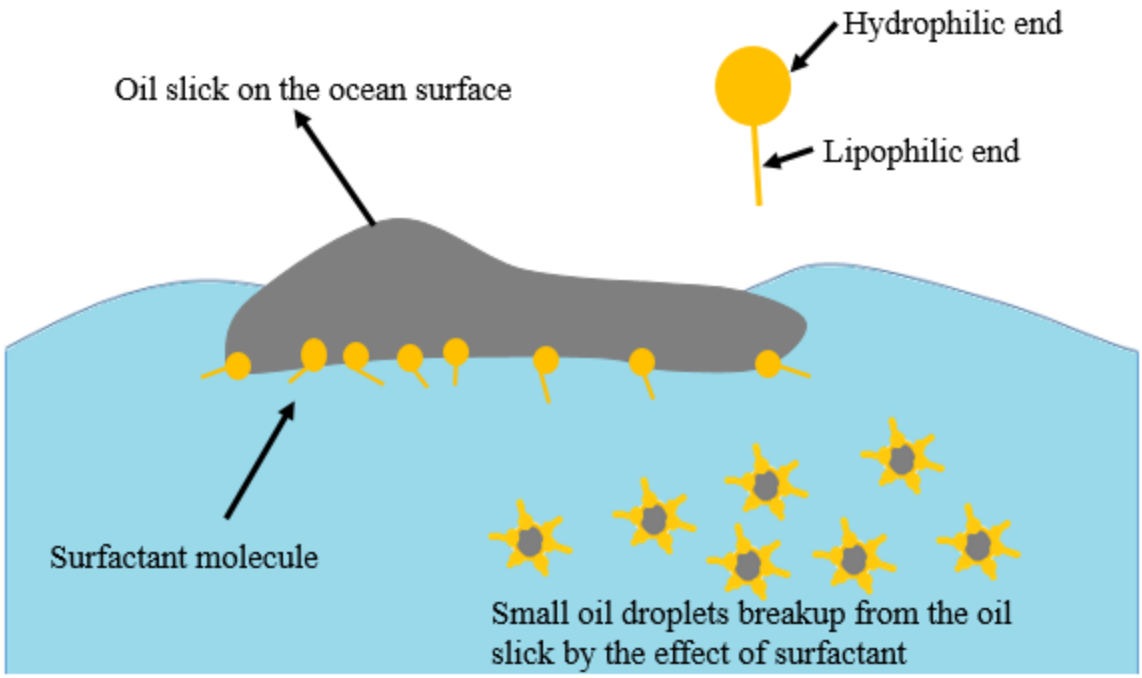

Figure 1.3 Mechanism of surfactant on the oil droplet breakup. The surfactant molecules, which are the effective component of the applied dispersant, decreases the oil-water interfacial tension such that the oil slick breakup into small droplets.

The surfactant contains molecules with a water-compatible ("hydrophilic") end and an oil-compatible ("lipophilic") end. The water-compatible end ("hydrophilic") is prone to be attached to the water molecules while the oil-compatible ("lipophilic") end is prone to be attached to the oil molecules. Due to the attachment of these ends, the interfacial tension of the oil droplet is reduced thus the oil slick is reduced to smaller one and the oil droplet size is further reduced by the ocean current, wind, and wave energy in the water.

The oil dispersant was systematically researched in various aspects, including its effectiveness and efficacy in oil spill mitigation (NRC, 2005) and comparative toxicity on the ocean environment (Fuller et al., 2004). Although dispersant was successfully used to clean up the oil spill, evidenced by numerous related studies (Chapman et al., 2007; Lessard

and DeMarco, 2000; Pezeshki et al., 2000), few studies were conducted in understanding the influence of dispersant on the hydrodynamics of underwater oil jet/plume, especially in the near-field region as the changed jet/plume hydrodynamics due to the application of oil dispersant may affect the estimation of initial droplet size distribution as well as water entrainment from the surrounding environment.

1.3 Research Objectives

Studying the hydrodynamics characteristics of multiphase oil jet is of critical importance in various aspects. Once the oil is released from the orifice, it breaks up into smaller droplets. The smaller droplets are more likely to remain in the water column while larger ones rise up to the surface, which subsequently affects carbon dissolution and biodegradation (NRC, 2005; Reddy et al., 2012). Although much is researched on surface waters (Boufadel et al., 2014; NRC, 2003), little is known about the characteristics of subsurface oil release.

Experimental measurements are not easy to be conducted as the velocity measurement devices (e.g., Acoustic Doppler Velocimetry and Profiler) cannot be placed too close to the orifice due to the strong turbulence vibrations near to the orifice and thus most experimental measurements were taken at the downstream of the jet (Rodi, 1982; Sykes et al., 1986; Yamashita et al., 1996).

In addition, many oil plumes are accompanied by the release of natural gas (MacDonald et al., 2002; Reddy et al., 2012), which would increase the mixing energy in the plume (Neto et al., 2008; Zhao et al., 2017a). Therefore, one needs to account for the

gas to oil ratio (GOR). Furthermore, as the released oil is "live" (i.e., containing natural gas dissolved in crude oil), it has been argued that the release of gas into the water could further atomize the oil. Thus, the primary focus of the proposed study is to investigate the hydrodynamics of subsurface oil jets by combining both experimental and numerical approaches.

The objectives of the research are as follows:

1. Investigate various aspects of hydrodynamic characteristics (e.g., jet profile, velocity, turbulence kinetic energy, and dissipation rate, etc.) of subsurface oil release (with/without dispersant) by using high resolution camera and Vectrino Profiler (based on the Doppler theory) to measure jet velocity experimentally and Computational Fluid Dynamics (CFD) approach numerically.

2. Model the transport of oil droplet after the primary breakup, including the effect of different physical forces exerted on the individual droplets, to evaluate the movement and trajectories of single droplets under the effect of turbulent flow.

3. Evaluate the effect of gas to oil ratio (GOR) on the hydrodynamics of subsurface oil release under Deepwater Horizon condition, and its impact on the estimation of oil discharge rate and energy loss by using Computational Fluid Dynamics (CFD) approach.

4. Understand the hydrodynamics of the turbulent multiphase jet by experimentally by using the combined approach of Particle Imaging Velocimetry (PIV) measurement CFD simulation to account for the influence of gas phase volume fraction.

CHAPTER 2

EXPERIMENTAL AND NUMERICAL CHARACTERIZATION OF THE HYDRODYNAMICS OF THE UNDERWATER OIL JET WITHOUT AND WITH DISPERSANT

2.1 Experimental Approach

A subsurface oil release experiment was conducted, which is consisted of releasing the crude oil from a horizontal orifice whose diameter is 2.4 mm. The saltwater flume tank is 32 m in length, 0.6 m in width and 2.0 m in height, which is shown in Figure 2.1. The flume was filled with seawater from Halifax bay to a depth of 1.5 m. The water salinity in the tank was measured using a hand held meter (YSI model #30-1-FT; Yellow Springs, USA) and was found to be 28 parts per thousand and a density of 1020.

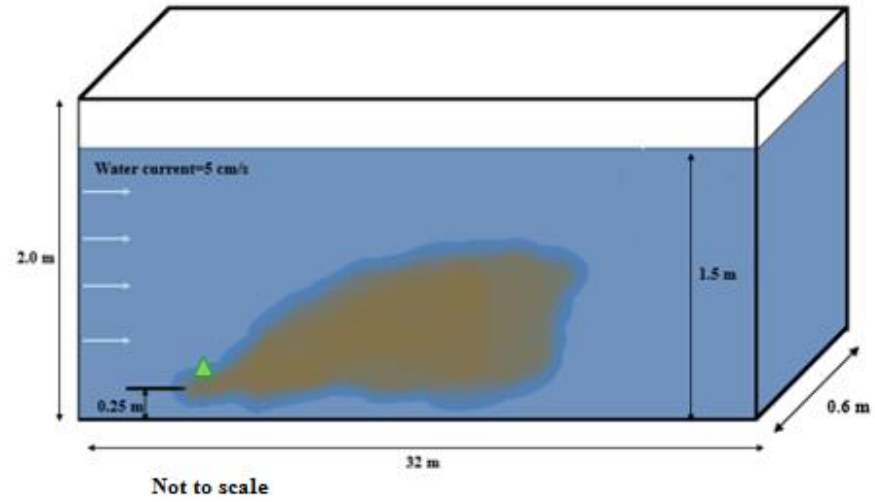

(a)

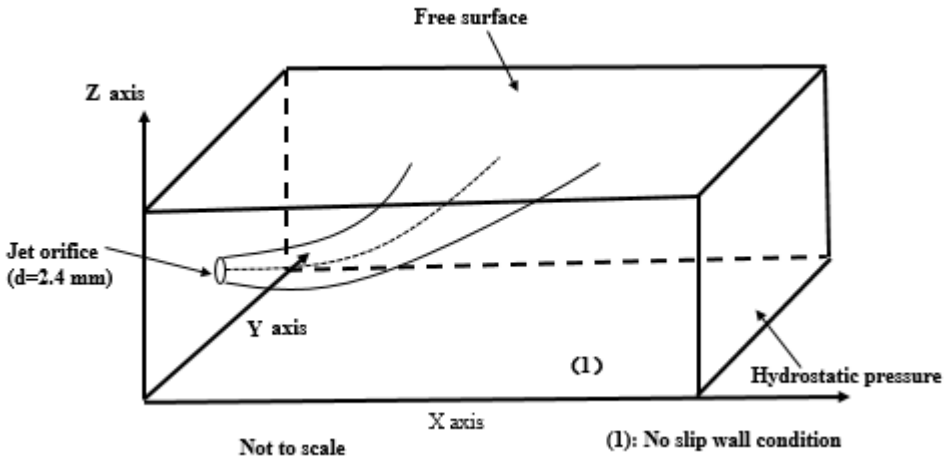

(b)

Figure 2.1 Schematic view for the release of the horizontal oil plume (a) the dimensions of Bedford Institute of Oceanography Tank (with the green triangle denoting the position of the Vectrino Profiler, whose location was as (x=0.5 m, y= 0.3 m, and z=0.304 m) (b) the boundary condition implemented in the CFD simulation.

A horizontal current was generated (through manifolds and pumps) in the tank to produce an average horizontal water velocity of 5.0 cm/s along the direction of the jet. The purpose of the current was to allow a better sampling of the oil droplet size distribution through the reduction of the concentration by dilution. However, the measurement of the

droplet size is not considered in this work. The orifice had a diameter of 2.4 mm, at an elevation of 0.25 m from the bottom of the tank. The oil was Alaska North Slope (ANS) with density $\rho_o = 866\,kg/m^3$, dynamic viscosity μ_o=11.5 cp, and the interfacial tension (IFT) with water σ_{ow}=20 mN/m (P. Than, 1988). The oil mass flow rate was 58 g/s. The oil temperature in the canister was 80 ℃. All of these values are reported in Table 2.1.

Table 2.1 Experimental Conditions for the Oil Release

Orifice diameter (mm)	2.4
Reynold number of the jet (Re)	2676
Weber number of jet, no dispersant	22793
Weber number of the jet, with dispersant	911720
Ohnesorge number of jet, no dispersant	0.05
Ohnesorge number of the jet, with dispersant	0.36
Oil mass flow rate (g/s)	58
Seawater density (kg/m^3)	1020
Seawater salinity (ppt)	28
Seawater temperature (℃)	15
Oil density(kg/m^3)	866
Oil viscosity (cp)	11.5
Horizontal current velocity (m/s)	0.05
Oil-water interfacial tension without dispersant (mN/m)	20
Oil-water interfacial tension with dispersant (mN/m)	0.5
Dispersant to oil ratio (DOR)	1:20

For the same oil release rate (58 g/s), two situations were considered: 1) Oil without dispersant (OwoD) and 2) Oil premixed with dispersant (OwiD) where the dispersant was COREXIT 9500 (Nalco Inc), and the volumetric ratio of dispersant to oil (DOR) was 1:20. Each oil release lasted about 24.00 s, resulting in approximately 1.4 kg of oil in the flume after each release. The plume achieved steady state in approximately 8.00 s after the initiation of the release.

The interface tension (IFT) was estimated based on prior works; Gopalan and Katz (2010) used DOR between 1:15 to 1:20 for COREXIT with ANS, and found IFT=0.19-0.83 mN/m. We found a value of 0.5 mN/m for the DOR of 1:20 (Pan et al., 2017), and thus we used the IFT value of 0.5 mN/m when dispersant was used at the DOR of 1:20.

The Weber number is the ratio of inertial force to surface tension. The orifice Weber number $W_e = \rho_o U_o^2 D / \sigma_{ow}$ was equal to 22,793 for the oil without dispersant (OwoD) and to the value 911,720 for oil with dispersant (OwiD). The Ohnesorge number given by $Oh = W_e^{1/2} \mathrm{R_e}^{-1}$ (see Table 2.1) was 0.05 for OwoD and 0.36 for OwiD. Using the Ohnesorge-Reynolds diagram (see Figure A1) (Johansen et al., 2013; Murphy et al., 2015; Zhao et al., 2016a), one concludes that the condition of release was "atomization". Therefore, the oil jet would break into small oil droplets upon release into the water.

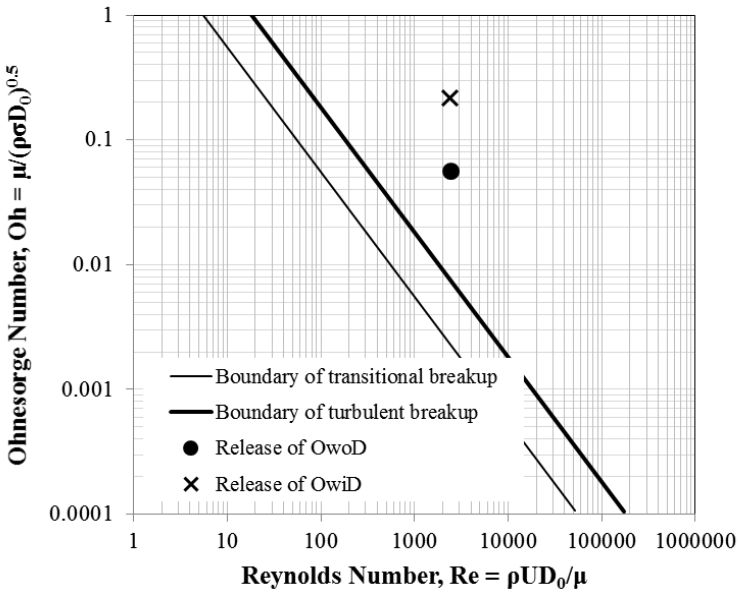

Figure 2.2 Reynold number vs. Ohnesorge number (showing that the jets in the experiments are atomizing).

The overall shape of the plumes was photographed and filmed using a GoPro® Hero 4 camera with an underwater housing and a resolution of 1080p (120 FPS). The water velocity was measured using a Nortek Vectrino Profiler, which was placed 50.0 cm from the jet orifice in the horizontal direction and 5.4 cm above the jet orifice, and it was lined up in a vertical cross-section through the plume centerline plane in the width direction, shown in Figure 2.7a. Based on the technical specification of the Nortek Vectrino profiler, it has an accuracy of 1 mm/s. The sampling rate for Vectrino Profiler was 100 Hz. The Vectrino Profiler measures velocity based on the principle of the Doppler effect. The Vectrino Profiler measures from 4.0 cm to 7.5 cm below the central transmitter with a total of 35 samplings, shown in Figure 2.3.

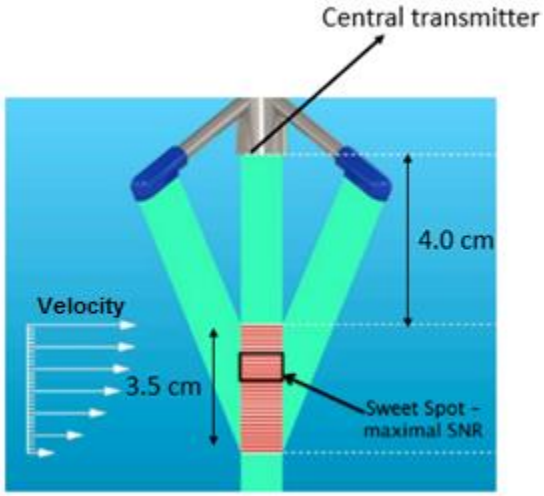

Figure 2.3 Schematic describing of the Vectrino Profiler used in the experiment. The Vectrino Profiler measures from 4 cm to 7.5 cm below the central transmitter. There are 35 sampling cells in total and each sampling cell is 1 mm. The black square box indicates the "sweet spot" within which the measured data are with the maximum signal to noise ratio (SNR).

The minimum requirement for quality measurement of the velocity is a signal-to-noise ratio SNR (provided by the instrument) of 15 decibels (dB). The minimum requirement for the correlation function (also provided by the instrument) should be no less

than 60%. As shown in Figure 2.4, the measured correlation and averaged SNR is above the minimum requirements for both the OwoD and OwiD cases.

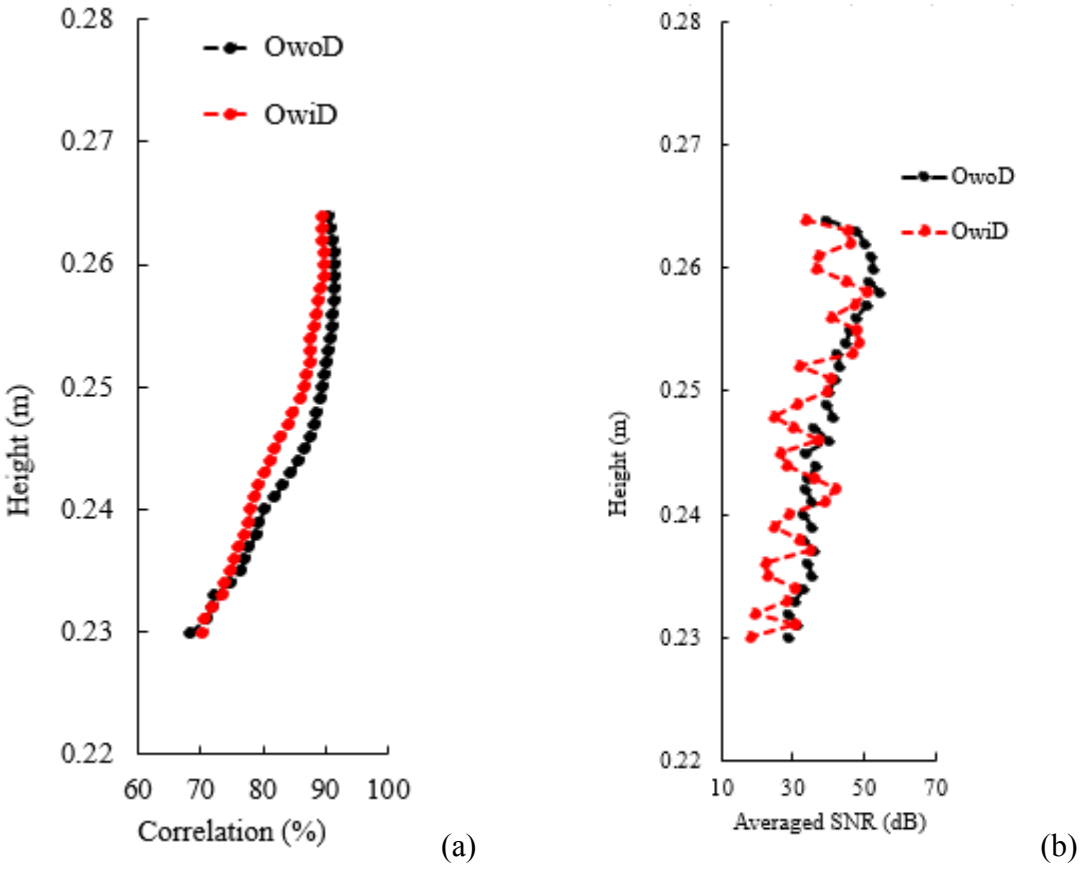

Figure 2.4 Measurement by Vectrino Profiler (a) averaged SNR (b) averaged correlation.

Experimental techniques for evaluating the turbulence dissipation based on velocity measurement were discussed by Kaku et al. (2006). In the present paper, we use the autocorrelation function approach, which calculates the turbulence dissipation rate (watts/kg) as follows (Kresta, 1993; Wu et al., 1989):

$$\varepsilon_j = A\frac{\left(u'_{rms,j}\right)}{\tau_{l,j}} \quad j=x,y,z \tag{2.1}$$

where ε_j is the turbulence dissipation rate based on the velocity component in the "j"

direction. A is a constant, which is taken as unity in the present paper. The term $u'_{rms,j}$ is the root mean square of the turbulent component of velocity. $\tau_{l,j}$ is the integral time scale calculated as:

$$\tau_{l,j} = \int_0^{+\infty} R_{l,j}\, dt \tag{2.2}$$

The upper limit of $+\infty$ is impractical and thus we used the point of first zero crossing (Kaku et al., 2006). $R_{l,j}$ is the autocorrelation function given by:

$$R_{l,j} = \frac{\overline{u'_j(t)u'_j(t+\tau)}}{\overline{(u'_j)^2}}, j=\text{x,y,z} \tag{2.3}$$

where $u'_j(t)$ is the turbulent velocity component and τ is the lag time (arbitrary). Turbulence is expected to be anisotropic near the orifice, with turbulence velocity fluctuations in the axial direction reported to be double that in the transverse direction, it becomes more or less isotropic at larger than 40 diameters due to the transfer of shear stress to the transverse components (Friehe et al., 1971). As the Vectrino Profiler is placed at 50 cm from the jet orifice, which is more than 200 diameters from the orifice (whose diameter is 2.4 mm), turbulence was assumed isotropic there. Thus the value of ε at a the Vectrino Profiler was estimated as the average of the directional values ε_j values given by Equation 2.1.

The turbulence kinetic energy per unit mass based on the experiment, $k_{\exp,}$ was calculated based on the definition (Pope, 2000):

$$k_{\exp} = \frac{1}{2}\left(\sum_{j=1}^{3} \mathrm{u}'_{rms,j}{}^{2} \right) \tag{2.4}$$

2.2 Numerical Approach

For numerical modeling, both oil and water were considered as incompressible fluids. The turbulent jet involves significant unsteadiness in nature; however, the averaged motion was obtained from the Reynold Averaged Navier-Stokes (RANS) Equations. The turbulence model $k-\varepsilon$ model (Belcaid et al., 2015; Hargreaves et al., 2012) was used. It requires the solution of two equations for two scalar turbulence quantities: the turbulence kinetic energy, k , and the turbulence dissipation rate, ε . The k equation reads as follows (ANSYS, 2009):

$$\frac{\partial}{\partial t}(\rho k) + \frac{\partial}{\partial x_i}(\rho k \mathrm{u}_\mathrm{i}) = \frac{\partial}{\partial x_j}\left[\left(\mu + \frac{\mu_t}{\sigma_k} \right) \frac{\partial k}{\partial x_j} \right] + \rho \overline{\mathrm{u}'_\mathrm{i} \mathrm{u}'_\mathrm{j}} \frac{\partial \mathrm{u}_\mathrm{j}}{\partial x_i} + G_b - \rho\varepsilon \tag{2.5}$$

where ρ denotes water density, the term G_b is the production of turbulence kinetic energy due to buoyancy from non-isothermal effects. It can be calculated as:

$$G_b = \beta g_i \frac{\mu_t}{\mathrm{Pr}} \frac{\partial T}{\partial x_i} \tag{2.6}$$

where T is temperature and β is the thermal expansion coefficient:

$$\beta = \frac{-1}{\rho}(\frac{\partial \rho}{\partial T}) \tag{2.7}$$

Pr is the Prandtl number, which is defined as:

$$\Pr = \frac{C_p \mu}{k_{th}} \tag{2.8}$$

where C_p denotes the specific heat, k_{th} is thermal conductivity and μ is the dynamic viscosity of the fluid. The term μ_t in Equation 2.6 is the eddy diffusivity defined as:

$$\mu_t = \rho C_\mu \frac{k^2}{\varepsilon} \tag{2.9}$$

For isothermal flows, the coefficient G_b is zero through the temperature gradient term (see Equation 2.6). However, even if the gradient term was non-zero, G_b would be close to zero if the fluid density does not change much with temperature, see Equation 2.7. The equation for ε is as follows:

$$\frac{\partial}{\partial t}(\rho\varepsilon) + \frac{\partial}{\partial x_i}(\rho\varepsilon u_i) = \frac{\partial}{\partial x_j}\left[\left(\mu + \frac{\mu_t}{\sigma_\varepsilon}\right)\frac{\partial \varepsilon}{\partial x_j}\right] + C_{1\varepsilon}\frac{\varepsilon}{k}(G_k + C_{3\varepsilon}G_b) - C_{2\varepsilon}\rho\frac{\varepsilon^2}{k} \tag{2.10}$$

G_K represents the production of turbulence kinetic energy due to the mean velocity gradients, and it is evaluated using the Boussinesq hypothesis:

$$G_k = \mu_t S^2 \tag{2.11}$$

where μ_t is the eddy diffusivity and S is the modulus of the mean rate-of-strain tensor, defined as:

$$S = \sqrt{2S_{ij}S_{ij}} \tag{2.12}$$

$$S_{ij} = \frac{1}{2}\left(\frac{\partial u_i}{\partial x_j} + \frac{\partial u_j}{\partial x_i}\right) \tag{2.13}$$

where $C_{3\varepsilon}$ is a variable parameter that accounts for the fact that ε is affected by buoyancy (due to the difference in density) and is given as follows:

$$C_{3\varepsilon} = \tanh\left(\frac{u_3}{u_1}\right) \tag{2.14}$$

where u_3 is the vertical velocity (also taken at u_z) and u_1 is the horizontal velocity (also denoted as u_x). Thus, $C_{3\varepsilon}$ is a variable varying locally depending on the ratio of the velocity components. The constants in Equations (2.9) and (2.10) are taken as C_μ=0.09, $C_{1\varepsilon}$=1.42, and $C_{2\varepsilon}$=1.92 (ANSYS, 2009).

Equations (2.5)-(2.14) were solved in the commercial software ANSYS-FLUENT®. The Volume Of Fluid (VOF) method (Hirt and Nichols, 1981) was used to track the oil-water interface.

The top water surface was modeled as a constant pressure condition because it is in contact with the atmosphere. The bottom surface and the vertical long surfaces of the tank were modeled as Neuman no-flow condition and a no-slip wall. The boundary condition on the upstream narrow vertical surface of the tank was taken as the inflow of 5.0 cm/s (to match the experiment) and that on the downstream was taken as hydrostatic, as shown in Figure 2.1b.

The turbulence dissipation rate at the orifice was obtained by running FLUENT separately for a long pipe (more than 60 diameters) with the same mass flow rate as in the present experiment. The following values reached the steady state in the pipe after 20 diameters: The turbulence kinetic energy and dissipation rate at the orifice of the tank was of 8.86 m^2/s^2 and 33,786 watt/kg, respectively.

The detailed numerical techniques used in the present study are summarized in Table 2.2. Implicit steady solver, which eliminates the transient term and becomes dependent only on space was used in Fluent, and second order upwinding (i.e., spatial derivatives are solved by upstream differentiation) scheme was used for the steady state equations of the VOF. The computational domain had a total number of 2,777,029 cells. The mesh was refined at the orifice and relatively coarse at the downstream. In addition, we performed a grid independence study. We used 11,101,116 nodes (e.g., four times the nodes number used in the present study) and monitored the velocity at few points in the domain, and found it to be close to that of the coarser mesh used in the current study

(2,777,029 nodes). Thus, it is concluded that the current mesh is sufficiently fine for the intended purposes. A steady state approach was adopted, and the residual criterion for convergence was set at 10^{-6}.

Table 2.2 Numerical Techniques Used in the Present CFD Simulation

Segregated solver type	Pressure based
Pressure and velocity coupling	SIMPLE algorithm
Pressure interpolation scheme	PRESTO
Gradient discretization	Green-Gauss node based
Number of nodes	2,777,029
Mesh size	0.15 mm up to 4.0 cm
Convergence criteria for residual	10^{-6}

The IFT between this oil (ANS) and water was taken at 20 mN/m (see Table 2.1). However, as the VOF model does not track the exact location of the oil-water interface, accounting for the impact of dispersant required the usage of a volume force. Using the continuum surface force (CSC) approach by Brackbill et al. (1992) in which the interfacial force is transformed to a volume force at the interface (Marianne M. Francois, 2007), one obtains:

$$\vec{F} = \left(\sigma\kappa\hat{n} + \nabla_s\sigma\right)\delta \tag{2.15}$$

where σ is IFT (in the unit of N/m), κ is the average curvature of the interface, ∇_s is the surface gradient and δ is the dirac-delta function. The first term on the right hand of

Equation 2.15 denotes the interfacial force in the normal direction and the second term denotes interfacial force in the tangential direction.

The CSC was implemented by the diffused interface modeling, as we are interested in the hydrodynamics of plumes at steady state and thus a continuous and steady jet profile was needed. The sharp interface module within FLUENT is not likely to achieve a continuous jet profile(ANSYS, 2009). In addition, as this work focused on the overall behavior of the plume, the detailed interfacial phenomena were not investigated.

As the oil was at 80°C prior to release, there was a need to evaluate the impact of temperature on the jet/plume hydrodynamics. The dynamic viscosity of water μ_w as a function of fluid temperature, *T*, can be calculated as (John C. Crittenden, 2012):

$$\mu_W = 1.002 \times 10^{-3} (10^B) \tag{2.16}$$

where $15\ ℃ \le T \le 80\ ℃$

The dynamic viscosity of crude oil μ_o as a function of temperature can be calculated as follows (Manzar Sattarin, 2007):

$$\mu_o = a \times \frac{e^{(b/API)}}{API} \tag{2.17}$$

where the units of μ_o is cp, $a = 0.00735T^2 - 4.3175T + 641.3572$, $b = -1.51T + 568.84$. *API* is the specific gravity of the crude oil based on the American Petroleum Institute

standard, and it was equal to 31.9 for this oil. The IFT in the absence of dispersant as a function of temperature can be estimated as follows (Zhao et al., 2015):

$$\sigma_{ow} = \left[\frac{1.58(\rho_w - \rho_o) + 1.76}{T_r^{0.3125}} \right]^4 \tag{2.18}$$

where T_r is the reduced temperature given by:

$$T_r = \frac{T + 459.67}{T_{cm}} \tag{2.19}$$

where T_{cm} is the pseudo-critical temperature given by:

$$T_{cm} = 24.2787 K_w^{1.76544} \gamma_o^{2.12504} \tag{2.20}$$

where K_w is Waston characterization factor, taken as 0.66 and γ_o is the oil specific weight (equal to 0.866 here).

2.3 Results and Discussion

The simulation with the injected oil of a uniform temperature of 80 ^{o}C was conducted to investigate the effect of temperature on the plume profile. Theoretically, the oil jet with high temperature should rise faster compared to isothermal one, as the temperature difference would introduce additional buoyancy, known as the Boussinesq effect. However,

we found that there no noticeable difference in the jet/plume between the isothermal 15ºC and the one where the oil has an initial temperature of 80ºC. This is probably because the heat from the high temperature release dissipated rapidly in the surrounding water, due to the turbulence diffusion and entrainment of surrounding water. Thus, in terms of the overall dynamics, the oil temperature of 80ºC had no noticeable effect, and for this reason, the remainder of this manuscript reports only the isothermal situation (i.e., as if the oil was released at 15ºC, the temperature of the surrounding seawater).

Figure 2.5a and 2.5c show the instantaneous jet profile of OwoD and OwiD, respectively. One notes that the color of the OwoD is black while that of OwiD is brown (resembling coffee), which is commonly observed when using dispersant (Brandvik et al., 2013; Johansen et al., 2013). The OwoD plume edges appear smoother than those of the OwiD. Thus, it seems that larger IFT of the oil-water (for OwoD) tends to keep the oil together minimizing the disturbance of the oil-water interface that would emanate from turbulence.

Figure 2.5b and 2.5d report the average of 480 frames, between t=11.00 s and t=15.00 s of the release. The spread angle was approximately 21° for OwoD, while it was around 24 ° for the OwiD, which seems to be close to the angle of miscible jets, at 23°-24° (Birkhoff, 1957; Horn and Thring, 1956; J.H.W. Lee, 2012). Noting that the only apparent difference is the IFT, it seems that the reduction of the IFT causes the two fluids to intermix better. Thus, when OwoD is released into the water, the IFT tends to keep the water off the oil, which results in less entrainment of the surrounding water, resulting in the smaller angle for the OwoD. When the IFT is significantly reduced due to the presence of the dispersant, the jet atomizes into a large number of small droplets that would allow the water

to be entrained within them or at least do not form a barrier for water entrainment. We also noticed that the angle of the jet was essentially the same as that of the OwiD when we made the IFT equal to zero.

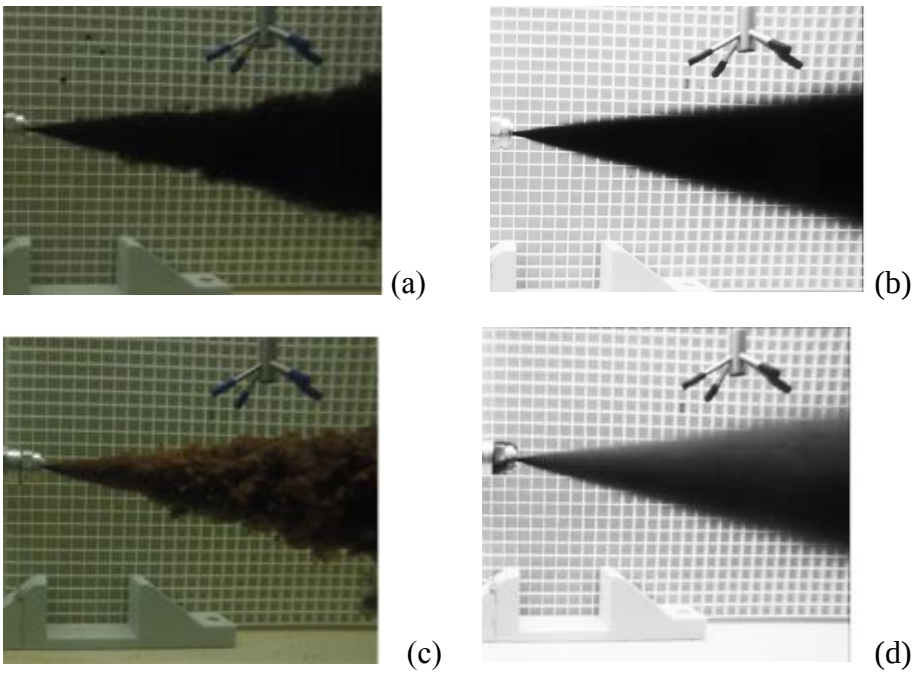

Figure 2.5 The jet release experiments (DOR=1:20) (a) instantaneous jet profile (OwoD) (b) averaged jet profile (OwoD) (c) instantaneous jet profile (OwiD) (d) averaged jet profile (OwiD). Each block in the grid in the background had a side of 1.6 cm.

Figure 2.6 shows the 3D instantaneous velocity at the jet centerline. The plume was full developed within ~10-16 s (the total duration was ~24 s), based on visual observations during the experiments. Therefore, the average velocity was computed over the time period of 10-16 s. Since the velocity profiles were similar within the ~10-16 s, to better illustrate the velocity data, only values within 11-12 s are presented in Figure 2.6. The velocity U is horizontal in the direction of the discharge, V is horizontal in the direction normal to U, and W is the vertical velocity. For the case without dispersants, the velocity is basically pointing in the discharge direction at the centerline, with a high velocity U of about 0.4 m/s.

Fluctuations can be seen in velocity V and W, but with relatively small values. The average velocities of V and W are close to zero. The average velocity magnitude was 0.43 m/s 60.1 m/s at the location of the measurement. The velocity profiles for the case with dispersants are very similar to the one without dispersants, with a slightly lower velocity at 11.3-11.6 s. The average magnitude of the velocity for the dispersant case was 0.37 m/s 60.15 m/s. The velocity discrepancy for the cases without and with dispersant may rely on that the droplet size decreased dramatically with the addition of dispersants, and thus the water was able to move between droplets more freely, thus slowing down the jet.

The average values for SNR and correlation coefficient without and with dispersant cases are also reported in Figure 2.6. The SNR value is very stable, basically within the range of 37.5-42 dB, indicating that sufficient particle seeding was available during the measurements. Also, 95% of the correlation coefficients were larger than 70%, indicating that measurement uncertainty was low.

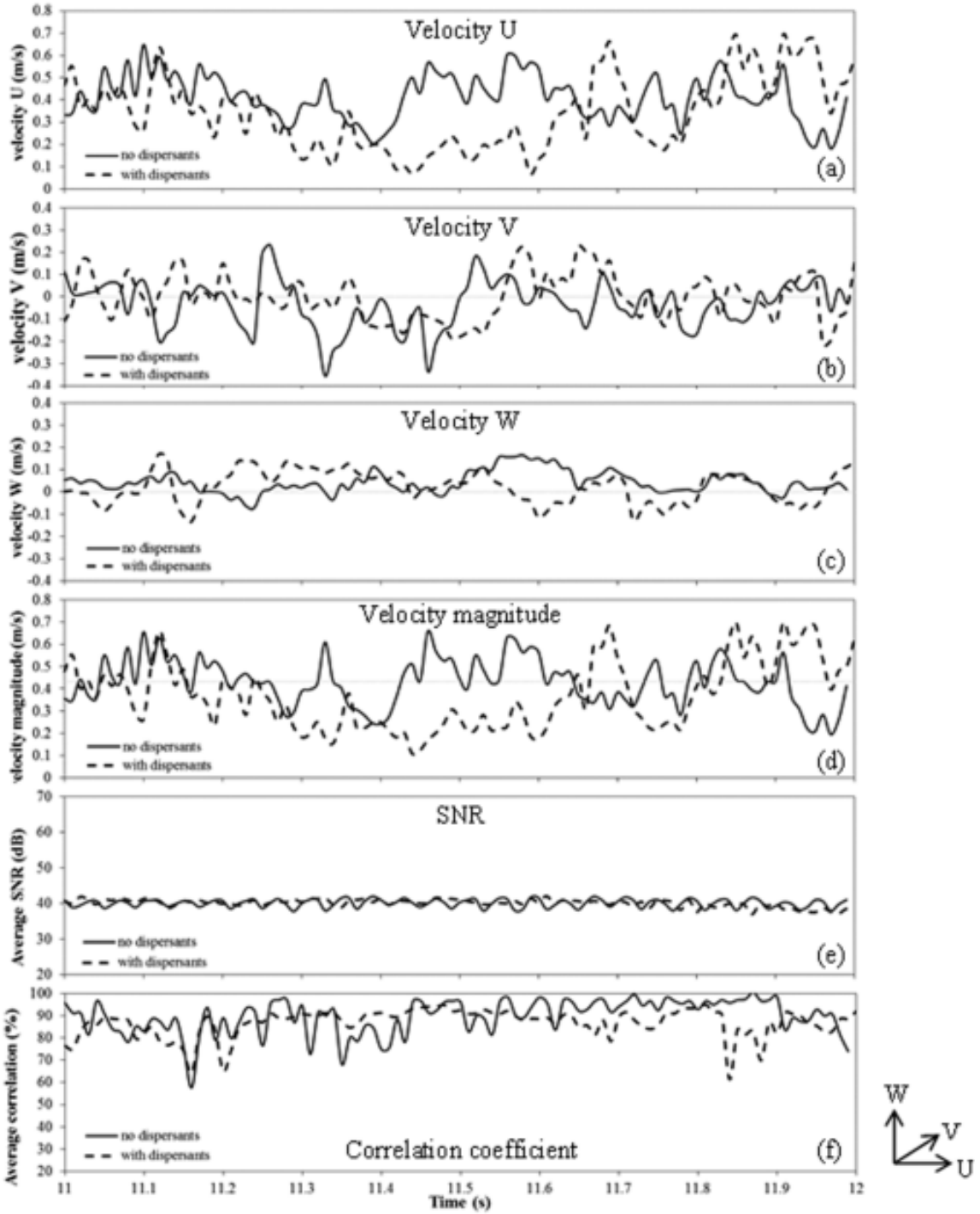

Figure 2.6 Instantaneous velocity profile obtained from the Vectrino profiler at the jet centerline for the cases without and with dispersants: (a, b, and c) three velocity components; (d) the magnitude of the velocity; (e) signal-to-noise ratio (SNR); (f) correlation coefficient. The average SNR of 40 and correlation coefficients of over 85% indicate the reliability of the results.

Figure 2.7a shows the simulated results of the edge of the plume, delineated using 10% of the holdup (volume of oil per total volume of fluids). We obtained the jet profile in the vicinity of the jet exit during the experiment, where we found that the jet angles were 21° and 23 °for the jet without and with the dispersant in the experiment measurement, respectively. Though the plume boundary can be visually estimated from the images taken from the experiment, for numerical simulations, the boundary has to be arbitrarily defined, which could be specified based on the fraction of a centerline value (Lee and Chu, 2003; Zhao et al., 2016a). We tried with different fraction of the centerline holdup (e.g., 2%, 5%, 10%,…) and found that the 10% holdup (of the centerline) agrees well with the experimental observation, and thus 10% holdup (of the centerline) was selected as the plume boundary in the current study.

Comparison between the edges of the OwoD and OwiD indicates that the OwiD does not rise as fast as OwoD, which suggests that OwoD had a larger buoyancy. This is consistent with the fact of less water entrainment in the oil jet in the OwoD (based on the narrow angle in Figure 2.5). As water is heavier than oil, larger water entrainment decreases the buoyancy of the jet.

Figure 2.7b shows the contours of holdup and velocity magnitude of OwoD jet. At this large scale, the contours of OwoD and OwiD jets looked similar, and for this reason, only the OwiD case was shown. The contour contains totally 83,853 nodes and the mesh size at x=0 m, 0.5 m, 1.0 m, and 2.0 m is 0.15 mm, 5 mm, 7.4 mm, and 19 mm, respectively. The holdup at the exit was 1.0 (as expected) and decreased rapidly to a few percents and even lower within 0.5 m of the orifice. The contours of the velocity magnitude show values larger than 0.2 to 0.3 m/s within the plume and a sharp decrease at the edge of the plume.

The orientation of the velocity vectors outside of the plume reflects the entrainment of fluids (i.e., water) to the plume, especially near the orifice.

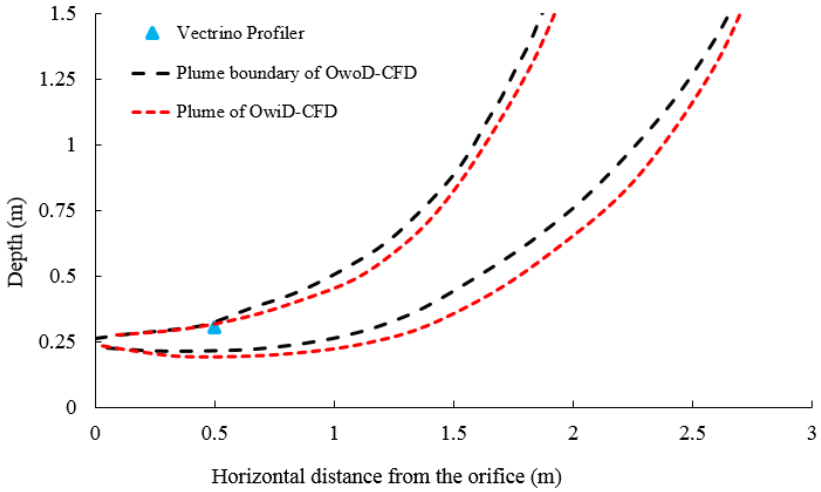

(a)

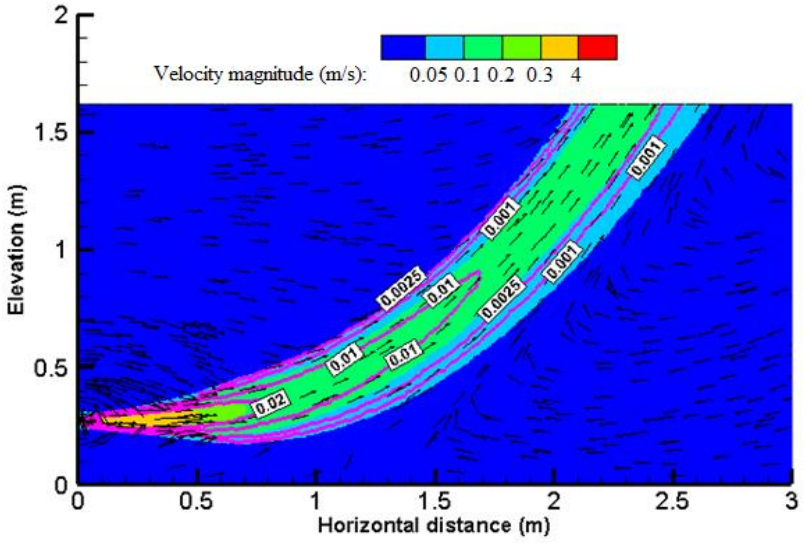

(b)

Figure 2.7 (a) Comparison of jet/plume shapes between the CFD simulation of the OwoD jet (IFT= 20 mN/m) and OwiD jet (IFT=0.5 mN/m). The edge of the plume is defined as 10 % of the holdup (volume of oil per total volume of fluids) (b) The profile of the OwoD plume through a vertical plane passing through the center axis. The figure shows the contour of the velocity magnitude (flooded colors) and the holdup, using purple lines. The arrows indicate the velocity component in the plane of the figure. The length of the velocity vector is taken as a uniform for better visualization.

Figure 2.8a report the velocity profiles at the Vectrino Profiler position (Figures 2.1 and 2.4a). Measurements were taken from time 11.00 s to time 12.00 s and then averaged to obtain a stable "steady state" velocity profile. The horizontal green dash line indicates the elevation of the jet orifice is at z=0.25 m. The local cell length for CFD simulation was approximately 5 mm. The Vectrino Profiler samples the velocity at 1.0 mm increments from z=0.23 to 0.265 m. The peak of the x velocity for the CFD simulation is above the orifice as the jet rises due to buoyancy. The maximum x velocity of the CFD simulation was at z=0.26 m for the OwiD jet and at z=0.275 m for the OwoD. This is probably because the OwoD jet has larger buoyancy compared to OwiD, and thus the maximum horizontal speed is shifted upward. Figure 2.8a shows that for both experimental and numerical results, the x velocity of OwoD plume was in general larger than that of the OwiD plume at the same elevation. This is most likely because OwoD entrained less water, and thus did not lose much of its horizontal momentum in comparison to the OwiD. The overall agreement between the simulated and observed results is good as the simulated results captured the observed trend of increase and subsequent decrease of velocity with elevation.

Figure 2.8b shows the vertical variation of the horizontal cross velocity at a vertical plane passing through the center axis. Negative values indicate velocity going inward in the plane of Figure 2.7 (i.e., velocity going to the left of the jet looking downstream). The simulated results suggest essentially a zero cross flow, which is expected based on the boundary conditions and would provide symmetric flow with respect to a vertical plane that passes through the centerline. The experimental results show fluctuations in the velocity, but the velocity was small, with magnitudes less than 0.04 m/s in general. The exception was for OwiD, which showed a sharp increase above 0.255 m in the positive

cross flow (inward in Figure 2.7). These variations could be due to the existence of vortices and/or localized entrainment of water into the plume due to turbulence (Zhao et al., 2016a) while the RANS model provides the average flow and thus is incapable of predicting this scale of vortices. The observed velocity fluctuations could be also due to imperfection in the geometry of the tank, which would then generate secondary flows. With the exception of the OwoD at elevations larger than 0.26 m, the variations are less than 0.03 m/s, and thus the discrepancy can be considered small.

Figure 2.8c shows the vertical variation of the vertical velocity. Positive values mean upward flow. One notes an increase in the CFD vertical velocity as one moves upward within the plume and then a decrease as it goes further upward, which results in a peak of vertical velocity at z=0.26 m (1 cm above the orifice) for the OwiD jet and z=0.27 m (2 cm above the orifice) for the OwoD jet. One notes the agreement between the results of CFD and experimental measurement is quite good except at larger than 0.26 m, which is probably due to the presence of eddies and/or imperfection in the tank geometry. In the experiment, the z velocity increases with height under the effect of buoyancy for both cases of OwoD and OwiD. However, the experimental vertical velocity of the OwiD jet does not increase as fast as the one of the OwoD and this was not observed in the CFD simulation as it cannot take account of the movement of individual droplets.

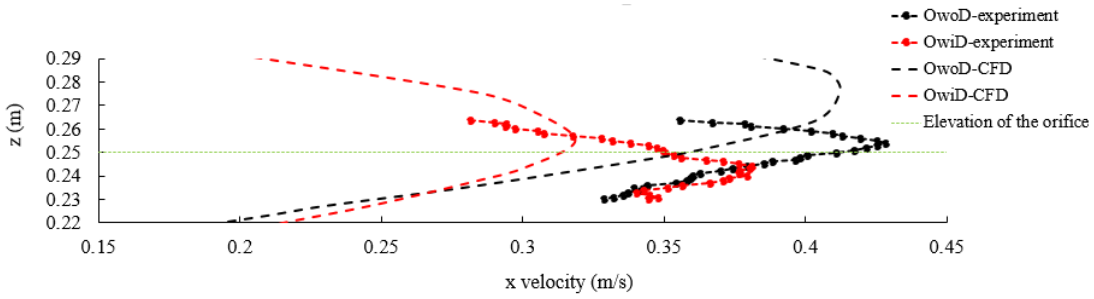

(a)

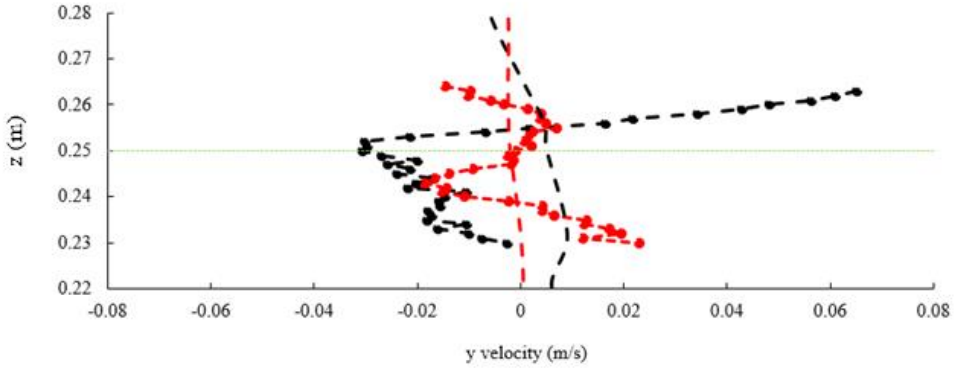

(b)

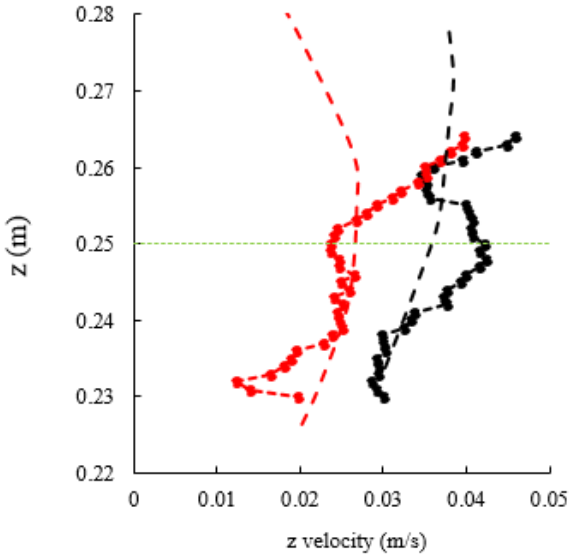

(c)

Figure 2.8 Velocity measurements by the Vectrino Profiler and CFD simulations at that location: (a) Horizontal velocity (i.e., in the x direction), where positive velocity is in the increasing x direction; (b) Horizontal y velocity, where positive values represent water moving into the plane of Figure 1 (i.e., right to left when looking downstream of the jet); and (c) Vertical z velocity, where positive velocity implies upward flow. All the profiles were within the 10% holdups of the plumes at the given location. The horizontal green dash line indicates that the jet orifice is located at z=0.25 m.

Figure 2.9a shows the experimentally determined turbulence kinetic energy based on Equation (2.4) along with that obtained from CFD. Throughout this work, we assumed that turbulence was isotropic, and for this, we used the k-ε model. The assumption is likely violated near the orifice where the shear flow is dominant. However, advanced turbulence models (e.g., Reynolds Stress model) were not used herein as the flow is likely to become isotropic within a short distance from the orifice. Evaluating the impact of the isotropic assumption is left for future work, where more detailed measurements could be obtained.

The difference between the various cases is generally small, considering the uncertainty in the experimental determination of turbulence velocities and the usage of a turbulence closure model that incorporates all scales. However, in both experimental and numerical results, the turbulence kinetic energy for OwiD was always slightly larger than that of OwoD (no dispersant). This is probably because the addition of dispersant (OwiD) decreased the IFT, and thus less turbulence kinetic energy was used to combat the interfacial tension force (see Equation 2.15), resulting in a larger turbulence kinetic energy for the OwiD. This is also confirmed in Figure 2.9b for the energy dissipation rate with higher values of the turbulence dissipation rate ε for the case with the dispersant (OwiD), indicating that the higher kinetic energy in Figure 2.9a was converted to thermal energy (i.e., ε).

Figure 2.9c shows the contour of the turbulence dissipation rate, ε, in a vertical plane centered on the jet. One notes that ε dropped sharply with the centerline distance (note the logarithmic scale of the contours). The relatively larger turbulence dissipation rate was concentrated near the orifice.

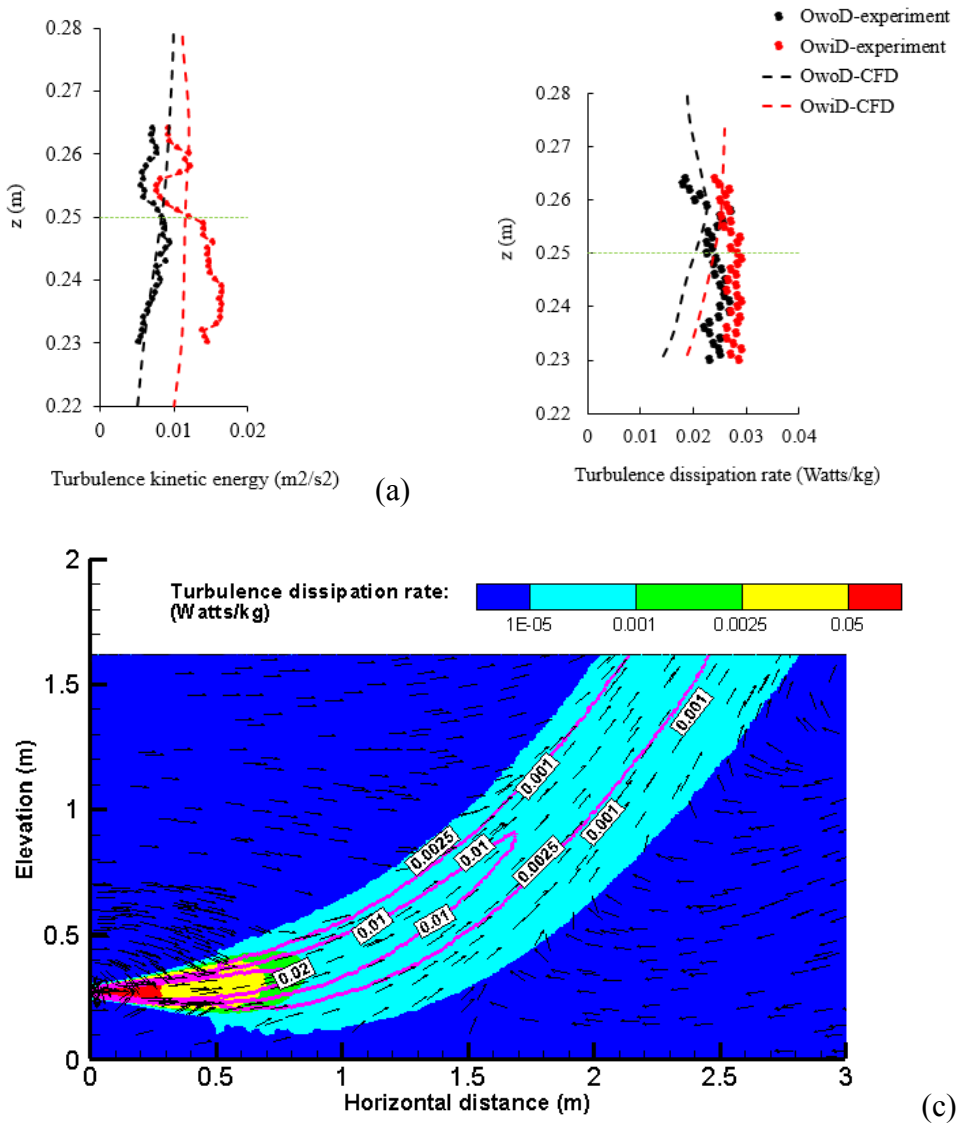

Figure 2.9 (a) Turbulence kinetic energy and dissipation rate obtained experimentally (using the Vectrino Profiler and Equation 2.1) and from the CFD simulations for both oil only and oil with dispersant jets (b) Turbulence kinetic energy obtained experimentally (using the Profiler and Equation 2.5) and from the CFD simulation for both oil only and oil with dispersant jets. The horizontal green dash line indicates that the jet orifice is located at z=0. 25 m. (c) The contour of the turbulence dissipation rate in the OwoD plume. Purple lines indicate the contour of the holdup, continuous flood contour indicates turbulence dissipation rate. The arrows indicate velocity vectors components that are parallel to the page surface. The length of the velocity vector does not represent the magnitude but only represent the direction.

Figure 2.10a reports the holdup from both cases of OwoD and OwiD. One notes that although both holdups start from the same value (of 1.0), the holdup of OwiD dropped

below the one of OwoD at 30 mm (i.e., around 12 diameters) from the orifice, reflecting a larger volume of water in the OwiD. The two holdup curves appear to level off at around 150 mm to 200 mm from the orifice.

Figure 2.10b shows the variation of the dimensionless velocity $\frac{U_c}{U_o}$, where U_c is the centerline velocity and U_o is the initial velocity at the orifice, of OwoD and OwiD jets along the horizontal distance from the orifice based on the CFD simulations. The results of $\frac{U_c}{U_o}$ for OwoD and OwiD jets are generally close with one another. The most significant difference occurs at 30-50 mm from the orifice in the horizontal direction although the absolute difference is quite small and the two curves of $\frac{U_c}{U_o}$ are level off from the distance greater than 100 mm (around 42 diameters). Comparing the profiles of holdup and velocity, both quantities decrease sharply with distance from the orifice, and the decrease follows the same trend. This is not surprising, as the decrease in holdup implies more water is entrained into the plume, and as the surrounding water had a much lower velocity than the plume, the entrained water would reduce the resulting velocity of the plume. The decrease appears to be more rapid than that in miscible fluid jets (e.g., water in water), where (Robin, 2014):

$$c_c(x) = \frac{5D_o}{x} C_0 \tag{2.20}$$

$$u_c(x) = \frac{5D_o}{x} U_0 \qquad (2.21)$$

where $c_c(x)$ and $u_c(x)$ are oil holdup and velocity at the centerline; *d* is the diameter of the orifice and C_0 and U_0 are the initial oil holdup and velocity at the orifice. However, it is worth noting that Equation (2.20) and (2.21) are also approximate.

Figure 2.10c provides a comparison between the turbulence dissipation rate obtained from CFD for OwoD and OwiD. The turbulence dissipation rate for OwiD is quite close to that of OwoD generally and decreases in logarithmic scale.

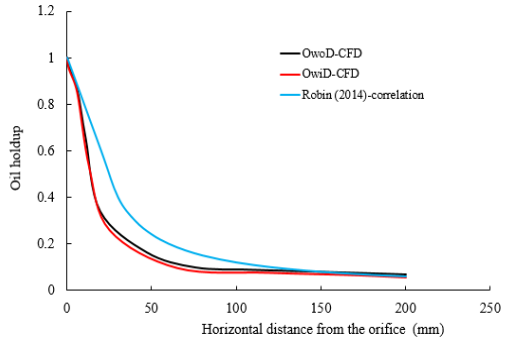

(a)

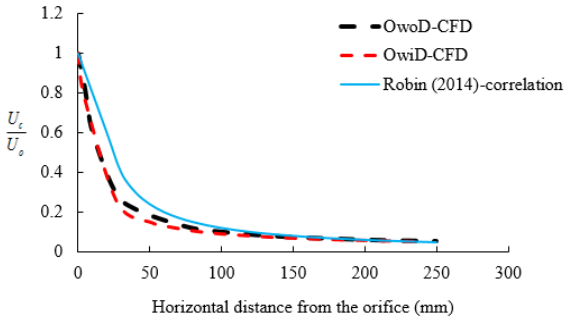

(b)

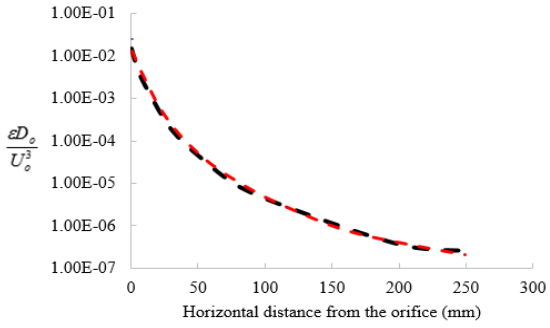

(c)

Figure 2.10 Comparison between the CFD results of OwoD and OwiD for (a) the holdup along the centerline and the correlation reads: $c_c(x) = \frac{5D_o}{x} C_0$, where $c_c(x)$ is the oil holdup along the centerline; D_o is the diameter of the orifice and c_0 is the initial oil holdup at the orifice(Robin, 2014). (b) the velocity along the centerline and the correlation read (Robin, 2014): $u_c(x) = \frac{5D_o}{x} U_0$, where $u_c(x)$ is the velocity along the centerline; D_o is the diameter of the orifice and U_0 is the initial velocity at the orifice (c) turbulence dissipation rate along the centerline.

In order to study the velocity development of jet at different distances from the orifice, we selected three cross sections along the plume trajectory as shown in Figure 2.11. The plume cross section at Surface-1 has a mean radius of 0.05 m with an area of ~0.008 m^2. The mesh size is approximately 5 mm inside the arbitrary plume boundary (i.e., bounded by the line contour of 10% of the centerline oil holdup), resulting in a total number of 314 cells inside the plume boundary at Surface-1. The plume cross section at Surface-2 has a mean radius of 0.1 m with an area of ~0.031 m^2. The mesh size is approximately 8.9 mm inside the arbitrary plume boundary, resulting in a total number of 396 cells inside the plume boundary at Surface-2. The plume cross section at Surface-3 has a mean radius of 0.135 m with an area of 0.057 m^2. The mesh size is approximately 17 mm inside the arbitrary plume boundary, resulting in a total number of 198 cells inside the boundary at Surface-3.

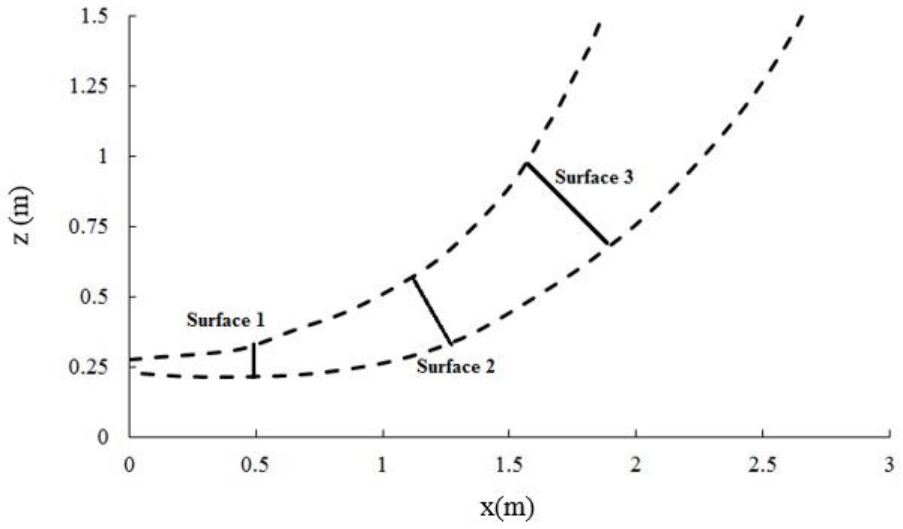

Figure 2.11 Locations of selected three cross sections along the plume trajectory. Surface-1 is centered at (x=0.5 m; z=0.27 m). Surface-2 is centered at (x=1.2 m; z=0.48 m) and makes an angle of 56 ° with respect to the horizontal direction. Surface-3 is centered at (x=1.78 m; z=0.94 m) and makes an approximate angle of 45° with respect to the horizontal direction. The dotted black lines denote the edge of the plume (which is defined where the velocity magnitude is 10 % of the centerline velocity).

Figure 2.12 shows the variation of the streamline and vertical velocity in the transverse direction (i.e., perpendicular to the plane of Figure 2.11) along with a horizontal line at z=0.27 m in Surface 1, z=0.48 m in Surface-2, and z=0.94 m in Surface-3 respectively. Figure 2.12a shows that the peak of streamline velocity was largest at Surface-1 and decreased until Surface-3, which is consistent with the decrease of the centerline velocity with distance from the source. At all surfaces, the OwoD jet produced larger streamline velocity than that of the OwiD, which is consistent with prior results. Namely that at Surface-1, the OwoD jet was narrower than that of OwiD, and thus, conservation of momentum suggests that the horizontal momentum of OwoD jet would be larger than that of OwiD. The difference in momentum from Surface-1 carried over to Surface-2 and to Surface-3. However, the difference is smaller, most likely to an increase in the relative role of buoyancy. Also, the width of the tank appears to have played a role in reducing the streamline velocity at the edges at Surface-3, where one notes sudden drops in the streamline velocity at y = 0.05 m and 0.55 m (i.e., 0.05 m from the walls).

Figure 2.12b shows the vertical velocity of the plume plotted with the goal of highlighting the role of buoyancy. At all surfaces (see Figure 2.11), the vertical velocity of OwoD was larger than that of the OwiD suggesting less entrainment of water, and thus larger buoyancy. The profile at Surface-2 indicates that buoyancy influenced the spread across the cross section of the plume, with the exception of a narrow region near the walls. The larger values in comparison to the velocity at Surface-1 reflect the conversion of the horizontal momentum at the orifice to a vertical momentum at Surface-2 and Surface-3. This is because the holdup (i.e., the volume of oil per total volume) at distances beyond Surface-2 was essentially the same, and thus the OwoD plume did not have a larger intrinsic

buoyancy than that the OwiD plume, especially for the case with the dispersant (OwiD). At Surface-3, we see the impact of the walls on both profiles, as noted by the sudden drop in velocity at y=0.05 m and 0.55 m.

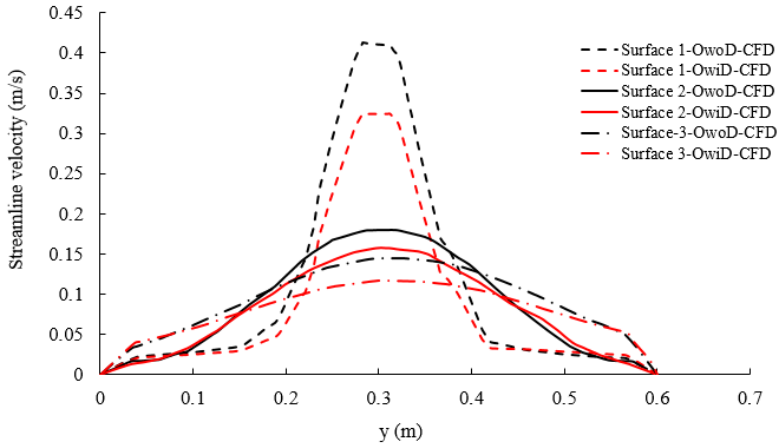

(a)

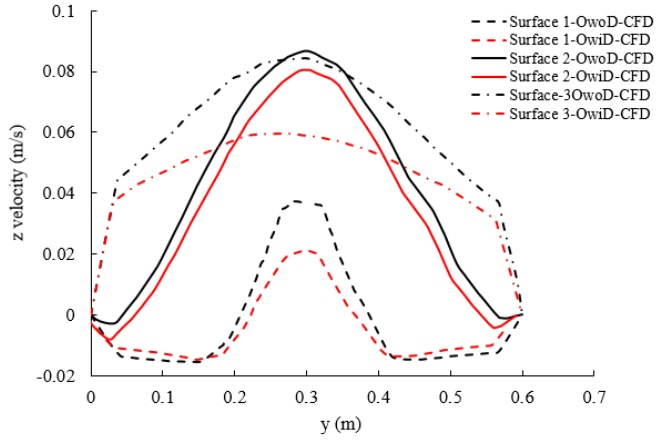

(b)

Figure 2.12 Velocity distribution in the transverse direction at Surface-1, Surface-2, and Surface-3 (see Figure 2.11) (a) streamline velocity (b) vertical velocity.

The aspect ratio, which equals the ratio of the longitudinal distance to the transversal distance at the cross section of the plume (inset of Figure 2.13) is plotted as a function of the horizontal distance from the orifice. The holdup value to determine the

aspect ratio in Figure 2.13 is 10% of the centerline holdup, which was consistently carried out in the present study. The aspect ratio is originally 1.0 and does not decrease much until 0.5 m. It then decreases in a linear fashion downstream. The decrease in the ratio indicates that the plume cross-section shape is flattened as the plume moves away from the orifice. This is consistent with the rise of the plumes and their upward curvature due to buoyancy (Figure 2.7). As these plumes need to "bend", simple conservation of mass requires that their vertical thickness (e.g., Surface-2) is reduced while horizontally increased. The aspect ratio is similar for OwoD and OwiD, which indicates that the application of dispersant had negligible influence on the jet cross section development.

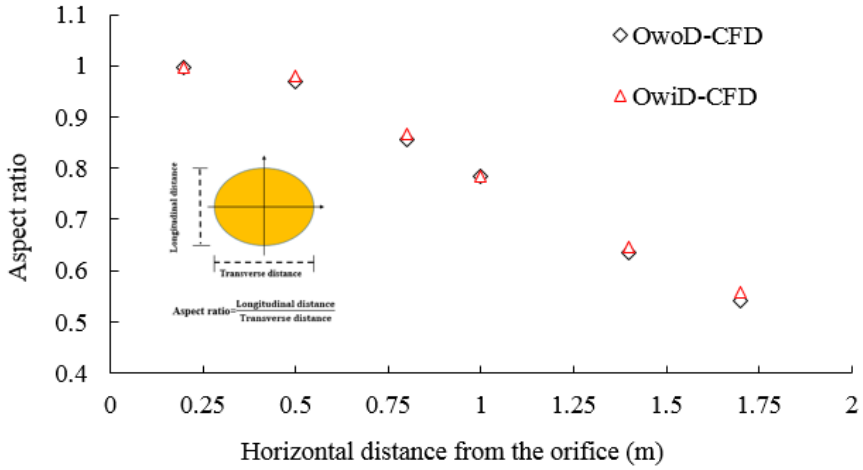

Figure 2.13 Aspect ratio (defined in inset) at various locations of the plume for OwoD and OwiD jet, respectively. The difference between the two cases is negligible through this metric (i.e., the aspect ratio).

The flatness of the plume cross section with distance can be further explained by Figure 2.14, which shows the contours of velocity and holdup (e.g., the volume fraction of oil) at Surface-3 for OwoD. One notes that the core of the plume is above the geometrical center of the plume, which is due to the larger buoyancy of the core with respect to its

surrounding fluid. The flattening engenders two major vortices with opposed signs on both sides of the plume cross-section (z=0.85 m and y=0.15 m, z=0.85 and y=0.45 m in Figure 2.14), which would tend to spread the plume further. The presence of side vortices was reported in previous works in dealing with miscible buoyant plumes (Ghoniem et al., 1993; New et al., 2006; Sykes et al., 1986).

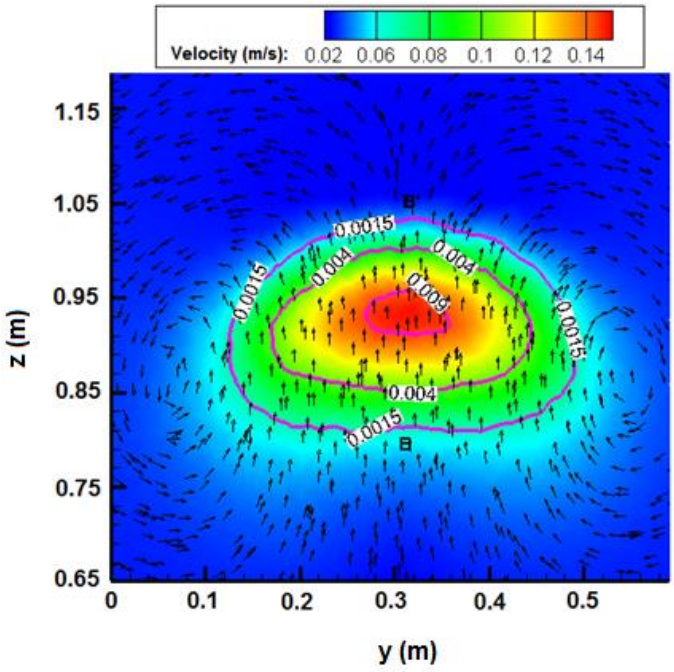

Figure 2.14 Contour lines (colors) of the velocity magnitude along with the velocity vectors (whose length is uniform herein) for Surface-3 (see Figure 2.11) looking downstream. The purple line indicates holdup (volume of oil per volume of fluids). Note the vortices with opposite signs.

The oil jet may be restricted as the width of the tank is 0.6 m such that the tank may not be wide enough for the oil jet to develop freely in the width direction. We performed a sensitivity analysis to evaluate the impact of tank width by conducting simulations with widths of 0.6 m, 2.0 m, and 10.0 m. For each of the cases, the mesh size and oil properties were the same (see Table 2.1). The only changed variable is tank width.

Figure 2.15a shows the line contour of 0.1 m/s at Surface-2. There is no obvious difference for the contour as we change the tank widths, which indicates the plume is not affected by tank width at Surface-2. Our measurements were taken at x=0.5 m from the orifice in the horizontal direction (much closer the the orifice than Surface-2) such that the results were not affected by the tank widths, in other words, the results of measurements we discussed are general and are not restricted by tank width. As a matter of fact, as we move further downstream, the tank width restricts the plume as shown in Figure 2.15b. In Figure 2.15b, the cross section of 0.6 m is quite different than that of 2.0 and 10.0 m. However, there is no significant difference for cross sections of the 2.0 m and 10.0 m width, which means that a width of 2.0 m is wide enough for the development of the jet cross section in the width direction while a tank width of 0.6 m restricts the development of jet.

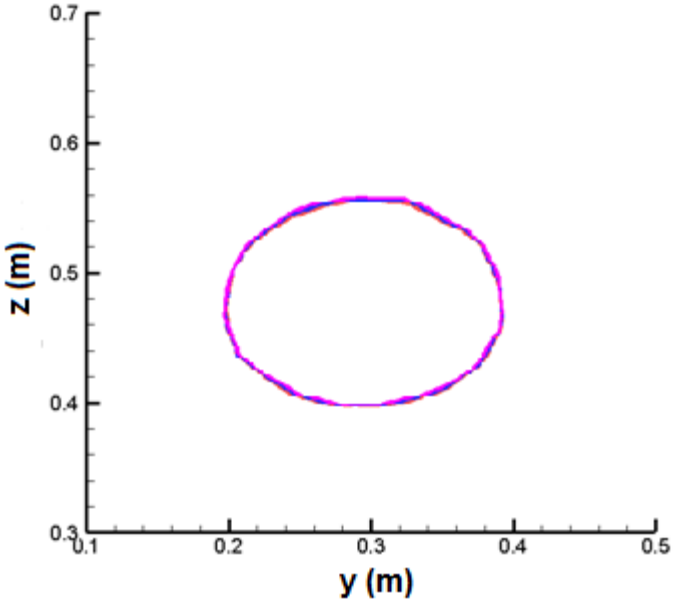

(a)

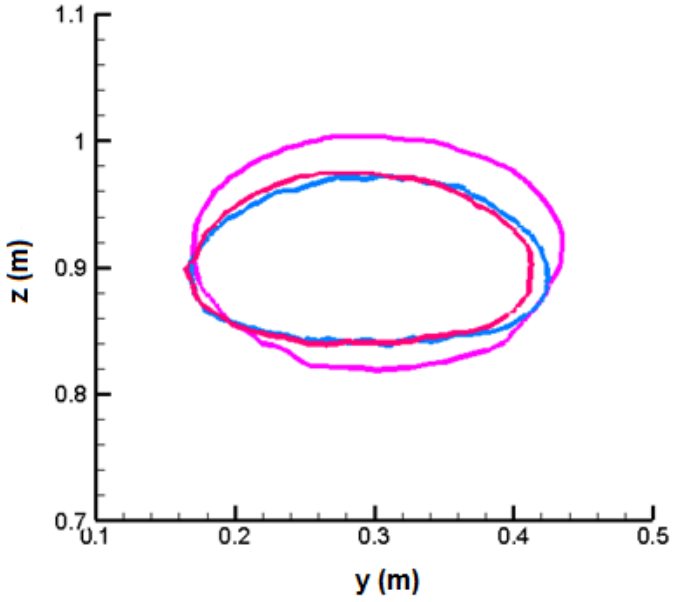

(b)

Figure 2.15 Impact of tank width on the velocity contours of 0.1 m/s (a) at Surface-2 and (b) at Surface-3 (see Figure 2.11 for locations). Three tank width were considered: The actual width of 0.6 m (purple line), a hypothetical 2.0 m width (blue line), and a hypothetical 10.0 m width (the red line). At Surface-2, in (a), there is essentially no difference between the contours. At Surface-3, in (b), the 0.6 m width tank restricts the development of the jet cross section such that it is more stretched in the vertical direction compared to the 2.0 m and 10.0 m width cases. But there was no apparent difference between the contours of the latter two. Our measurements and investigations have focused on the region upstream of Surface-2.

2.4 Conclusions

In the present study, we conducted two subsurface jet release experiments: one of oil without dispersant (OwoD) and the other one of oil premixed with the dispersant (OwiD). The jet profiles at the near to orifice region were recorded by a camera. The velocity of the fluid was measured by Vectrino Profiler. In parallel, RANS simulations were adopted with the $k-\varepsilon$ turbulent model. Simulations revealed that the influence of temperature on the oil jet was negligible as heat energy dissipated quickly, probably due to water entrainment. The salient findings are summarized in the following:

1. The jet spread angle of OwoD jet was 21° while that of OwiD was 24.0 °from the experiment measurement, which is comparable to that of the miscible jet at around 23°. This is possible because dispersant facilitated the breakup of smaller droplets and thus made the OwiD oil behave closer to a miscible jet.

2. The simulation results were able to capture the range of measured velocity, turbulence kinetic energy, and turbulence dissipation rate.

3. The OwoD jet entrained less water than the OwiD jet causing it to be more buoyant, as evidenced by the comparatively faster rise.

4. The streamline and vertical velocity at different cross sections along the OwoD and OwiD jets were evaluated. At all surfaces, the OwoD jet produced a larger streamline velocity than that of the OwiD, which is probably due to the smaller entrainment of water, that would reduce the horizontal momentum of the jet. The vertical velocity of OwoD was larger than that of the OwiD at all surfaces, consistent with less entrainment of water and thus larger buoyancy.

5. Although the OwoD velocities were larger than those of the OwiD, the turbulence kinetic energy and the turbulence energy dissipation rate of the OwoD were always smaller for the OwoD (no dispersant) than the OwiD. This is probably because the addition of dispersant (OwiD) decreased the IFT, and thus less turbulence kinetic energy was used to combat the interfacial tension force in the OwiD, resulting in a larger turbulence kinetic energy for the OwiD. This then carried over to the energy dissipation rate with higher values of the turbulence dissipation rate for the case with the dispersant (OwiD), indicating that the higher kinetic energy was converted to thermal energy (i.e., to).

6. The shape of the jet cross section changed from circular near the orifice to elliptical at mid-distance and became very stretched at far distances. For both cases, the aspect ratio (height over the width of the cross section) was initially 1.0 until around 0.5 m from the orifice, and then linearly decreased with distance. At a sufficiently far distance, which is at Surface-3, the core of the plume was above the geometrical center of the cross sections with two symmetrical vortices on both sides of the cross section, which is due to the larger buoyancy of the core with respect to its surrounding fluid.

CHAPTER 3

LAGRANGIAN PARTICLE TRACKING OF OIL DROPLETS TRAJECTORIES FOR SUBSURFACE OIL RELEASE

3.1 Introduction

The Lagrangian models are widely used a variety of applications, including atmospheric pollution (Haan, 1999), dispersion and diffusion phenomena in porous media (Ding et al., 2013), turbulent combustion (Borghi and Gonzalez, 1986) and in conditions where the particle transport or aggregation in turbulent flow is important (Toschi and Bodenschatz, 2009).

The fate of oil spilled from Deepwater Horizon Blowout is dependent on a variety of influencing factors, including transport and dispersion by the ocean circulation (Spaulding, 1988), physical weathering (e.g., evaporation and emulsification) (ITOPF, 2014), and biological consumption (Reed et al., 1999). Dimou (1992) showed that Lagrangian particle tracking with the random walking method can accurately model the oil dispersion in coaster waters by comparing with experimentally observed data. North et al. (2011) used analytical multiphase plume model with hydrographic fields of Gulf of Mexico as input to apply to the Lagrangian transport model to predict the fate of transport of oil spill and concluded that small droplets tended to form a distinct subsurface plume and remain in the water while large oil droplets rise to the surface rapidly. The presence of methane gas accompanied with oil from the initial Deepwater Horizon Blowout makes the the tracking of the movement of oil droplets more challenging. Takagi et al. (2012) showed that the rising velocity of hydrated methane was slower than that of oil droplet and crude

oil branched according to the droplet diameter and did not cluster like methane gas when a strong steady current was assumed.

Although Lagrangian models have been popularly applied in tracking the fate of oil droplets for Deepwater Horizon Blowout, most works were concentrated on the far-field instead of studying the fate of oil droplets after releasing from the orifice. In fact, the difference in the fate of oil droplets of varying sizes occurs shortly after the oil being released from the orifice, as evidenced by experimental observation (discussed later). Furthermore, all above mentioned Lagrangian approaches use analytical models to obtain the general jet/plume velocity and assume constant eddy viscosity for approximation, which does not take account of the influence of turbulence parameters in evaluating on oil droplets even though it is commonly well known that turbulent velocity significantly affects the movement of oil droplets (Chang et al., 2007; Korotenko et al., 2004; Zhao et al., 2017c).

The mitigation of oil spills depends on the trajectory and fate of oil droplets, which requires understanding the mechanisms that generate the droplets (oil dispersion including breakup and coalescence of droplets) and the mechanisms that affect their trajectories. Dissolution would tend to reduce the size of the droplets, but not in a major way. Extensive studies show that the transport and fate of oil are greatly affected by the droplet size (Brakstad et al., 2015; Chen et al., 2015; Ramseur, 2010). There is an increase in surface area due to the increasing number of small droplets, a larger surface area enhances the dissolution of hydrocarbon and oil biodegradation subsequently (Zhao et al., 2016a). Small droplets have low buoyancy such that they are more likely to remain underwater suspended by turbulence (Geng et al., 2016), while large droplets tend to rise to the water surface

rapidly (Korotenko et al., 2004). Droplets with smaller sizes are more subject to the influence of turbulence compared to larger ones (Wang et al., 2016). Although various models (Chen and Yapa, 2004b; Johansen, 2000; Zhao et al., 2015; Zheng et al., 2003) and field experiments (Chen and Yapa, 2003; Johansen, 2003) were carried out to study the impact and physics of oil spills, few have considered the comprehensive forces exerted on the droplets which may influence the movement of single oil droplets under turbulence.

In the present study, an underwater oil release experiment in the Bedford Institute of Oceanography flume tank was conducted, whose detailed information is presented in Chapter 2. In this chapter, a Lagrangian Particle Tracking (LPT) model is developed to trace the trajectories of individual droplets of various diameters by accounting for the effect of turbulence and physical forces (e.g., gravitational force, buoyancy force, drag force, lift force, add mass force. etc.), coupling with velocity field obtained from computational fluid dynamics (CFD) simulation.

3.2 Methodology

The individual motion of oil droplets (dispersed flow) in water (continuous flow) is modeled by a Lagrangian approach, in which the movement of each droplet is determined by solving a set of ordinary differential equations along its path. This approach is suitable to model two phase flows with relative low particle concentration with non-uniform properties (Joao et al. 2010), as in the present work.

The equations for calculating the oil droplet location are defined in the following (Geng et al., 2014):

$$X_d' = X_d + U_d \Delta t + R\sqrt{2D\Delta t} \tag{3.1}$$

where X_d' is the coordinates of the droplet at the next time level. X_d and U_d are the coordinates and velocity of the oil droplets at the current time level, respectively, which are given as $X_d = (x, y, z)_d$ and $U_d = (\mathrm{u}, \mathrm{v}, \mathrm{w})_d$. The subscript "*d*" denotes droplet. The third term on the RHS of Equation (3.1) represents the impact of turbulence on the subscale movement of the oil droplet, which is accounted as a random walk process, where R represents a random number generated from a Gaussian distribution with a mean of 0 and a variance of 1.0. Δt is time step. D is eddy diffusivity, which is calculated as:

$$D = 0.09\frac{k^2}{\varepsilon} \tag{3.2}$$

in which k is turbulent kinetic energy and ε is turbulent dissipation rate, both are obtained CFD (e.g., RANS model) described above.

The oil droplets are subject to comprehensive forces based on Newton Second Law:

$$m_o \frac{d}{dt}(U_d) = F_g + F_b + F_l + F_a + F_d \tag{3.3}$$

m_o is the mass of oil droplet. All relevant forces are expressed on the RHS of Equation (3.3): F_g is the gravitational force, F_b is buoyancy force due to oil droplet and water density difference, F_l is lift force, F_a is added mass force, and F_d is drag force.

Sridhar and Katz (1995) show that the basset force, which is a historical term, is quite small and thus the basset force was neglected in equation (3.3) in the present study.

The gravitational force F_g is given by the following assuming oil droplet is of spherical shape:

$$F_g = \frac{1}{6}\pi\rho_o D_d^3 g \tag{3.4}$$

where ρ_o is oil density, $\mathrm{D_d}$ is droplet diameter and g is gravity. Gravitational force points downward and is assigned as positive. The oil droplet is considered as immiscible discrete phase, the buoyancy force due to the density difference between oil droplets and the surrounding liquid is given by:

$$F_b = -\frac{1}{6}\pi\rho_w D_d^3 g \tag{3.5}$$

where ρ_w is water (continues) density, taken as 998. 2 kg/m^3 in the present study.

F_l is expressed as follows (Joao Pinto, 2010):

$$F_l = \frac{\pi}{8}\rho_w D_d^3 C_l[(U - U_d)\times\omega] \quad (3.6)$$

in which ρ_w is water (continuous phase) density, *U* is the local velocity of the surrounding water (continuous phase). D_d is oil droplet diameter, C_l is the lift coefficient, which usually varies between 0.01 for very viscous fluid and 0.5 for inviscid fluid (Burlutskiy and Turangan). We take C_l as 0.1 in the present study. ω is vorticity and reads as:

$$\omega = \nabla \times U \quad (3.7)$$

F_a accounts for the acceleration of oil droplet due to its movement through the surrounding water volume, which is expressed as the following (Tomiyama, 1998):

$$F_a = C_a m_w \left(\frac{dU}{dt} - \frac{dU_d}{dt} \right) \quad (3.8)$$

with $C_a = 0.5$, taken as a constant (Lucas et al., 2005) and m_w is the mass of water taking the same volume as the oil droplet.

F_d accounts for the resistance acting in the opposite direction of moving oil droplet with respect to water (Miller et al., 1998):

$$F_d = \frac{f_d}{\tau_d}(U - U_d)m_o \quad (3.9)$$

where m_o is the mass of oil droplet and τ_d is the Stokes drag coefficient given as:

$$\tau_d = \frac{\rho_o * D_d^{\,2}}{18 * \mu_o} \tag{3.10}$$

The variable f_d is a correction for the Stokes coefficient to account for situations where the flow is not laminar, which is calculated based on Miller et al. (1998):

$$f_d = 1 + 0.0545 \mathrm{Re}_d + 0.1\sqrt{\mathrm{Re}_d}\,(1 - 0.03\mathrm{Re}_d) \tag{3.11}$$

where where Re_d are defined as follows:

$$\mathrm{Re}_d = \frac{\rho_w D_d \mathrm{u}_s}{\mu_w} \tag{3.12}$$

where μ_w is water dynamics viscosity and u_s is slip velocity.

By incorporating Equation (3.4)-(3.12) into Equation (3.3) using single step forward Euler scheme for time stepping.

In the present work, Inverse Distance Weighted Method (IDVM) was used to interpolate the local flow velocity within space, in which the local flow velocity (U) at is obtained as the average of the velocity of the whole domain weighed by the inverse distance to a selected power:

$$\mathrm{U}_j(x_d, y_d, z_d) = \sum_{i=0}^{N} \frac{\theta_i \mathrm{U}_{ji}}{\sum_{j=0}^{N} \theta_i \mathrm{U}_{ji}}, \quad \theta_i(x) = \frac{1}{d^p}, \quad j = x, y, z \tag{3.13}$$

where d is the distance from the oil droplet position to an arbitrary node in the CFD computational domain. p is a selected power, which is normally taken as 2.0.

3.3 Results and Discussion

During the subsurface oil release experiment (see Chapter 2), it is noticed that some oil droplet exit the boundary of the plume and continue to rise up to the water surface, as shown in Figure 3.1. The possible explanation is that the physical forces exerted on oil droplets are dependent on diameter such that the trajectories of oil droplets vary with droplet diameter. A similar observation was reported in (Zhao et al., 2016b) as well.

Figure 3.1 Crude oil plume cross-section captured by the high resolution camera at the 4.0 m downstream of the jet orifice. Some oil droplets exit the upper boundary of the plume and continue to rise up (see the details within the white box in the figure).

Figures 3.2 shows the distribution of droplets at the cross section located at x=1.8 m with a radius of 0.2 m, for droplets with a diameter of 100 um, 250 um and 500 um. The selection of the 100 um and 250 um droplets was because the majority of the droplets for the oil only case were less than 250 um, while 500 um was taken to illustrate the impact of buoyancy. To obtain better statistics, over 800 droplets for each size were released from the orifice and tracked along the plume.

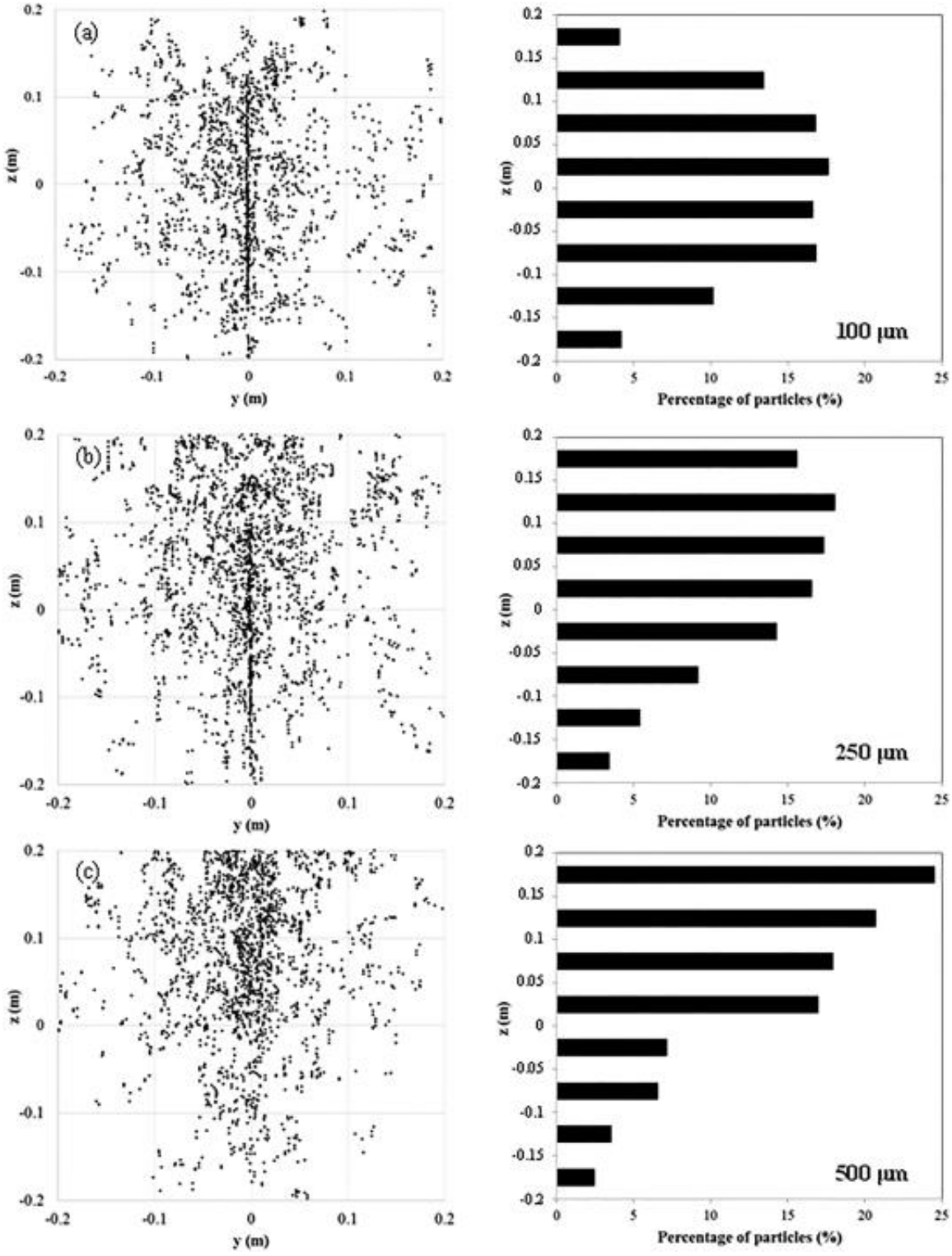

Figure 3.2 Distribution of oil droplets at the cross section located at x = 1.8 m predicted by the integration of the particle tracking NEMO3D model and RANS simulation for jet and plume: (a) 100 *um* droplets; (b) 250 *um* droplets; and (c) 500 *um* droplets.

The zero point presents the center of the cross section. Over 800 droplets were tracked for each size. The left panel shows the distribution of the droplets over the cross section, while the right panel shows the percentage of the droplets over the vertical position z.

For the 100 um droplets (Figure 3.2a), the droplets were evenly distributed over the cross section; the percentage of droplets at upper and lower portion of the plume was essentially the same (right panel of Figure 3.2a). This suggests that the buoyancy of each droplet was not strong enough to overcome the forces of inertia due to turbulence. For 250 um droplets (Figure 3.2b), the droplets are also spread over the entire cross section, with slightly more droplets ended up at the upper portion. The percentages at the upper and lower portion of the plume are 67% and 33%, respectively. The effect of buoyancy of individual droplets seems to become major for 500 um droplets (Figure 3.2c), where most of the droplets were in an upper portion of the plume (around 80%), and some droplets were outside of the upper plume boundary (not shown in Figure 3.2c).

Figure 3.3 shows the time series of the vertical component of physical forces (F_o , e.g., buoyancy force, lift force, drag force, added mass force) over a single droplet, scaled by gravitational force. For droplets less than 500 μm in diameter, the added mass force is almost negligible, as shown in Figure 3.3a and 3.3b. Even for large droplets with 500 μm in diameter, the added mass force is around 17 % of the buoyancy force of droplet. The scaled buoyancy force is a straight-line with no mass transport and maintains constant oil droplet density. The scaled lift force is negligible although it slightly increases as droplet diameter increased to $500\,\mu m$. It indicates the main contributing forces in the process of

rising up of the oil droplet are buoyancy force and drag force based on the observation in Figure 3.3.

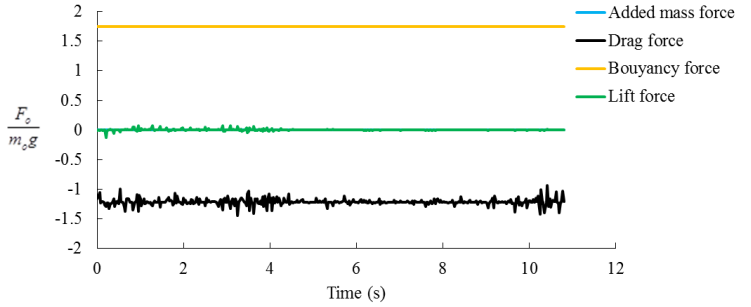

(a)

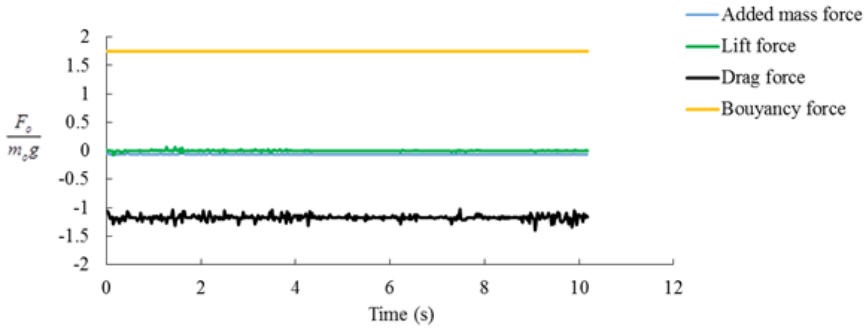

(b)

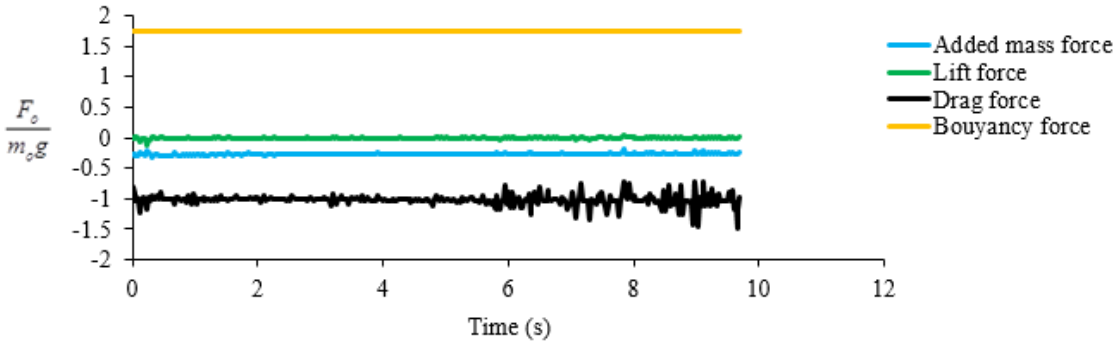

(c)

Figure 3.3 Time series of the vertical component of the dimensionless physical forces over a single droplet (a) 50 μm in diameter (b) 200 μm in diameter (c) 500 μm in diameter. Note the physical forces are scaled by gravity.

It is worth noting that the 3D flow velocity of the jet and plume in the present study was predicted by means of RANS simulation, which only provides an average behavior of the plume dynamics. But, as observed, the plume itself exhibited large eddies and puffs (Figure 3.4) at a distance of around 1.0 m above the orifice, which is characteristic of buoyancy and turbulence. These eddies carried the droplets in all directions inside the plume. Such behavior could not be fully captured by the RANS simulation, and the 250 *um* droplets are likely more evenly distributed across the plume than the one shown in Figure 3.2b. To fully resolve the droplet movement in the subsurface oil plume due to eddies and puffs, more sophisticated CFD models are needed, such as Large Eddy Simulations (LES).

Figure 3.4 Image of oil jet engulfing at the downstream during the experiment (oil with dispersant). Large eddies and puffs were formed and likely increase the mixing of droplets in comparison to that provided by the Reynolds Average Navier Stokes (RANS) simulations.

3.4 Conclusions

In the present study, we observed that some oil droplets exited the boundary of the plume and continue to rise up depending on its own buoyancy although most oil droplets stay within the oil plume from the subsurface oil release experiment. That is possible because larger oil droplets have the larger buoyancy to overcome the turbulence mixing energy while smaller droplets are more likely to be uniformly mixed within the oil plume. The experimental observation further substantiated the necessity to account for the individual droplet movement by considering the comprehensive physical forces on the droplets.

The Lagrangian particle tracking (LPT) method that coupled with Computational Fluid Dynamics (CFD) simulation by considering the comprehensive forces on oil droplets of different diameters, including the gravitational forces, buoyancy force, lift force, drag force, and added mass force.

By tracking the location of individual droplets, it was found that oil droplets less than 100 um would mix uniformly in the plume, while those equal 500 um tend to be above the centerline of the plume. Droplets that are 250 um seem to be slightly biased upward. The relative importance of different forces was evaluated by LPT model and was concluded that the two major contributing forces are the buoyancy force and drag force. The added mass force becomes considerable when the droplet size is large (e.g., 500 um) while the lift force is negligibly small.

CHAPTER 4

LARGE EDDY SIMULATION OF THE OIL AND GAS FLOW FROM DEEPWATER HORIZON BLOWOUT

4.1 Introduction

The production and transportation of crude oil in the pipe from offshore drilling contain a fraction of natural gas (mostly methane). The crude oil transported from the riser is subjected to high pressure and temperature and thus the crude oil is in the gas-saturated state with the solution gas in oil and some gas in the separated gas phase. The companion of gas might influence the overall hydrodynamics of the oil plume with varying the GOR (gas to oil ratio). What is more challenging is providing the quantitative analysis of the impact of gas phase on the hydrodynamics of the oil plume for the Deepwater Horizon oil spill incident, which is important to understand what role the gas phase has played in the oil plume as it might allow us to re-estimate the total oil discharged to the ocean from the Deepwater Horizon oil spill.

It is estimated that between 3.26 to 5.0 million barrels of crude oil with a companion of between 1700 to 3600 tons of gas per day were released by the Deepwater Horizon oil spill incident (Camilli et al., 2012b; McNutt et al., 2012; Valentine et al., 2012).

Researchers have performed multiphase (e.g., gas and water) in the laboratory experiment scale to study the influence of the inclusion of the gas phase on the plume hydrodynamics. Milgram (1983) performed bubble plume release from with varying flowrates and found that the entrainment coefficient increases with the increasing volume fraction of the gas. The gas phase increases the turbulent velocity and intensifies the mixing from the entrainment interface to the plume centerline. Iguchi et al. (1992) performed air-

water mixture injection of the jet in a cylindrical water bath and found that the air volume fraction has a negligible effect on the axial water velocity whereas turbulence production was increased due to the increasing gas volume fraction. This was expected as the increasing air volume fraction is able to cause more chaotic flow behavior as the air bubbles tumble around in the water volume. A subsequent experiment further revealed that the turbulence production in the wake of the air bubbles to be approximate two times of the turbulence production compared to the single phase jet (Iguchi et al., 1995).

Most of the related research work was done in a lab scale while Deepwater Horizon Blowout is in a complicated underwater environment down 2000 m below the ocean surface with high pressure and temperature. Given the difficulties in experimentally measuring the Deepwater Horizon Blowout, a numerical simulation approach was performed to study how the gas phase influence the overall oil plume hydrodynamics. Large Eddy Simulation (LES) approach was used to simulate the gas and oil plume hydrodynamics in order to maintain high accuracy with capturing the small scale turbulence structure under unsteady state, with a special focus on the near-to-orifice region (e.g., within five diameters downstream from the riser orifice).

The flow rate estimation was mostly focused on the Mississippi Canyon Macondo Well (MC 252). The oil and gas were released mainly from a 200 m long broken riser on the seafloor, whose riser was cut at the wellhead on June 3rd, 2010 such that the oil and gas were directly blowout from the cut wellhead.

The reported gas to oil ratio (GOR) was 1600 scf/stb (standard cubic foot/barrel) (Reddy et al., 2012). Converting to SI unit, one finds the follows,

$$1600 scf / stb = 285 m^3 / m^3 \tag{4.1}$$

The dissolved gas was estimated to be 623 scf/stb (Zhao et al., 2017a). Thus, the remaining volume of gas in the separate gas phase was (1600-623) scf/stb=977 scf/stb=174 m^3 / m^3.

Under both standard and Deepwater Horizon Blowout conditions, the mass of oil and gas is conserved, one has:

$$\frac{\dot{m}_{gas-std}}{\dot{m}_{oil-std}} = \frac{\dot{m}_{gas-DWH}}{\dot{m}_{oil-DWH}} \tag{4.2}$$

where $\dot{m}_{gas-std}$ and $\dot{m}_{oil-std}$ are the gas and oil mass rates under standard condition, respectively. And $\dot{m}_{gas-DWH}$ and $\dot{m}_{oil-DWH}$ are the gas and oil mass rates at 1500 m depth of Deepwater Horizon Blowout local condition.

Equation 4.2 can be written as:

$$\frac{\dot{\mathrm{V}}_{\text{gas-std}}}{\dot{\mathrm{V}}_{\text{oil-std}}} \cdot \frac{\rho_{gas-std}}{\rho_{oil-std}} = \frac{\dot{\mathrm{V}}_{\text{gas-DWH}}}{\dot{\mathrm{V}}_{\text{oil-DWH}}} \cdot \frac{\rho_{gas-DWH}}{\dot{\mathrm{V}}_{\text{oil-DWH}}} \tag{4.3a}$$

$$174 \cdot \frac{0.656 kg / m^3}{820 kg / m^3} = \frac{\dot{\mathrm{V}}_{\text{gas-DWH}}}{0.08 \mathrm{m}^3 / s} \cdot \frac{135 kg / m^3}{662.6 kg / m^3} \tag{4.3b}$$

where $\dot{V}_{\text{gas-std}}$ is the gas flow rate under standard pressure and temperature, $\rho_{gas-std}$ is the density of gas under standard condition, $\dot{V}_{\text{oil-std}}$ is the flow rate of oil under standard condition, $\rho_{oil-std}$ is the density of oil under standard condition, $\dot{V}_{\text{gas-DWH}}$ is the flow rate of gas under Deepwater Horizon Blowout, $\rho_{gas-DWG}$ is the density of gas under Deepwater Horizon Blowout condition, $\dot{V}_{\text{oil-DWH}}$ is the flow rate of oil under Deepwater Horizon Blowout condition, $\rho_{oil-DWH}$ is the density of oil under Deepwater Horizon Blowout condition. This gives $\dot{V}_{\text{DWH-gas}} = 0.055 m^3/s$.

The pipeline outlet cross-section (*A*) with a diameter of 0.5 m gives:

$$A = 3.14 \cdot \left(\frac{0.5}{2}\right)^2 = 0.2 m^2 \tag{4.4}$$

The superficial gas velocity ($v_{\text{gas-DWH}}$):

$$v_{\text{gas-DWH}} = \frac{\dot{V}_{\text{gas-DWH}}}{A} = \frac{0.055 m^3/s}{0.2 m^2} = 0.275 m/s \tag{4.5}$$

On June 3rd, 2010, the riser was cut above the BOP and before the Riser Kink Jet, the oil discharge rate was reported as 7100 m^3/day (equivalent to 0.08 m^3/s) from the post-cut vertical riser (FRTG, 2011).

The superficial velocity of oil ($v_{\text{oil-DWH}}$, the horizontal axis in Figure 3.1b) under the Deepwater Horizon Blowout condition:

$$v_{\text{oil-DWH}} = \frac{\dot{V}_{\text{oil-DWH}}}{A} = \frac{0.08 m^3/s}{0.2 m^2} = 0.4 m/s \tag{4.6}$$

Therefore, the oil and gas mass rate under the Deepwater Horizon Blowout condition:

$$\dot{m}_{oil-DWH} = \rho_{oil-DWH} \dot{V}_{\text{oil-DWH}} = 662.6 kg/m^3 \cdot 0.08 m^3/s = 53.008 kg/s \tag{4.7}$$

$$\dot{m}_{gas-DWH} = \rho_{gas-DWH} \dot{V}_{\text{gas-DWH}} = 135 kg/m^3 \cdot 0.055 m^3/s = 7.425 kg/s \tag{4.8}$$

The oil and gas flow is in the vertical riser at Deepwater Horizon condition is similar to the multiphase flow in many chemical reactors. The multiphase flow of oil and gas can be categorized into four classes based on visual observation of the flow mechanism, as shown in Figure 4.1a.

Bubbly flow occurs at a low gas flow rate in which the gas phase presents in discrete and uniform bubbles in the continuous liquid phase. As the gas flow rate is increased, the gas phase presented in the continuous liquid phase appear as bullet shaped bubbles, which is called “slug flow”. As the gas flow rate continues to increase, the gas phase displays highly chaotic and disordered characteristics with oscillating instability. When the gas flow rate is completely dominant, the annular flow occurs with the continuous liquid phase form a thin film on the wall and the gas phase flows in the gas core with liquid phase droplets entrained.

Figure 4.1 shows the flow regimes map based on the superficial velocity of the liquid and gas phase, where the shaded areas indicate the transitional zones between

different flow regimes. It can be determined that the oil and gas flow in the vertical riser under the DHW condition is "churn", which is indicated by the blue dot in Figure 4.1. The calculated gas superficial velocity (e.g., gas flow rate divides the cross sectional area of the riser) is 0.3 m/s and the liquid superficial velocity is 0.4 m/s (see Equations 4.1-4.8). McNutt et al. (2011) concluded that the oil flow rate was 0.055-0.074 m^3/s for the post riser cut operation (after June 3rd, 2010), which is equivalent to 0.3-0.4 m/s for the oil velocity. In addition, the estimated oil superficial velocity of 0.4 m/s (equivalent to 0.08 m^3/s) in the present study is comparable to the "best-estimate" oil flow rate of 0.064-0.083 m^3/s for the poster riser cut operation after June 3rd, 2010.

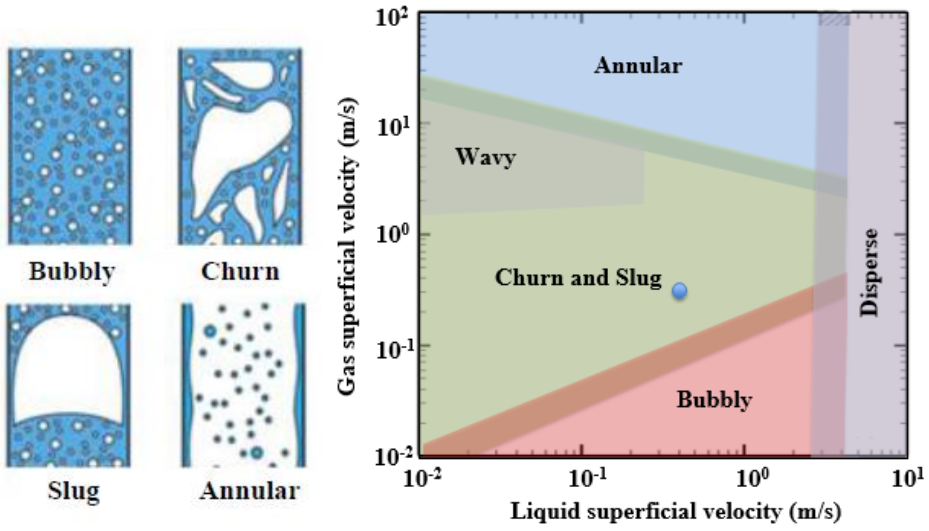

Figure 4.1 (a) Schematic view of the flow regimes (bubbly, slug, churn and annular) in a vertical pipe (b) Flow map adapted from (Weisman, 1983) in which the blue dot indicates the Deepwater Horizon condition and the dark strips indicates the transition zones between regimes.

4.2 Methodology

In the present study, we used Large Eddy Simulation (LES) within the model FLUENT to investigate the oil and gas plume from the riser, including the flow (e.g., oil and gas phases) interaction with the surrounding water after blowout from the riser orifice with a main focus on the near-field flow. In LES, we assume the oil and gas phases are incompressible and the densities of water, oil, and gas are constant for approximation.

The three dimensional computational domain mainly consists of the cylindrical volume of 30 m in diameter and 14 m in height with 14.5 million nodes in total. The riser is simplified by another cylindrical volume of 0.5 m in diameter and 4 m in length, as shown in Figure 4.2. The mesh size of the near-to-orifice region is 4 mm and the mesh size gradually increases to 8 cm downstream. The simulation was run with a constant time step of $2*10^{-4}$ s to ensure the global courant number is less than 1.0 to ensure the simulation stability. The simulation was run in parallel with 48 cores on the high performance computing server of Center of Natural Resources at New Jersey Institute of Technology.

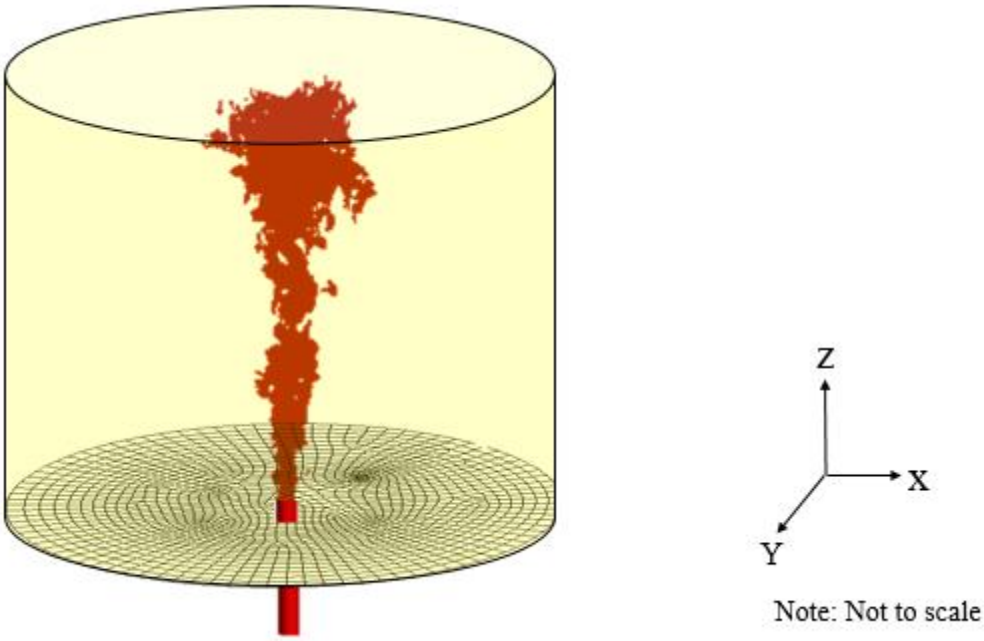

Figure 4.2 3D view of the computational domain. The domain is cylindrical in shape. The riser is 2 m above the bottom and 2 m below the bottom (i.e., 4 m in length). The cylindrical domain is 30 m in diameter and 14 m in height (e.g., 12 m above the orifice). The domain consists of 14.5 million nodes and the time step was $2*10^{-4}$ s.

The bottom of the cylindrical shape is considered as the seabed, which is assigned as wall boundary condition. The lateral surface and the top surface of the cylindrical shape are assigned as hydrostatic pressure boundary condition.

The turbulent boundary condition at the inlet of the riser for the LES simulation started from a steady state RANS (Reynolds Averaged Navier Stokes) in a 20 m portion of the pipe at the same mesh resolution. Within the RANS simulation, the inlet boundary condition was that of the oil and gas discharge velocities, and the energy dissipation rate was estimated at $\varepsilon_0 = \frac{0.003D_0}{U_0^3}$, where ε_0 is the turbulence dissipation rate, D_0 is the diameter of the pipe, and U_0 is the inlet velocity (Zhao et al., 2014). The energy dissipation

rate at 10 m from the RANS inlet obtained at the steady state of the RANS was used as upstream (or inlet) boundary condition for the LES simulation in the 4.0 m pipe.

Large eddy simulation (LES) calculates the large eddies by solving the Navier Stokes equations and accounts for the small eddies (e.g., smaller than the filter length) by using a sub-grid scale (SGS) model (Sagaut, 2005). We used the Volume of Fluid (VOF) method to account for the gas, oil and water phases (Hirt and Nichols, 1981).

In this work, the flow is incompressible and the filtered equations read:

$$\frac{\partial \bar{u}_i}{\partial t} + \bar{u}_j \frac{\partial \bar{u}_i}{\partial x_j} = -\frac{1}{\rho}\frac{\partial \bar{p}}{\partial x_i} + \frac{\partial}{\partial x_i}\left(\nu \frac{\partial \bar{u}_i}{\partial x_j}\right) + \frac{1}{\rho}\frac{\partial \tau_{ij}}{\partial x_j} \tag{4.9}$$

where u is velocity, p is pressure, ρ is density, ν is kinematic viscosity and τ_{ij} is the sub-grid stress, given by:

$$\tau_{ij} = \bar{u}_i \bar{u}_j - \overline{u_i u_j} \tag{4.10}$$

Smagorinsky model is adopted for the sub-grid scale. The traceless part of the SGS stress, $\tau_{ij} - \frac{1}{3}\delta_{ij}\tau_{kk}$, can be related to the strain rate, S_{ij}, of the resolved velocity field using the Boussinesq hypothesis for the combined phases (ANSYS, 2009; Stefano et al., 2008):

$$\tau_{ij} - \frac{1}{3}\delta_{ij}\tau_{kk} = -2\nu_{SGS}\overline{S_{ij}} \tag{4.11}$$

$$\overline{S_{ij}} = \frac{1}{2}\left(\frac{\partial \overline{u_i}}{\partial x_j} + \frac{\partial \overline{u_j}}{\partial x_i}\right) \tag{4.12}$$

ν_{SGS} in Equation. (4.11) is the sub-grid eddy viscosity, which can be written as:

$$\nu_{SGS} = \left(C_s \Delta\right)^2 \left|\overline{S}\right|^2 \tag{4.13}$$

$$\overline{S} = \sqrt{2\overline{S_{ij}}\,\overline{S_{ij}}} \tag{4.14}$$

C_s is a Smagorinsky constant, taken as 0.1 in the present simulation.

The total dissipation rate, ε, is composed of viscous ε_ν and sub-grid scale ε_{SGS} (Chumakov, 2005):

$$\varepsilon = \varepsilon_\nu + \varepsilon_{SGS} \tag{4.15}$$

The viscous ε_ν is calculated as:

$$\varepsilon_\nu = 2\nu\overline{S_{ij}}\,\overline{S_{ij}} \tag{4.16}$$

where S_{ij} is the strain rate tensor defined above.

The sub-grid scale energy dissipation rate ε_{SGS} is calculated as:

$$\varepsilon_{SGS} = 2\nu_{SGS}\overline{S_{ij}}\,\overline{S_{ij}} \tag{4.17}$$

where ν_{SGS} denotes the sub-grid eddy viscosity based on the Smagorinsky model.

The computational domain was discretized using approximately 14.5 million nodes. The spacing varied from 0.005 m within the riser to 0.15 m at 5 m away from the orifice. The interfacial tension (IFT) between oil and water was estimated at 20 mN/m for DWH blowout simulation (McNutt et al., 2011) by using the continuum surface force (CSC) approach in which the interfacial force is transformed into a volume force at the interface (Francois and Sicilian, 2007).

4.3 Results and discussion

Figures 4.3 shows photos of the Macondo wellhead with fluids emanating from it (Video was obtained from NOAA Natural Resources Damage Assessment, Dr. Lisa Di Pinto). The oil plume at the near-to-orifice region exhibit violent turbulent structures with vortices pairing and rolling up.

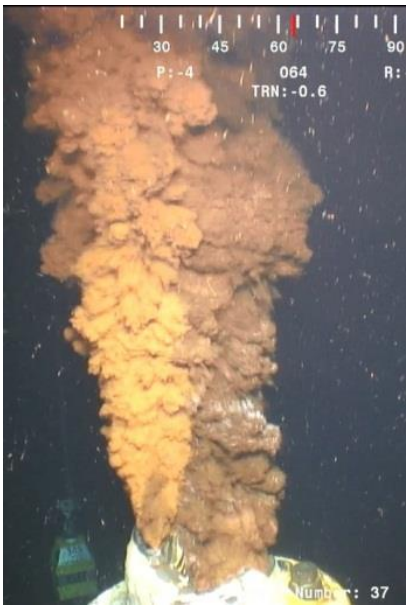

Figure 4.3 Image of the Macondo 252 wellhead on June 3rd, 2010 (courtesy from Dr. Lisa Di Pinto, NOAA).

Figure 4.4 shows the oil holdup (e.g., the volume of oil per total volume of a given cell) and gas holdup (e.g., the volume of gas per total volume of a given cell) obtained from the simulations of churn flow and bubbly flow are reported at two times. The holdup distribution for the churn flow shown in Figure 4.4a was more granular than for bubbly flow shown in Figure 4.4b, resembling far more closely the Deepwater Horizon Blowout plume appearance (see Figure 4.3).

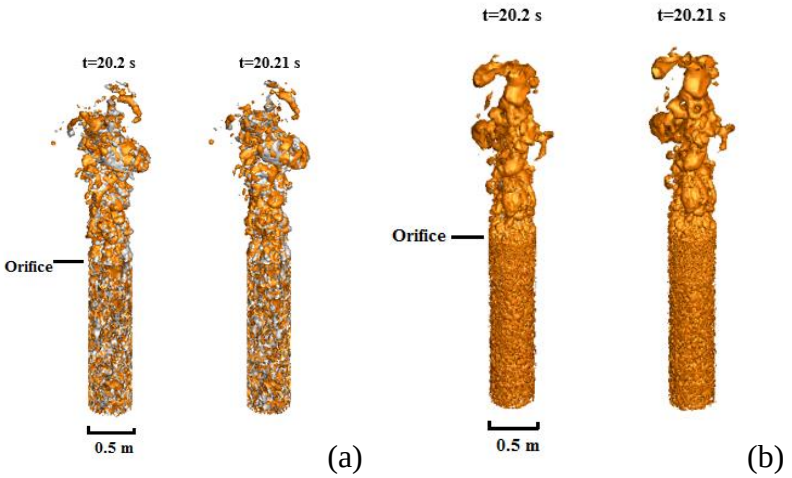

Figure 4.4 Simulated oil holdup (orange) and gas holdup (gray) at two consecutive time levels for the churn and bubbly flow, respectively. The oil holdup threshold=0.2 and the gas holdup threshold=0.04. The simulated churn flow plume appeared more "grainy", similar to the photo of the actual plume (Figure 4.3). The bubbly plume appears smoother than the churn one.

Figure 4.5 shows the zoom-in of the oil and gas holdups for the churn and bubbly plumes at three consecutive time levels with a time interval of 0.005 s. In Figure 4.5a, big gas bubbles strongly interact with oil blobs for the churn flow. Unlike the bubbly flow, the gas bubbles in the churn one have a significant influence on the breakup of oil blobs. One oil blob was attached to the gas bubble in the near-to-orifice region at t=20.2 s as indicated by the dashed rectangular shape for the zoom-in view, the oil blob was elongated by the force exerted by the gas bubble at t=20.205 s and a small oil blob was peeled off from the big one due to the gas bubble attached to the tip of the oil blob. Another example can be taken from the one in the solid rectangular shape for the zoom-in view as the oil blob was attached to two gas bubbles at t=20.2 s. The oil blob was pulled by the larger buoyancy or turbulence of the gas bubbles and that oil blob finally broke into two at t=20.21 s. It is likely that the oil blob breakup was mainly due to turbulence for the bubbly flow while the

oil blob breakup in the churn flow was due to the effect of turbulence and the influence of gas bubbles.

As can be noticed in Figure 4.5b, small and separate gas bubbles, whose holdup is colored by gray, are mixed with the oil in the near-to-orifice region. The oil, whose holdup is colored by orange, continuously breaks into smaller ones as it is released from the orifice. The oil blob in the dashed rectangular shape was one body at t=20.2 s and was about to pinch off at t=20.205 s, and finally broke into two smaller blobs at t=20.21 s.

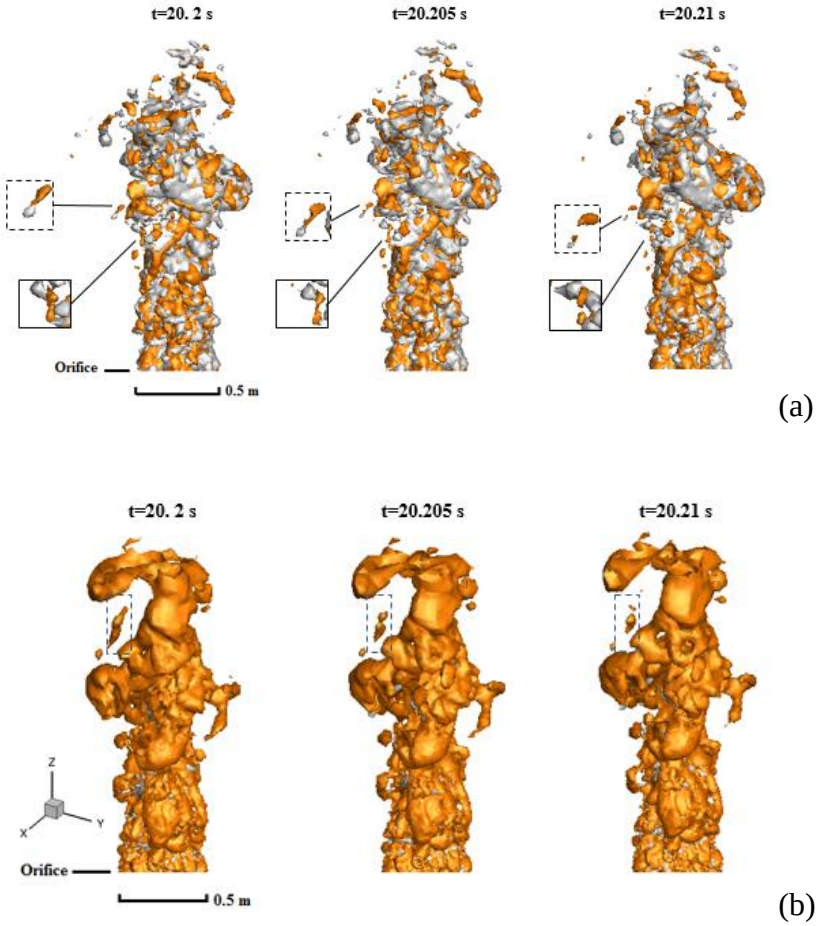

Figure 4.5 Zoom-in oil holdup (orange) and gas holdup (gray) for the churn and bubbly plumes at three consecutive time levels.

Figure 4.6 shows the q-criterion (to visualize the vortices) colored by z velocity at three consecutive time steps for the bubbly and churn flow, respectively. The fully three-dimensional coherent vortex structure and strong vortex interaction were observed. Compared with the bubbly flow, the churn one is visually wider for vortex in all consecutive time steps.

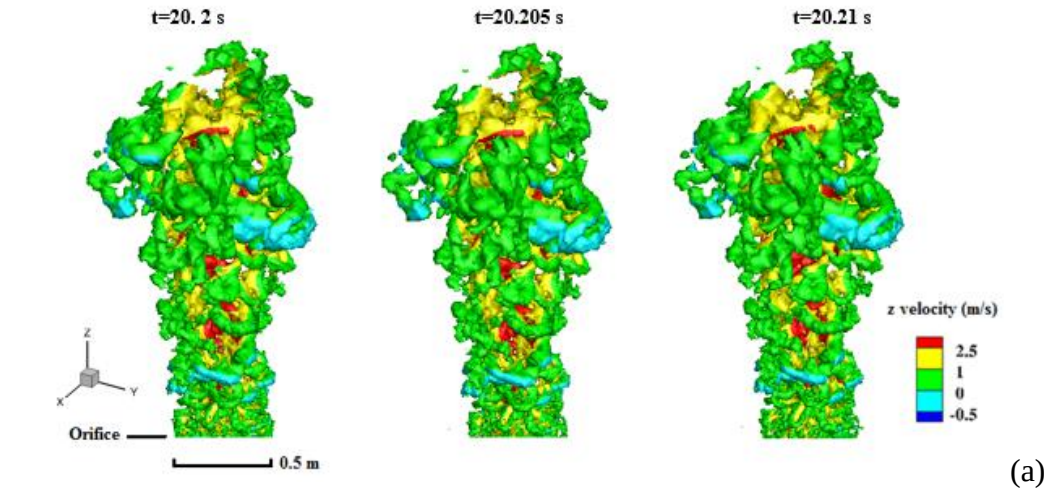

(a)

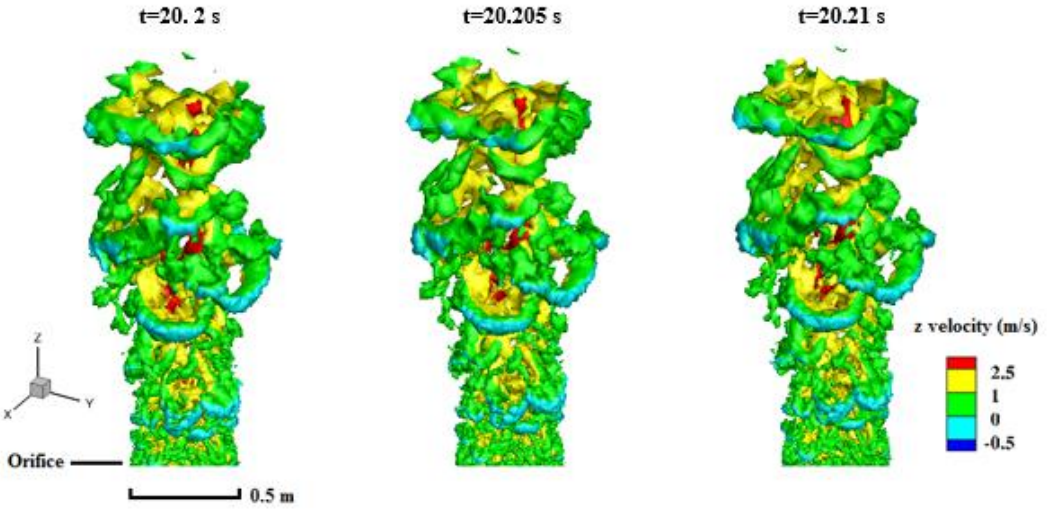

(b)

Figure 4.6 Q-criterion, whose threshold is 10, colored by z velocity for the (a) churn plume and (b) bubbly plume.

Figure 4.7a shows the velocity contour of the churn plume in the middle plane. The plume was compared with a constant angle of 1:10.5 as indicated by the dashed line. Negative velocity could be noticed at the edge of the plume, which might be the result of the tumbling characteristics of the churn flow as the infinite instability of the churn flow introduces downward velocity within the riser and the trend of the downward velocity continue to exist in the plume even above the riser orifice.

Figure 4.7b shows the contour of vertical velocity at the approximate out-surface of the plume, which is viewed at the same perspective as measured by HDIV (full name) in (FRTG, 2011) (see Figure 4.7c). As can be noticed in Figure 4.7b, the range of velocity from the LES is from -0.4 m/s-1.4 m/s at the out-surface of the plume, which is quite consistent to the range of velocity from HDIV measurement in Figure 4.7c, which confirms that LES is a robust and appropriate numerical approach to regenerate the approximate multiphase (e.g., oil and gas) plume hydrodynamic characteristics during the Deepwater Horizon Blowout.

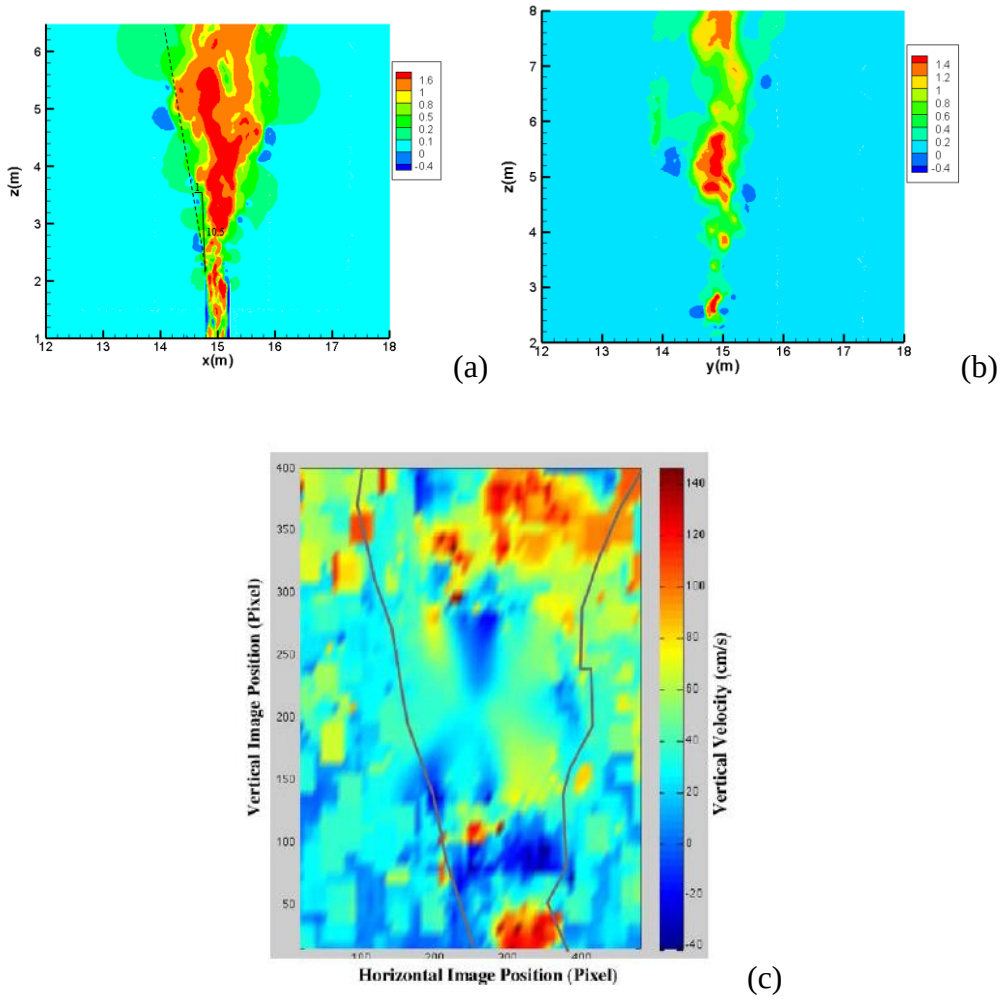

Figure 4.7 Contour of vertical velocity (m/s) (a) at the middle plane in LES (instantaneously) with the orifice located x=15 m, y=14.9 m, z=2 m. (b) at the approximate out surface of the plume (e.g., viewed from the dashed line in Figure 4.7a with an angle of 1:10.5. The view plane is perpendicular to the paper through the dashed line in Figure 4.7a) in LES (c) at the out surface by HDIV measurements in (FRTG, 2011).

Vertical cuts through the modeled pipe and plume shown in Figure 4.8 further elucidate the unsteadiness of churn flow hydrodynamics. Figure 4.8a,b, and c show the contour of vertical velocity at z=1.0-1.95 m (where the orifice is located at z=2.0 m) inside the riser. Negative velocity is noticed near the wall, which is typical flow characteristics of tumbling churn flow of infinite unsteadiness(Laborde-Boutet et al., 2009; Montoya et al., 2016; Parsi et al., 2015). Moreover, the core of the flow (indicated by red) is unsymmetrical

within the riser while the contour levels are more of symmetrical circular shape outside of the riser orifice (above z=2.0 m) than inside the riser orifice. That is because the gas and oil phases intermix with the surrounding water and the violent interaction behaviors of the churn flow are alleviated by the mixing and entrainment of the surrounding water such that the cross section of the plume is more and more circular in shape as the plume goes up.

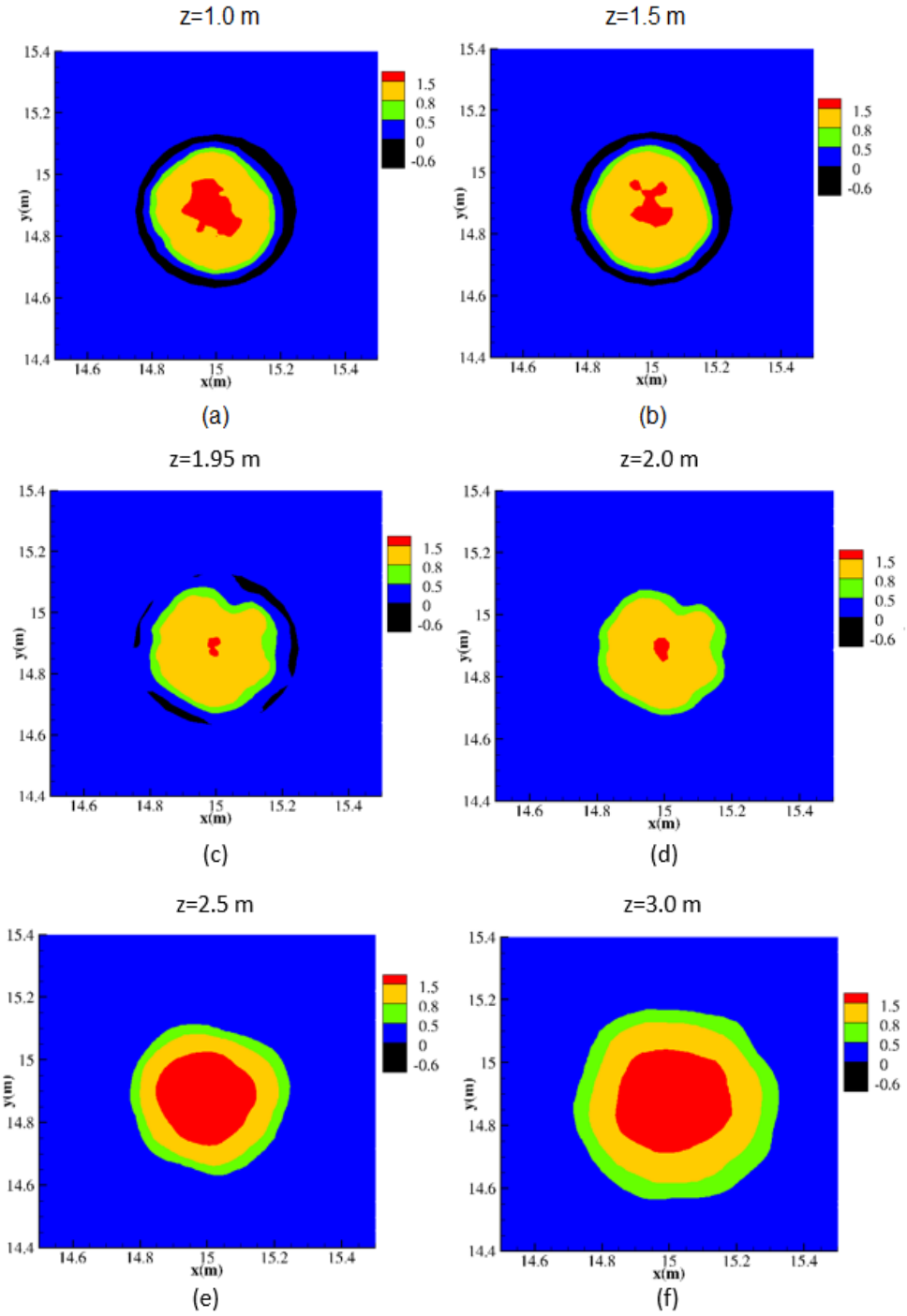

Figure 4.8 Contours of the axial average velocity (i.e., z velocity) of churn flow at cross sections of various elevations from the bottom of the domain (a) z=1.0 m(b) z=1.5 m (c) z=1.95 m (d)z=2.0 m (i.e., the orifice) (e) z=2.5 m (f) z=3.0 m. Within the pipe (z< 2.0 m), the axial velocity varied from +1.5 m/s near the center to -0.6 m/s near the walls. As the fluids (oil + gas) approached the exit of the riser (z=1.95 m), they were entrained by the surrounding water, and the magnitude of the negative velocity decreased from 0.6 m/s to 0.1 m/s. For z=2.5 m and 3.0 m, the maximum of the average axial velocity occupied a relatively broad region at the center axis.

Figure 4.9 shows the oil/gas holdups and velocity vectors at different vertical cuts at t=20.2 s for the churn and bubbly flows, which illustrates the concentrated nature of velocity vectors for churn flow. The vectors of bubbly flow were more or less uniform. Also, note the downwelling velocity for churn flow within the pipe near the wall (y=15.10 m). The velocity vectors of churn flow appear to concentrate (at a given instant) more in space than those of the bubbly flow, which appears to be more or less uniform in space This could be due to the higher buoyancy of the churn flow plume, as it contains more gas. Also, note the downwelling velocity for churn flow within the pipe near the wall (y=15.10 m). One could discern visually that the oil holdup from churn flow decreases much faster with distance than that of the bubbly flow. Also, the oil holdup for both churn and bubbly flow decreased going away from the center plane, but the oil holdup for churn flow seems to be more concentrated near the center of the plume in comparison to that of bubbly flow; this could be deduced by the rapid decrease of oil holdup going from the center plane to the edge of the plume (e.g., 15.05 m and 15.10 m).

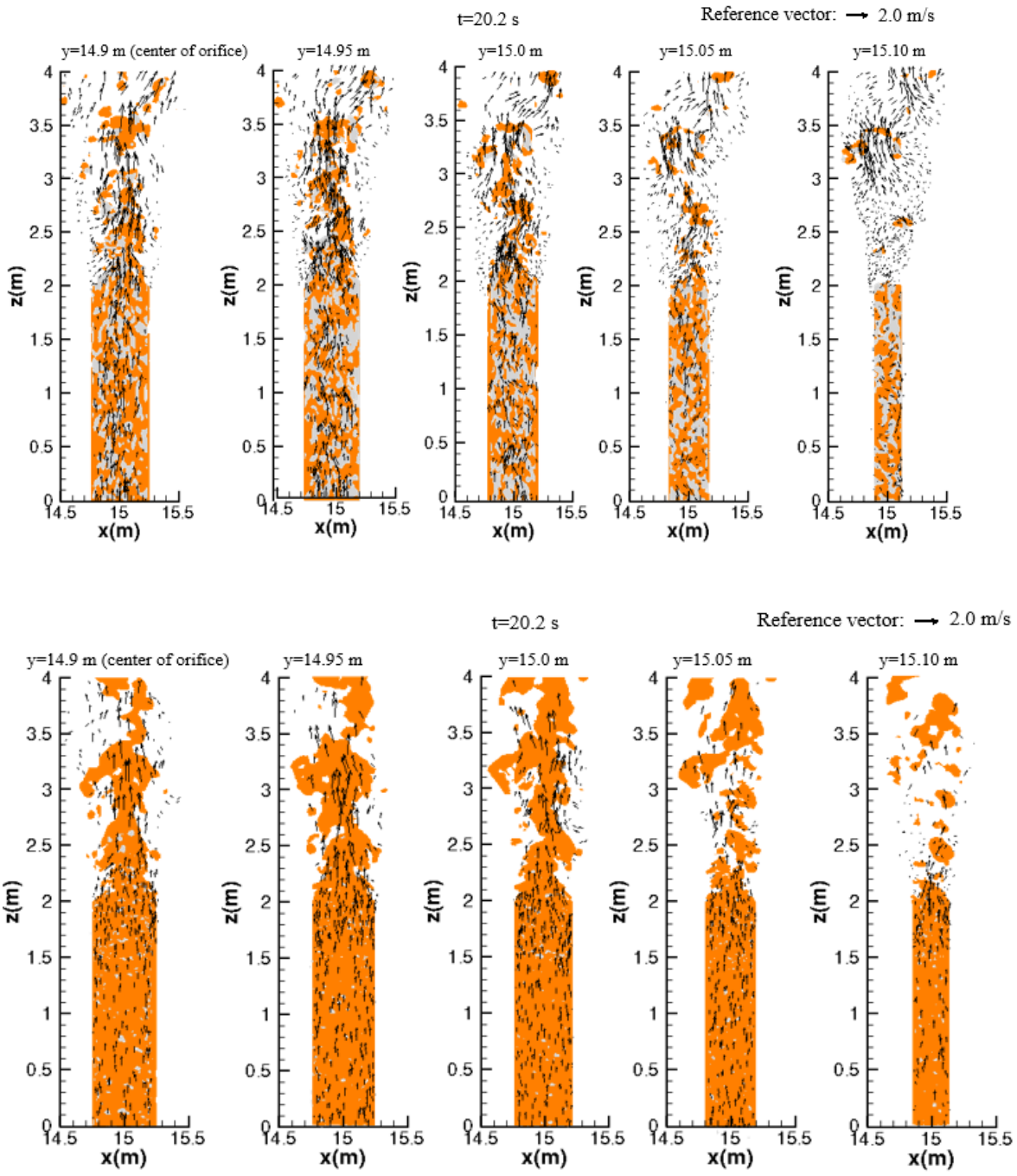

Figure 4.9 Vertical cuts at t=20.2 s through the pipe and the plume of churn flow (upper panels) and bubbly flow (lower panels). The plane at y=14.9 m passes through the diameter and the vertical cut planes were every 5 cm from the center plane for 20 cm (The internal radius of the pipe was taken as 25 cm).

Figure 4.10 shows the oil/gas holdups and velocity vectors at two cross sections, z=1.0 m, and 3.0 m, for the churn and bubbly flows, respectively. As can be noticed in Figure 4.10, major vortices can be noticed at the cross-section of the churn flow with the maximum velocity magnitude of around 0.2 m/s (see Figure 4.10a) while the velocity of the bubbly one does not show any noticeable vortices. This is expected as the interaction of the gas and the oil produce axial velocity due to the flow tumbling while the bubbly flow mainly goes vertically along the riser, similarly as single phase pipe flow.

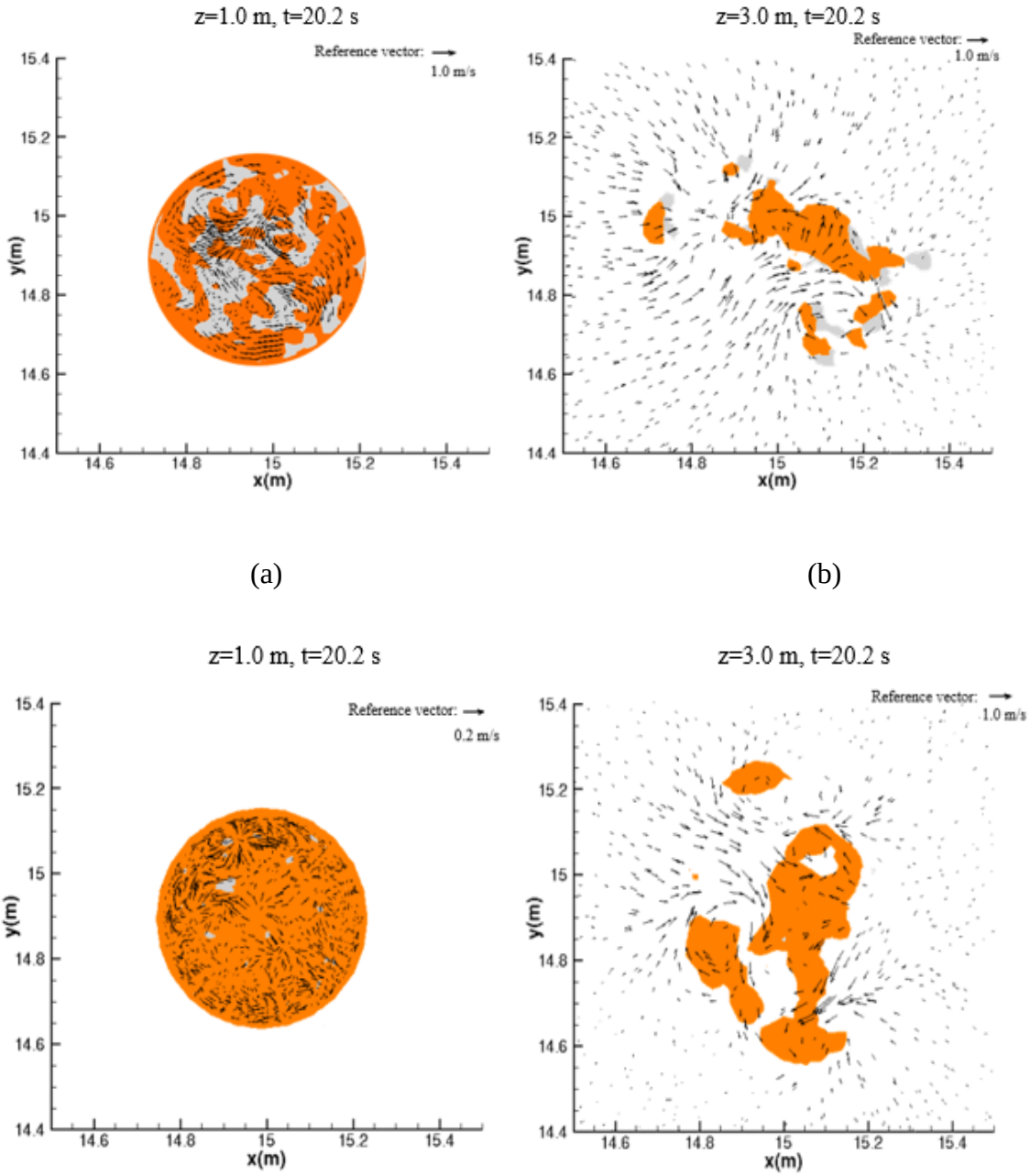

Figure 4.10 Oil holdup (orange) and gas holdup (grey) at two cross sections z=1.0 m (1.0 m below the orifice) and Z=3.0 m (1.0 m above the orifice) along with velocity vectors. (a) and (b) are for churn flow and (c) and (d) are for bubbly flow.

Figures 4.11 and 12 shows the comparison of the absolute and normalized oil/gas holdups (e.g., the local oil/gas holdups scaled by the oil/gas holdup at the centerline, such that the normalized oil/gas holdups start from 1.0 at the centerline and decrease in the radial direction) respectively. It can be noticed from Figure 4.11 that the the oil/gas holdups for both the churn and bubbly flows decreased along the radial direction. The oil/gas holdups of the churn flow decreased at a slower rate along the radial direction compared to the bubbly flow. Of particular interest is the large gas holdup at the plume's edge (pipe radius, r, r=0.5 m) for the churn flow, which would have dispersant application implications.

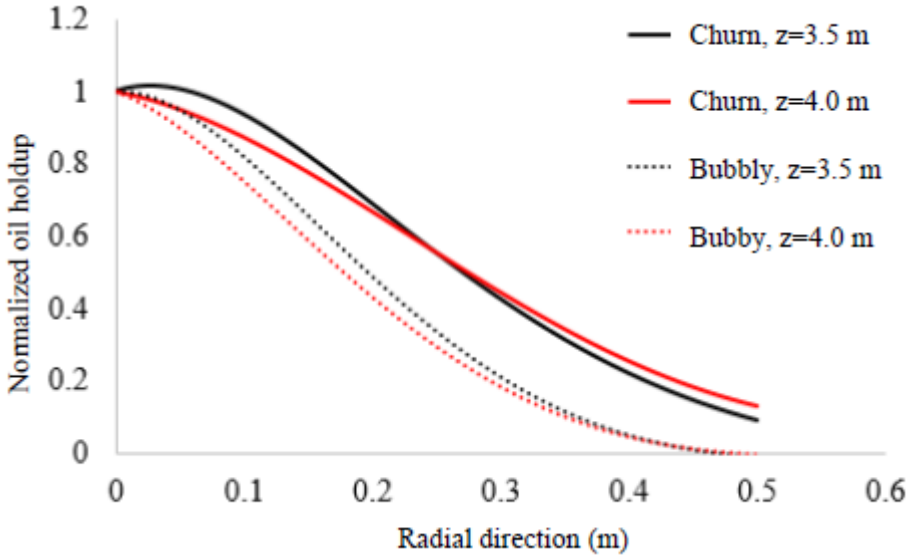

(a)

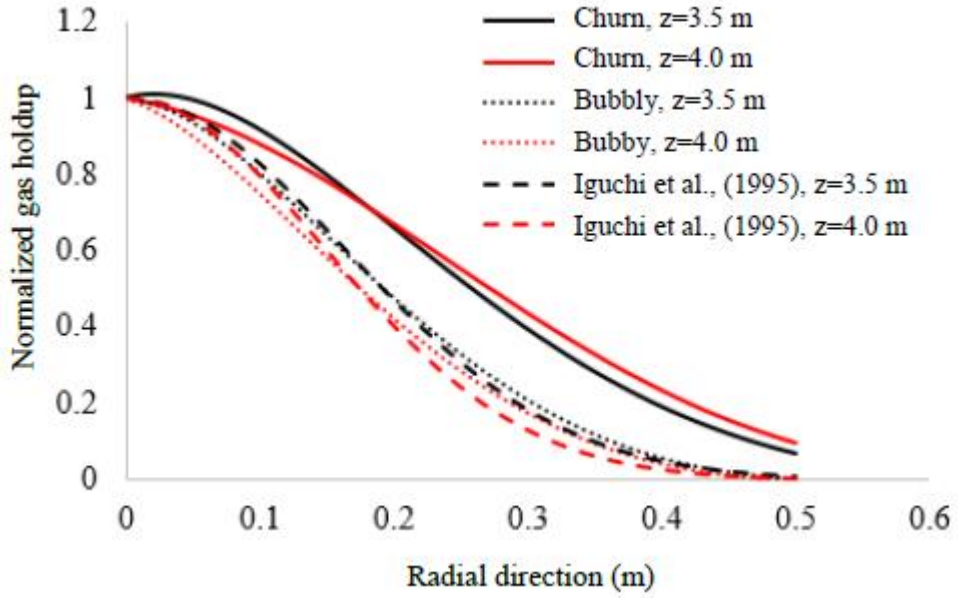

(b)

Figure 4.11 Behavior of oil and gas in the blowout (i.e, outside of the DWH riser) at two elevations, z, above the orifice (located at z=2.0 m). The normalized holdup of (a) oil and (b) gas for the churn and bubbly flows based on the LES approach. The decrease as a function of the radius is slower for churn flow. Also shown is the experimental bubbly flow data from Iguchi et al. (1995), with the good model agreement.

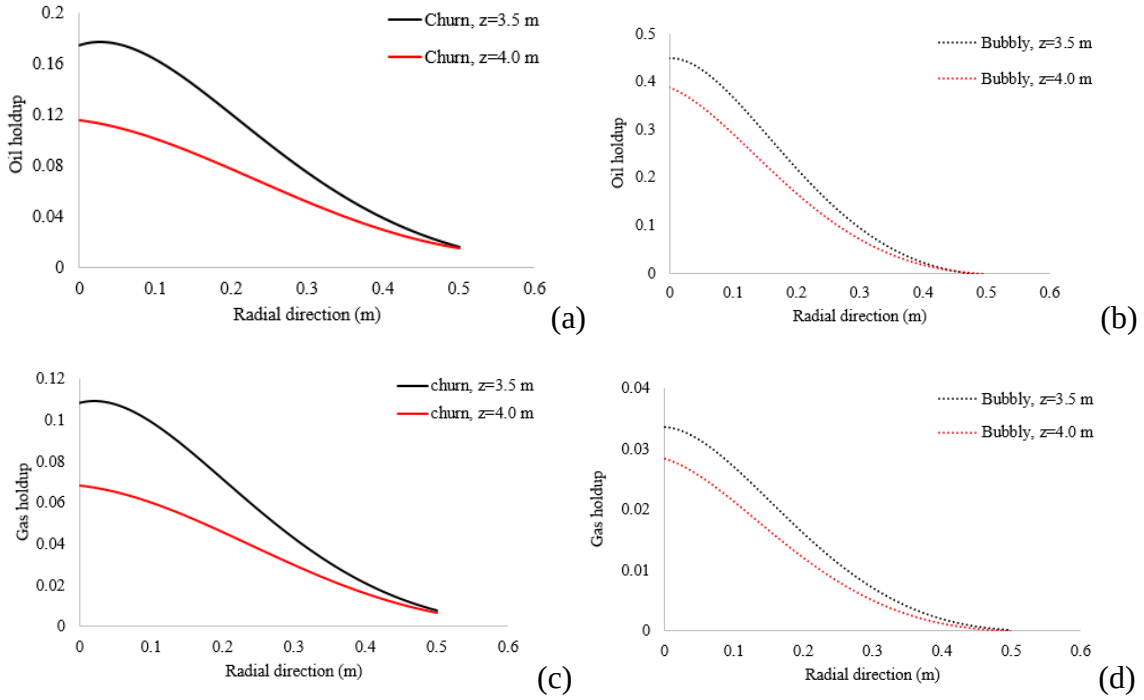

Figure 4.12 Oil and gas holdup for churn and bubbly flow at z=3.5 m and z=4.0 m (1.5 m and 2.0 m above the orifice, respectively). Note that the gas holdup was 0.45 and 0.05 at the orifice of the churn and bubbly flows, respectively. This shows that the gas holdup of the churn flow decreased much rapidly along the center axis (r=0) than for bubbly.

Figure 4.13 shows the normalized oil holdup (e.g., the volume fraction of oil) along the centerline of the plume outside the riser orifice. As the oil holdups at the riser orifice for the bubbly and the churn flows are different, thus the oil holdups along the plume centerline, ϕ_c, are scaled by the oil holdup at the center of the riser orifice, ϕ_o, such that both oil holdups of the bubbly and churn flows start at 1.0 at the riser orifice. As can be noticed in Figure 4.13, the oil holdups of the churn and bubbly flows decrease shapely along the plume centerline. However, the oil holdup of the churn flow decreases more rapidly along the centerline than the bubbly one. This indicates more water be entrained in the plume body due to the presence of the interaction between the gas phase and the surrounding liquid. Figure 4.13 further indicates that the gas phase in the churn flow

intensifies the mixing energy within the plume body such that more water is entrained in the plume, this is most likely to happen within a few diameters above the orifice along the centerline, as the normalized oil holdup of the churn flow significantly decreases before reaching z=3 m in the vertical direction while that of the bubby flow slowly decreases within z=2.5 m.

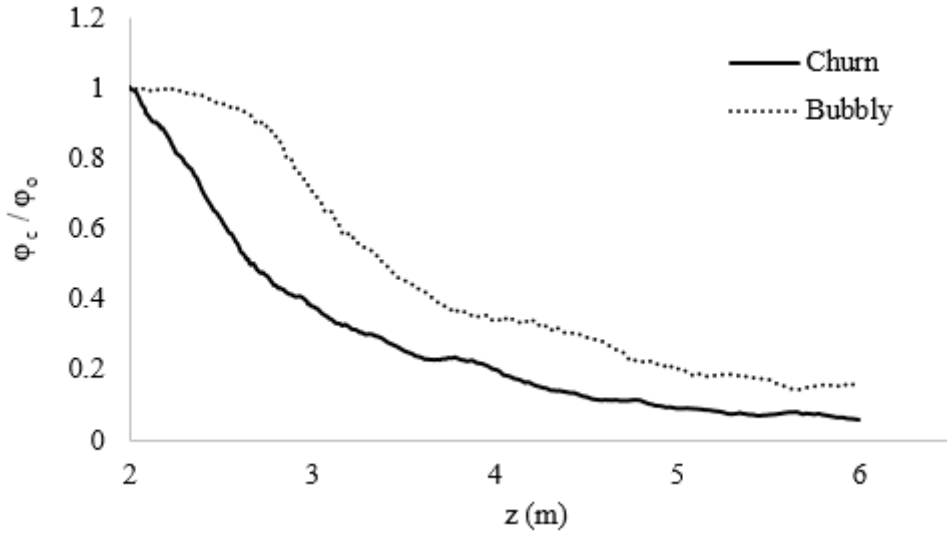

Figure 4.13 Oil holdup along the centerline, φ_c, normalized by its orifice value, φ_o, as a function of elevation for both churn and bubbly flows. As the rate of gas released in each case does not change over time, a rapid decrease of normalized oil holdup could only be due to a larger entrainment of water. Thus, the churn flow plume entrains more water into it than the bubbly flow plume.

As the bubby and churn flows were at different gas flow rates, the normalized turbulence dissipation rate (Fischer et al., 1979; Houghtalen et al., 2016) is used in order compare the turbulence characteristics of the bubbly and churn flows. As can be noticed in Figure 4.14, the normalized turbulence dissipation rate for the bubbly and churn flows are dramatically different. The normalized turbulence dissipation rate of the churn flow (denoted by the solid black line) fluctuates with a wider range compared to the one of the

bubbly flow at z=1 m (inside the riser). The averaged normalized turbulence dissipation rate for the churn flow is around five times of that of the bubbly flow, which indicates that the churn flow has more turbulence energy compared to the bubbly one when inside the riser. The large turbulent energy loss is due to the violent interaction between the phases. At z=3 m, that is two diameters above the riser orifice, the averaged normalized turbulence dissipation rate is doubled for the churn flow compared to the bubbly one.

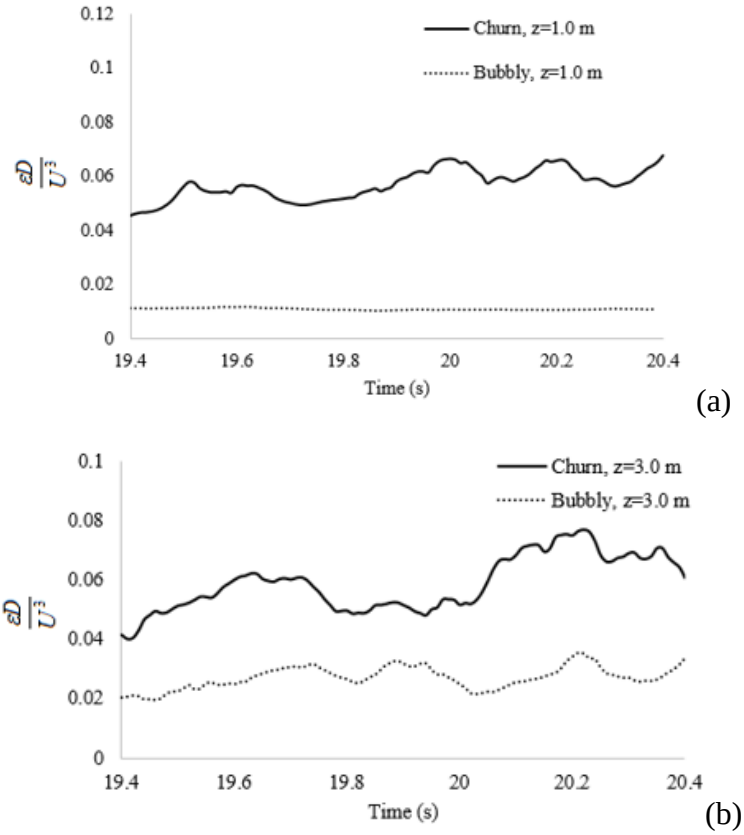

Figure 4.14 Variation of the total energy dissipation rate ε normalized by the pipe diameter D and the velocity U at the cross section (a4.) z=1.0 m (i.e., within the riser) (b) z=3.0 m (i.e., outside the riser). For z=1.0 m (i.e, 1.0 m below the orifice), the cross section is that of the DWH pipe (i.e., riser). At z=3.0 m (i.e., 1.0 m above the orifice), the cross section was circular bounded by an angle of 1:10.5 from the orifice. The normalized total energy dissipation values of churn flow were approximately 5 times and 2.5 times larger than those of bubbly flow at z=1.0 m and 3.0 m, respectively.

Figure 4.15 shows the turbulence intensity ($\frac{u'}{U_c}$) along the radial direction for the bubbly and churn flows at z=2.5 m. It can be noticed that the turbulent intensity of both the bubbly and churn flows gradually increase originating from the centerline in the radial direction, the peak of turbulence intensity appeared at around r in radial distance for both the bubbly and churn flows and then gradually went down in the radial direction after reaching the peak. The turbulence intensity of the bubbly flow agrees well with the experimental data for miscible plumes in the literature (Iqbal and Thomas, 2007; Rahai and Wong, 2002; Shim et al., 2013), especially the results of (Poole and Hall, 2014). However, the turbulence intensity of the churn flow is comparatively higher than that of the bubbly flow. For example, the peak of the turbulence intensity of the bubbly flow is around 0.18 while that of the churn flow is around 0.28, which is an increase of 55.5%. It can be concluded from Figure 4.15 that the churn flow has much larger turbulence energy compared with the bubby flow, which is mainly due to the presence of the gas phase, which violently interacts with the surrounding liquid phase.

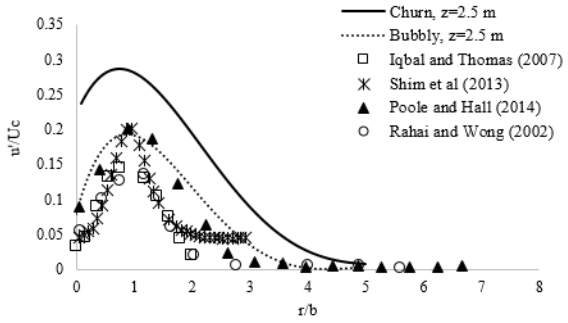

Figure 4.15 Comparison of streamwise turbulence intensity (u'/U_c) between the bubbly and churn flow. The term "u′" is the root mean square streamwise (z direction) velocity fluctuations and U_c is the mean streamwise velocity at the centerline. The parameter "r" is the distance from the centerline in the radial direction and "b" is the half radius (the distance from the centerline to the location in the radial direction where the velocity is half of that at the centerline).

Figure 4.16 shows the normalized velocity along the radial direction at z=3.5 m and 4.0 m, respectively. The velocity profile of miscible plumes can be approximated by Guassian distribution:

$$\frac{w(r,z)}{w(0,z)} = \exp\left[-\frac{a^2 r^2}{(z-2)^2}\right] \tag{4.18}$$

where w(r,z) is the mean streamwise velocity in the radial direction, w(0,z) is the streamwise velocity at the centerline, r is the radial distance, z is the vertical distance from the rise inlet. a^2 is a fitting value.

In Figure 4.16, the mean streamwise velocity was obtained by averaging the instantaneous streamwise velocity over 4.0 s in the simulation. It can be noticed that the churn flow exhibits a slower rate of decrease of the mean streamwise velocity in the radial direction, which might because the presence of the gas blobs with larger buoyancy slowed down the momentum decrease as the gas interacts with the surrounding water.

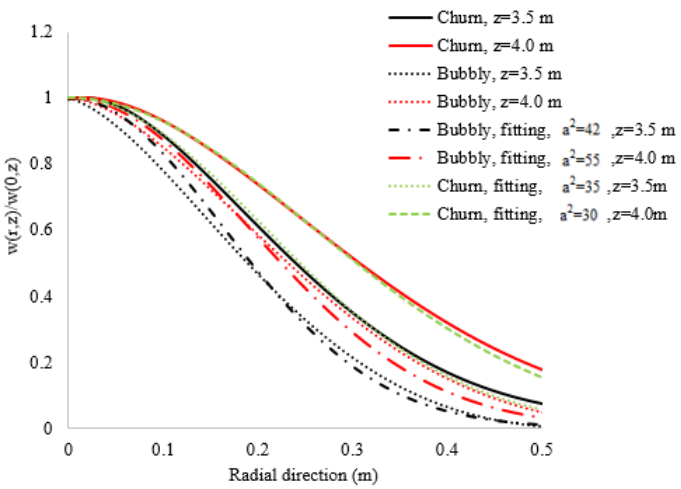

Figure 4.16 Mean axial velocity W(r,z) normalized by the value at the center along the radial direction at various downstream distances (the orifice is at z=2.0 m). Also shown are the fit of the Gaussian profile based on the equation $W(r,z)/W(0,z) = \exp[-a^2 r^2/(z-2)^2]$. The value a^2=42~55 for bubbly and around 30~35 for churn flow. The bubbly and churn flow profiles were obtained by averaging the numerical results over 4.0 seconds from 19.0 s to 23.0 s.

It is important to evaluate the entrainment coefficient in order to estimate the oil discharge rate. The estimation of oil discharge from the riser was evaluated by using a presumably known entrainment coefficient, for example, Reddy et al. (2012) used an entrainment coefficient of 0.05 for the oil plume after the riser cut on June 3rd, 2010, which is a value that commonly used for the miscible plume. However, the present research shows that the presence of the churn flow may significantly affect the hydrodynamics of the plume in various aspects, such that the entrainment coefficient of the churn flow might be different than what was previously assumed.

The entrainment coefficient calculation in the present study is based on (Reddy et al., 2012) as follows. The radius of the plume cross section (R) is calculated by assuming a constant half-spread angle of the jet at 1:10.5:

$$R = 0.25 + \frac{1}{10.5} * (z - 2) \tag{4.19}$$

The riser is 0.25 m in radius and located at z=2 m and thus (z-2) is the distance from the orifice to the given cross section in the vertical direction.

The entrainment coefficient (α) appears in the entrainment equation as follows:

$$Q_{water} = \alpha W_{avg} S \tag{4.20}$$

where Q_{water} is water entrainment (m^3 / s) and W_{avg} is the averaged vertical velocity in the yellow conical frustum part and S is the lateral surface area of the yellow conical frustum part in Figure 4.17.

Q_{water} is calculated as:

$$Q_{water} = A_2 W_2 H_{dw(2)} - A_1 W_1 H_{dw(1)} \tag{4.21}$$

where A_1 and A_2 are the cross section area of the plume at 3.1 m and 3.0 m above the riser orifice, respectively. W_2 and W_1 are the averaged vertical plume velocity within the cross sections at 3.1 m and 3.0 m above the riser orifice, respectively. $H_{dw(2)}$ and $H_{dw(1)}$ are the averaged water volume fraction at 3.1 m and 3.0 m above the riser orifice, respectively. Thus, $A_2 W_2 H_{dw(2)}$ is the water flow rate at 3.1 m above the orifice and $A_1 W_1 H_{dw(1)}$ is the water flow rate at 3.0 m above the orifice.

The lateral surface area S in Equation 4.22 was calculated based on the equation:

$$S = \pi R_2^2 \sqrt{(Z_2 + 2.625)^2 + R_2^2} - \pi R_1^2 \sqrt{(Z_1 + 2.625)^2 + R_1^2} \qquad (4.22)$$

where Z_2 =5.1 m and Z_1 =5.0 m. R_2 and R_1 are the radii of the cross sections at 3.1 m and 3.0 m above the orifice, obtained from Equation 4.19.

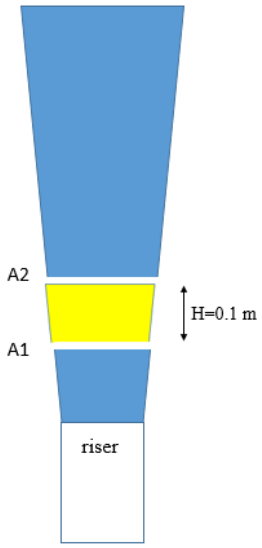

Figure 4.17 Schematic view of the calculation of the entrainment coefficient. The yellow conical frustum part is a cut portion of the plume, which is from 3.0 m to 3.1 m above the orifice of the riser. The height of the yellow conical frustum part (H) is 0.1 m. As for the yellow conical frustum part, the cross section area at the lower bottom (e.g., the cross section area of the plume at 3.0 m above the orifice) is indicated as A_1 and the cross section area of the upper top (e.g., the cross section area of the plume at 3.1 m above the orifice) is indicated as A_2. The lateral surface area of the yellow conical frustum part is indicated as S.

Figure 4.18 shows the entrainment coefficient of the bubbly and churn flow based on the approached introduced above. Figure 4.18a shows the instantaneous and time averaged entrainment coefficient at no time lag (explained in the caption of Figure 4.18).

The time averaged entrainment coefficient of the churn flow is 0.16 while the that of the bubbly flow is 0.12. This indicates that the entrainment coefficient of the churn flow is 33% under no time lag condition. In order to verify the results, we also considered the condition with a time lag to allow the fluid to travel through the controlling volume. As the average flow velocity is around 1.0 m/s, the lag time is taken 0.1 s and 0.2 s for the churn and bubbly flow cases, respectively, as the average flow velocity is 1 m/s and 0.5 m/s for the churn and bubbly flow cases, respectively. For the condition of time lag, the time averaged entrainment coefficient for the churn and bubbly flow are 0.15 and 0.11, respectively. This indicates that the churn flow increases the entrainment coefficient by 36%.

In all, the churn flow increases the entrainment coefficient by around 33-36% by the presence of large volumes of gas phase interacting with the surrounding liquid phase fluids.

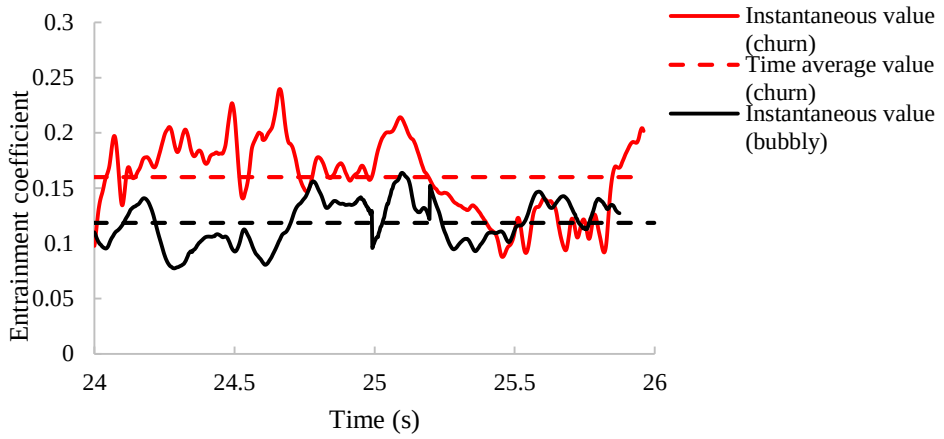

(a)

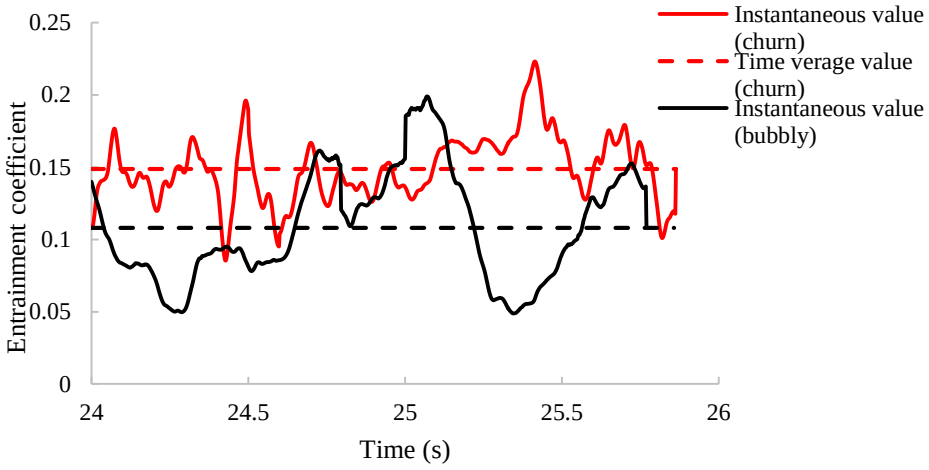

(b)

Figure 4.18 Instantaneous entrainment coefficient for churn flow and bubbly flow (a) by taking Equation (4.21) at the same time level with no time lag. The dashed red line indicates the averaged value is 0.16 and the dashed black line indicates the averaged value is 0.12. (b) by using Equation (4.21) with a time lag of 0.1 s and 0.2 s for the churn flow and bubbly flow, respectively. The dashed red line indicates the value is 0.15 and the dashed black line indicates the value is 0.11. For the churn flow, the first term on the right hand side of Equation (4.21) was evaluated at (t+0.1) and the second term was evaluated at t. The time interval was chosen at 0.1 s to allow for the fluids A_1 to travel to A_2 approximately for the churn flow (as the averaged velocity is around 1.0 m/s). For the bubbly jet, the first term on the right hand side of Equation (4.21) was evaluated as (t+0.2) and the second term was evaluated at t. The time interval was chosen at 0.2 s to allow for the fluids A_1 to travel to A_2 approximately for the bubbly jet (as the averaged velocity was around 0.5 m/s).

4.4 Conclusions

This is the first investigation of a blowout from a multiphase churn flow (oil and gas in water), and there were no data in the literature for comparison. The sole exception is Iguchi et al. (1995) who reported only limited data of jets of churn flow of air and water in water. The LES simulation bubbly flow results agreed closely with literature data for various properties of the plume. This indicates that the LES robustly and accurately characterizes the general plume dynamics for both bubbly flows and as applied for churn flow.

Various groups estimated the oil discharge from the MC252 well, including the U.S. Government formed the Flow Rate Technical Group (FTRG), which included five Department of Energy labs and various academicians(McNutt et al., 2012). With the exception of Dr. Leifer of the FTRG, all assumed bubbly flow. Dr. Leifer considered intermittent behavior in the fallen (horizontal) riser prior to June 3rd, 2010 and reported "slug" flow behavior with a period of tens of seconds. However, the video of the release after the riser was cut on June 3rd, 2010 (Video, SI) suggests a behavior closer to churn. In essence, where slug flow exhibits a short period, it becomes churn (Montoya et al., 2013).

Based on energy loss considerations, neglecting the churn flow behavior could underestimate the energy loss in the pipe by five folds (Figure S7), which would overestimate the oil discharge by more than 200% (actually $\sqrt{5}$).

Using fluid measurements outside of the DWH pipe, researchers (page 164 of PlumeCalculationTeam, 2010), estimated the discharge from the DWH based on visual observation of the external eddies within one diameter of the release based on a single phase (or bubbly) velocity profile (Wygnanski and Fiedler, 1969). In their approach, the speed of eddies on the outer edge of the plume was assumed to be 1/1.6 to 1/2.5 the plume's

centerline speed. The deviation from the single phase (or bubbly) profile, as noted herein, would introduce uncertainty in that approach; on the one hand, the actual speed of the outer eddies could be larger, consistent with the large velocity values of churn flow at, for example, r=0.5 m; z=4.0 m, in comparison with the common Gaussian profile. This would result in a smaller estimated oil flow rate. On the other hand, the zone of high velocity near the center for churn flow is broad, resulting in a larger oil flow rate if the ratio of eddy speed to centerline speed is consistent with the assumption of the Plume Calculation Team (2010). Another group (Camilli et al., 2012a) estimated oil discharge using Acoustic Doppler Current Profiler (ADCP) velocimetry, which provided the total fluid velocity, although no corrections were reported for erroneous velocities–a common feature in ADCP data of mixed phase flows (Leifer et al., 2015; Nauw et al., 2015). To account for water in the discharge flow, Camilli et al. (2012a) used an entrainment coefficient of 0.056, three times smaller than for churn flow and even smaller than the one for bubbly flow. Smaller entrainment coefficients would induce an overestimate in the oil discharge.

Numerous papers on the oil droplet size distribution and gas bubble size distribution have been published, e.g., Gros et al. (2017); Zhao et al. (2017b) and publications therein, yet they all ignored churn flow dynamics. Based on the findings herein, the droplets formed by a churn flow plume are likely to be smaller than those formed by oil only or bubbly flow plumes (all parameters being equal), because the formation of oil droplets occur through a two breakup mechanisms: First, shear and interfacial instability on the outer surface of the jet produce ligaments in a process known as primary breakup (Gorokhovski and Herrmann, 2008). Second, these ligaments are entrained into the jet and subsequently break into droplets based both on the mixing energy (energy dissipation rate, ε) and the oil within the

plume. This is known as secondary breakup (Zhao et al., 2016b). A large ε value alone cannot produce small droplets without the presence of water or gas to surround them, and thus, the holdup plays an important role in droplet formation within the first few diameters of the orifice. We saw also that churn flow spreads the gas across the plume, and thus concentrates the oil in the center in comparison with the bubbly flow, which concentrates the gas (but not the liquid) in the plume center (Lima Neto et al., 2008; Milgram, 1983). Thus, churn flow is more likely to produce smaller oil droplets due to the contribution of individual bubbles to the local turbulence energy (Fabregat Tomàs et al., 2016; Zhao et al., 2016b). If the dispersant is applied on the plume edge, the presence of higher gas holdup would scavenge dispersant, decreasing effectiveness.

Although the calculation was for a smooth pipe, non-uniformity including protrusions in the DWH pipe were documented, and are likely to exist in future blowouts. Protrusions could be in the shape of fragments of metal from the pipe and other infrastructure and spikes that would disrupt large-scale eddies minimizing, therefore, churn flow behavior, or they could be bulky such as fragments of the drill, blocking portions of the pipe, magnifying churn flow by increasing the superficial velocities of both gas and oil. In the latter case, it shows that the flow would remain "churn" if the new area remains larger than 10% of the smooth pipe area. Additionally, gashes in the pipe below the seabed were likely with some of the blowout flowing outside the riser for some of its path. Depending on the details, this could make churn flow more or less likely. Given the significant implications of whether the flow is churn or bubbly it is critical to consider in any efforts to assess future blowouts to evaluate both types of flow, and ideally to collect data to confirm one or the other.

In the assessment of future deep sea oil and gas spills, correctly assessing the character of the flow in the pipe is critical to providing more reliable estimates for the response. Churn/slug flow has been well studied in conduits, and this study highlights the needs to incorporate that knowledge in analyzing geophysical multiphase flows. Still, additional complexity must be considered in future studies to reflect the complexity of reality, including pipe shape, hydrates, condensates, produced water, and the many additives used in production activities. Furthermore, such studies can identify key measurements needed to confirm flow character, decreasing uncertainty. Although the precise details of the conditions of the interior of the pipe are unlikely to be known for a blowout, studies to characterize the flow for a range of conditions would provide more robust uncertainty on estimated flow rates. Any response decisions must address both the best estimated flow rate plus one or two sigma deviation due to uncertainty to ensure success.

CHAPTER 5

EXPERIMENTAL AND NUMERICAL ANALYSIS OF THE HYDRODYNAMICS OF THE MULTIPHASE FLOW IN A LABORATORY SCALE

5.1 Introduction

In this chapter, a laboratory scale experimental setup was built for releasing multiphase jet/plume to evaluate the influence of the gas phase on the jet/plume hydrodynamics, especially at the near-to-orifice region. A numerical approach that introduced in Chapter 4 was used to demonstrate the possibility of churn flow inside the riser as well as at the near-to-orifice region. Hence, this chapter provides an alternative experimental method to study and compare the hydrodynamics of the bubbly and churn flow in a laboratory scale in order to provide a new perspective on the detailed flow behavior in the Deepwater Horizon Blowout. Due to the experimental limitation and safety concerns, air and water instead of crude oil and methane were used for the presented experiment. High resolution videos are recorded to capture the detailed flow dynamics of various flow regimes for both inside the riser and at the near-to orifice region (e.g., 10 cm above the orifice of a releasing diameter of 2.5 cm). Particle Imaging Velocimetry (PIV) is used to measure the flow velocities and obtain the energy spectrum during the air/water release.

Subsurface multiphase (gas-liquid) jet and plume flow play an important role in many engineering applications and industrial processes, including chemical reactors (Jiang et al., 2005), steam generators(Zare et al., 2018), and Carbon Capture Storage(Nguyen et al., 2016). Aside from the aforementioned applications, gas-liquid jet and plume encountered in the natural system, such as the Deepwater Horizon Oil Spill, have caught the attention of researchers for its impact on the natural environment and ecosystem.

Several flow regimes, bubbly, churn, and annular, can be classified depending on the pipe geometry, flow property, volume fraction and velocity of each phase. The bubbly flow, which occurs when the velocity of the gas and liquid phases is low, have discrete bubbles dispersed and suspended in the continuum phase (liquid phase). When the velocity of the liquid and gas phases increase, churn flow occurs with the gas and liquid phases highly distorted and oscillating up and down. There are a number of studies focusing on the bubbly flows in open literature: Iguchi et al. (1997) researched the air-water bubbly jet by using Laser Doppler Velocimetry and found the jet radial velocity basically follows the Gaussian profile. The presence of bubbles significantly increases turbulence production while having a slight influence on the mean velocity of the bubbly jet when the gas volume fraction is small. Rensen et al. (2005) further concluded that the presence of bubbles in jet/plume increase turbulence energy on the small scales than on large scales and leads to a less steep slope than the classical Kolmogorov -3/5 law for the spectrum analysis. With the increasing gas volume fraction in bubbly flow, bubble slips velocity increases while the bubble drag coefficient decreases (Ruzicka, 2000). However, the mean liquid velocity significantly increases as the gas volume fraction increases (Lima Neto et al., 2008). Leitch and Baines (1989) concluded that individual bubble wakes can contribute to the entrainment into the liquid jet on a significant scale. As for the churn flow, most of the research is focused on the flow inside the vertical/horizontal pipes (Montoya et al., 2016) and few research studies the churn jet flow. Deshpande et al. (2012) studied the air entrainment of churn flow region of plugging liquid jet in open water and shows that the turbulence energy level is maximized at the churn flow region, presenting a strong periodically motion behavior. Sun et al. (2005) experimentally observed the interfacial

structure of churn flow in bubble column reactor and Yamagiwa et al. (1990) developed correlations of gas holdup and gas entrainment for churn jet experimentally.

The above mentioned research is mostly focused on the flow characteristics in the far field (e.g., distance larger than 20 diameters of the orifice in the downstream) even though the flow near the orifice region may play an important role in the flow development in the downstream. Meanwhile, there is very few research focusing on the churn jet in the open literature to the best of our knowledge and most papers studying churn flow are for conditions within the horizontal/vertical pipe. However, the churn jet (flow injected from the orifice in horizontal /vertical pipe) preserve the typical churn flow characteristics at the near-to-orifice region, which may be different than the bubbly jet in various aspects, such as the velocity and turbulence energy, which calls for the attention from researchers to study on both the experimental and numerical sides. Boufadel et al. (2018) recently suggested that oil flow from the Deepwater Horizon oil blowout can be "churn" rather than the assumed "bubbly", which may provide new perspectives in estimating the total oil flow rate from the DWH. For DHW oil spill, the flow characteristics at the near-to-orifice region can be of importance in the estimation of droplet size distribution as well as the evaluation of dispersant effectiveness. Therefore, there is a need to gain a better understanding of the flow behavior of the bubbly and churn jet, especially in the near-to-orifice region.

In the present study, we experimentally measure the air-water bubbly and churn jet in a laboratory scale by using Particle Imaging Velocimetry (PIV) to evaluate the influence of the gas phase on the jet/plume hydrodynamics, especially at the near-to-orifice region. In parallel, Computational Fluid Dynamics (CFD) approach with Large Eddy Simulation (LES) is used to simulate the hydrodynamics of bubbly and churn jet in detail.

5.2 Methodology

As shown in Figure 5.1, a transparent acrylic water container whose size is 61 cm $\times$61 cm $\times$61 cm was built to contain water released from a crystal clear round pipe. The air and water were injected from a crystal clear round pipe whose inner diameter is 2.5 cm and the outer diameter is 3.175 cm. The water flow rate was controlled by a power supply (12 V) and measured by a digital flow meter (manufactured by Savant Electronics, Inc., model # SKU-DF067) and the air flow rate was controlled and measured by a rotameter (manufactured by Omega Engineering, Inc., Acrylic meter, model # FL-2016). A portion of the crystal clear round pipe (e.g., 10 cm in length) was above the water container bottom, which allowed the flow behavior inside the pipe to be captured by the PIV measurement and high resolution camera recording. The liquid phase was tap water whose density is 998 kg/m^3 and dynamic viscosity is $8.9*10^{-4}$ Pa · s and the gas phase was air whose density is 1.29 kg/m^3 and dynamic viscosity is $1.8*10^{-5}$ Pa · s. The experimental measurement was taken at a constant temperature (room temperature ~15 ℃) and humidity (relative humidity ~40%) environment.

The PIV system that manufactured by Dantec consists of a Dantec Dynamics HiSense PIV/PLIF CCD camera (Model #. C4742-53-12NRB, Dantec Dynamics A/S, Denmark), a double pulsed Nd YAG laser with an output of 800 mJ. The laser sheet generated a thin vertical plane crossing through the center of the orifice.

The camera used Nikon lens with AF Micro-Nikkor 60 nm f/2.8D that produced a high resolution of 1264$\times$1008 pixel per frame. The camera is approximately 20 cm from the edge of the acrylic box, which provided a viewing area of 114 mm$\times$114 mm. The measurement sampling rate is 10 Hz with a total sampling of 200 frames. The recorded

frames were processed by Flow Manager ™ software, provided by Dantec Dynamics. A 32×32 pixel interrogation was used for the purpose of best measurement accuracy and spatial resolution.

Silver-coated particles whose diameter are 10 μ m with a density of 1.4 g/cm^3 are used to seed the measured flow. The seeding particles were well-mixed with water before being injected into the pipe.

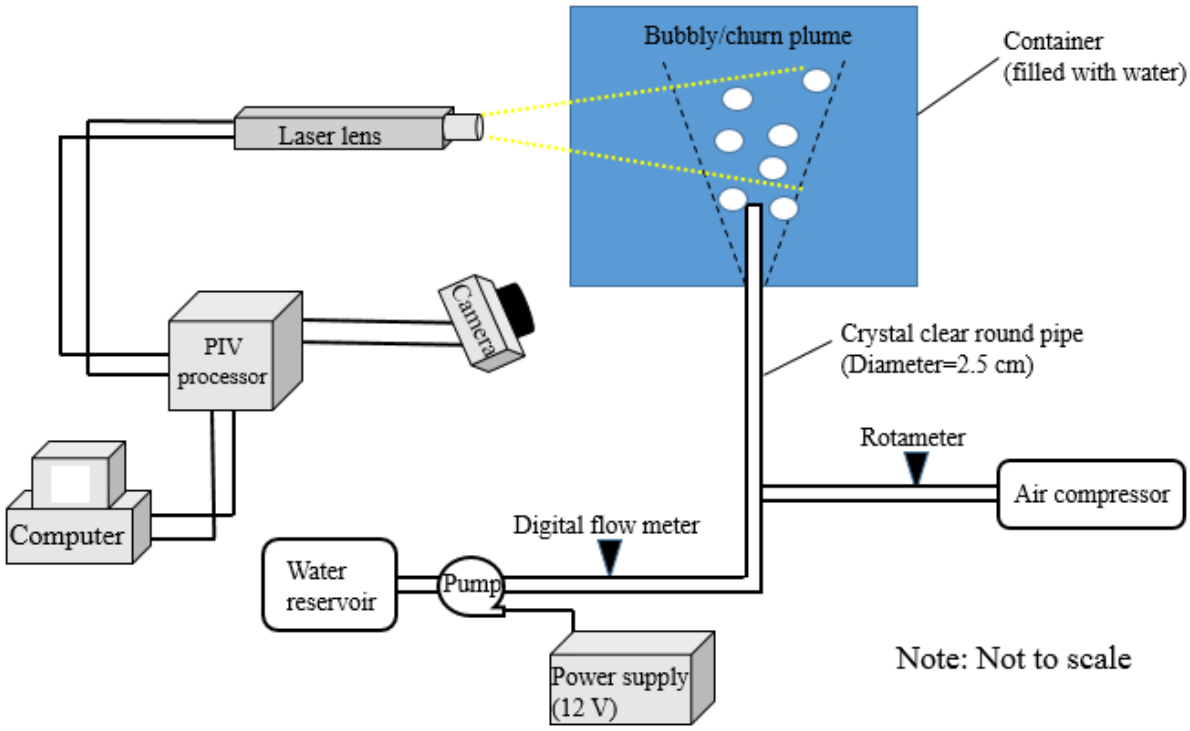

Figure 5.1 Systematic view of the PIV experimental measurement setup.

Meanwhile, high resolution videos were taken to observe the flow behavior inside the vertical round pipe to identify different flow regimes related to the air/water rates. PIV system was operated to measure the flow velocity both inside the pipe (~10 cm in length) and a short distance above the orifice. The 2D velocity flow field was measured by the PIV system for the bubbly and churn flows, respectively. The water flow rate was at ~5.7 LPM

(liter per minute) and the air flow rate was ~ 0.5 LPM, making the air volume fraction for the bubbly flow case of ~8%. As for the churn flow, the water flow rate was maintained at ~5.7 LPM and the air flow rate was kept at ~10 LPM, making the air volume fraction for the churn flow case of ~63.7%.

5.3 Numerical Approach

Computational Fluid Dynamics (CFD) is used as a numerical approach to study the laboratory scale air and water multiphase flow. Commercial CFD software ANSYS-FLUENT with Large Eddy Simulation (LES) model was used to capture the unsteady state eddies and detailed turbulence structures. The volume of Fluid (VOF) model was used to track the air and water phases. The computational domain consists of a 3D cubic water container which is 61 cm $\times$ 61 cm $\times$ 61 cm, that is the actual size of the acrylic box used in the experimental measurement. The pipe is 25 mm in diameter whose length is 50 cm in length. The orifice is 10 cm above the water tank bottom. The length of the pipe in the numerical simulation is 20 times the diameter of the pipe, which is long enough to minimize the effect of the boundary condition at the pipe inlet. A two dimensional schematic view of the computational domain is presented in Figure 5.2. The mesh size is 1 mm at the near-to orifice region and the mesh size gradually increases to 8 cm at the top surface as the elevation increases. The computational domain consists of ~11 million nodes in total. The numerical simulation was run on 48 processes in parallel with a time step of 0.0001 s.

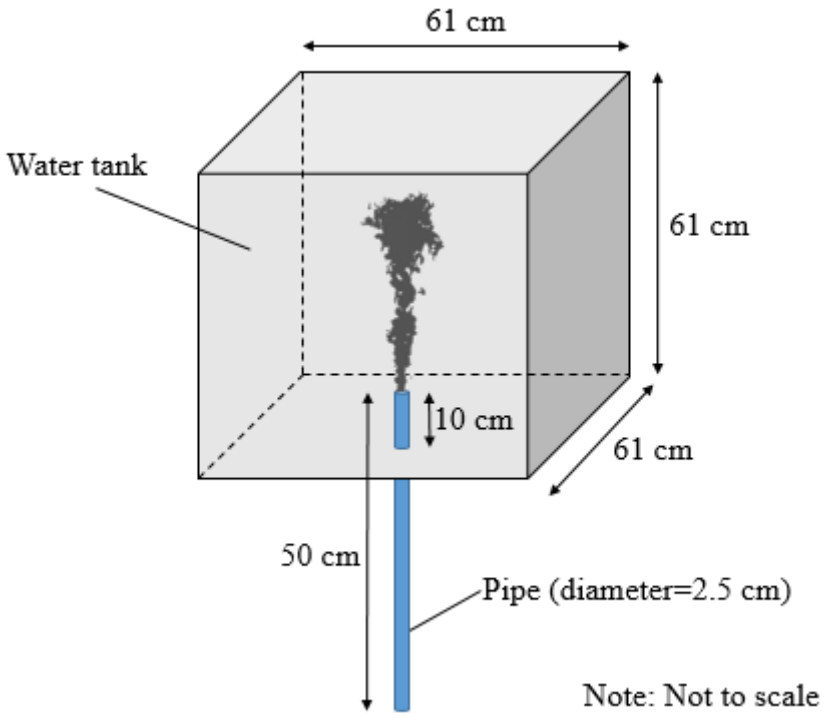

Figure 5.2 Schematic view of the computational domain in the CFD simulation.

5.4 Results and Discussion

Figure 5.3 shows the bubbly flow at the near-to-orifice region. As you can see, the air was formed into discrete small bubbles and those air bubbles barely interacted with one another.

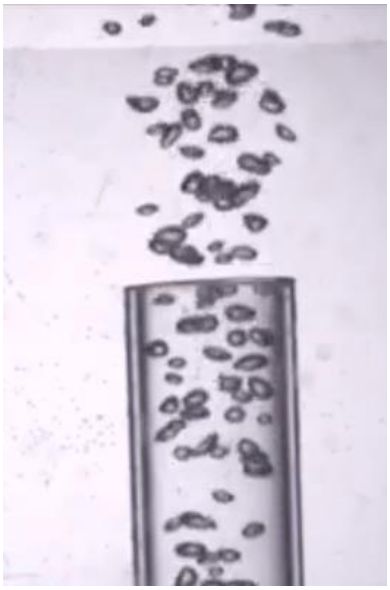

Figure 5.3 Bubbly flow at the near-to-orifice region.

Figure 5.3 shows the churn flow at three consecutive time levels. Unlike the bubbly flow presented in Figure 5.2, churn flow in Figure 5.4 shows infinite unsteadiness and the air and water voilently interacted with each other all the time. For the chrun flow, the water near the pipe wall might go downward, see Figure 5.4a. Air bubbles were entrained in the water and exhibit chaotic flow behavior when interacted with the water. Big air blobs were formed at the orifice and then pinched off and rose up in the vertical direction.

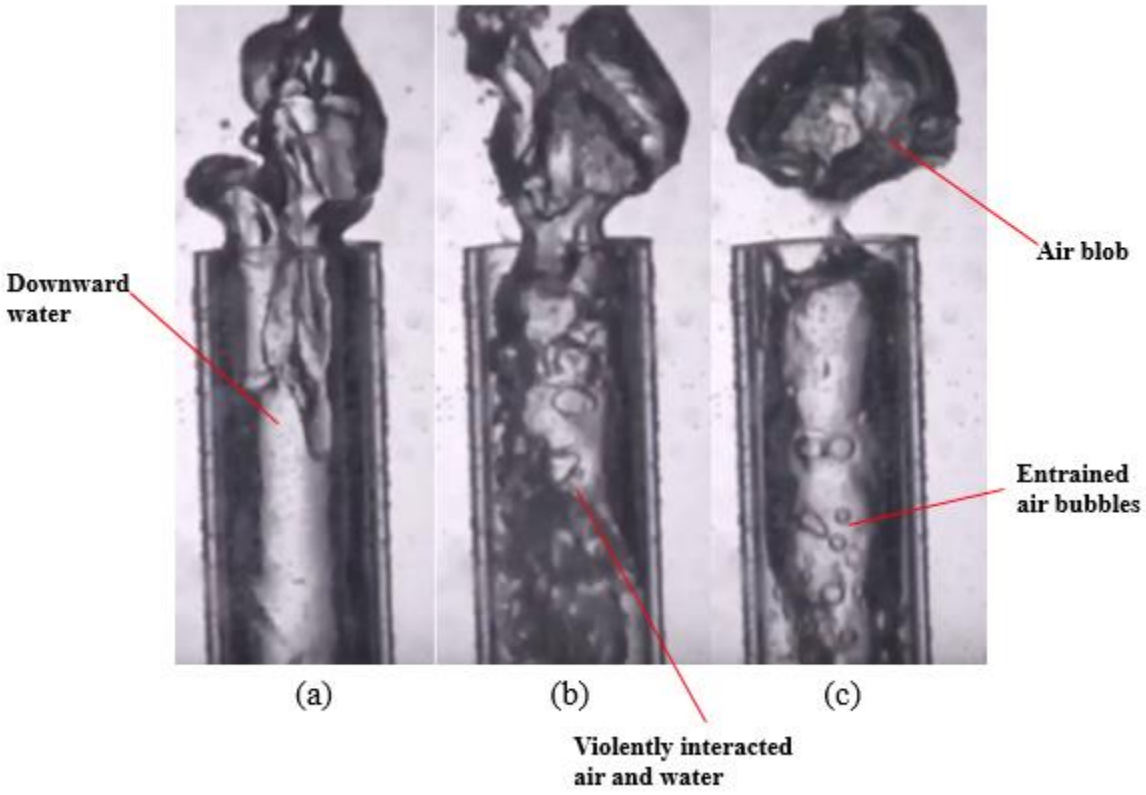

Figure 5.4 Churn flow at the near-to-orifice region for three consecutive time levels.

Figure 5.5 shows the 2D plane captured by the camera of the PIV measurement system. The tiny white dots are the seeding particles and the glares, especially for the churn flow in Figure 5.5b is the result of the reflection by the bubbles. However, the glare by the air bubbles is inevitable with the lighting source presented.

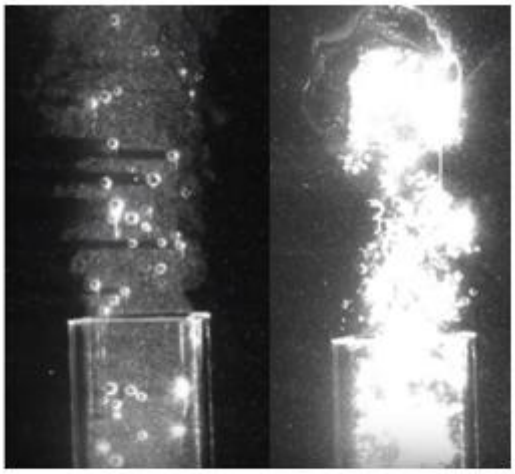

Figure 5.5 View of the 2D cross-sectional area captured by the camera (Nikon lens of AF Micro-Nikkor 60 nm f/2.8D) in the PIV measurement system.

Figure 5.6 shows the time-average of the plume profile taken by the high resolution camera. The sampling rate is 0.02 s and the total time of sampling is 4 s. Thus, Figure 5.6 averages the total 200 frames to obtain the average plume profile at the near-to-orifice region. The half jet angle of the bubbly one is $\tan(\alpha)$=1/5.5, which is slightly smaller than the half jet angle of single jet ($\tan(\alpha)$=1/5, (Pope, 2000)) while that of the churn one is $\tan(\alpha)$=1/4, which suggests that churn flow spreads momentum with a larger angle and the churn flow has a "wider" cross-section at the same elevation from the orifice compared to bubbly flow. With a larger half jet angle, the churn flow flow might entrain more water from the ambient environment than the bubbly flow.

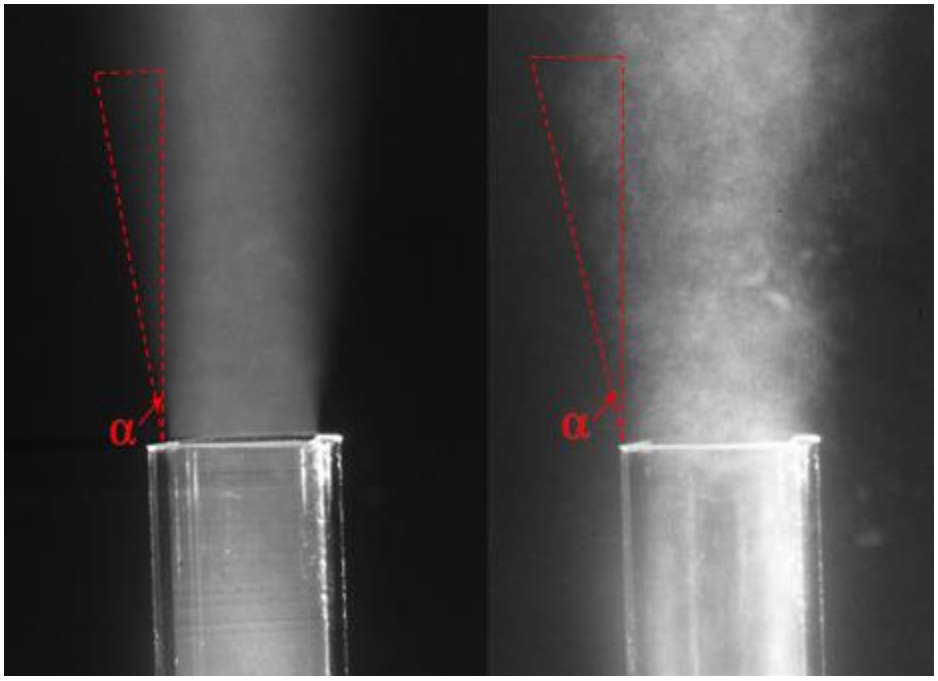

(a) (b)

Figure 5.6 Time average plume profile of the near-to-orifice region, in which α is the half jet angle (a) for the bubbly, left panel (b) for the churn flow, right panel.

In the presented PIV measurement, the sampling rate of measurement is 10 Hz with a total of 200 samplings. The measured flow velocity, $\mathrm{u_i}(x,z)$, by PIV can be obtained as the average velocity, and turbulent velocity, as follows:

$$\mathrm{u_i}(x,z) = \overline{U}(x,z) + \mathrm{u_i'}(x,z), i = 1,2,3...,N \tag{5.1}$$

where i is the index that representing different realizations of the PIV measurement (e.g., "i" is ranged from 1 to 200 in the presented measurement), $\overline{U}(x,z)$ is the average of N realizations of every measurement point (m/s), and $\mathrm{u}'(x,z)$ is the turbulent fluctuation at every measurement point (m/s).

The scaled mean velocity profiles of the bubbly and churn flow at multiple elevations (in the z direction) above the orifice are compared from PIV experiment and CFD simualtion are shown in Figure 5.7. It can be noticed that the velocity profile of the churn flow is generally "flatter" than that of the bubbly flow at the same elevation. Meanwhile, the churn flow has relative larger velocity at the edge of the plume at the same elevation (e.g., the scaled velocity of the bubbly flow is ~0.05 at X=40 mm at the edge of the plume while that of the churn flow between 0.2~0.25 at the same location, see Figure 5.7a). This indicates that the churn flow might entrain more water due to the relative lareger velocity at the plume edge and the above conclusions based on PIV mearuement are consistent with the findings stated in Chapter 4 based on the LES approach. The CFD results generally follows the same pattern and trend as the PIV experiment measurement, however, the scaled velocity at the edge of the plume is relatively smaller comapred with PIV experiment results at the same elevation for a given x value (for example, the scaled velocity of the churn flow at an elevation of z=100 mm is ~0.3 at x=30 mm for the PIV experiment measurement while that for the CFD simualiton is decreased to almost zero. Similary, the scaled velocoty of the bubbly flow at an elevation of z=100 mm is ~0.02 for the PIV experiment measurement while that for the CFD simulation is ~zero). That is possibly because the individiual bubble velocity due to buoyancy at the edge of the plume is not negigible but not accounted for in the CFD simualtion using VOF mothod. The individual bubbles, either from big air blob breaking up as rising up in the churn flow condition or the smaller bubbles in the bubbly flow, accelerates the flow field especially at the edge of the plume.

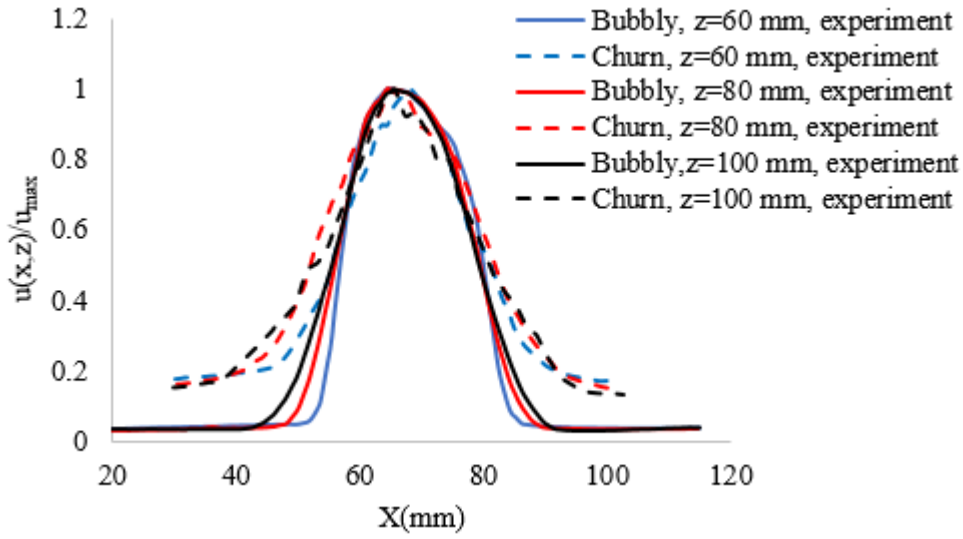

(a)

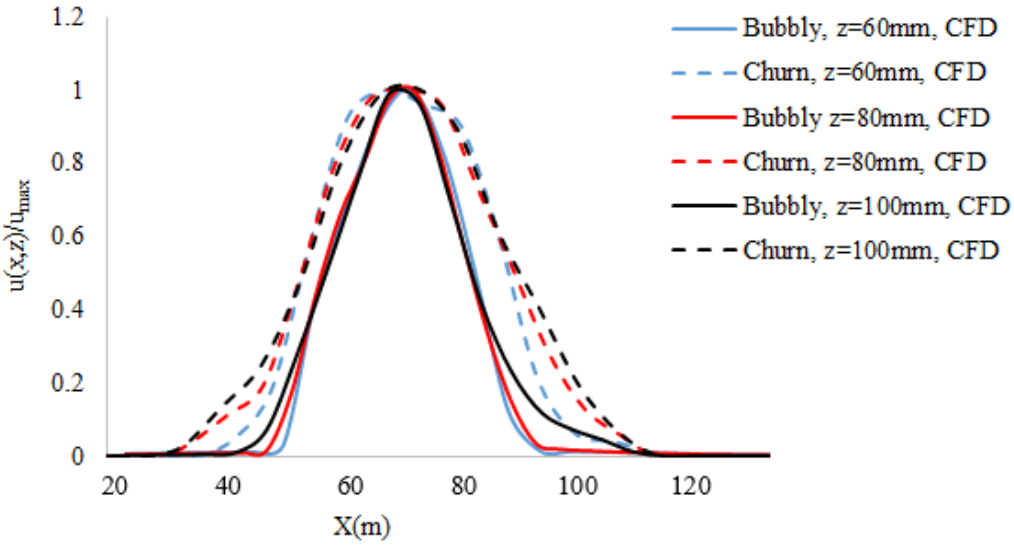

(b)

Figure 5.7 Mean velocity profile of the bubbly and churn flows at multiple elevations (in the z direction) above the orifice (a) PIV experiment (b) CFD simulation. The local flow velocity, u(x,z), is scaled by the maximum velocity at the centerline, u_{max}.

Figure 5.8 shows the instantaneous velocity contours along with vectors at multiple consecutive time levels for the bubbly flow. The main flow has a velocity of ~0.2-0.3 m/s and the red or yellow dots in the velocity contour indicates the rising discrete bubbles whose rising velocity is relatively higher than that of water. The bubbly flow mainly shows

the jet flow behavior and there is no sudden change in flow behavior as the bubbles exit the orifice.

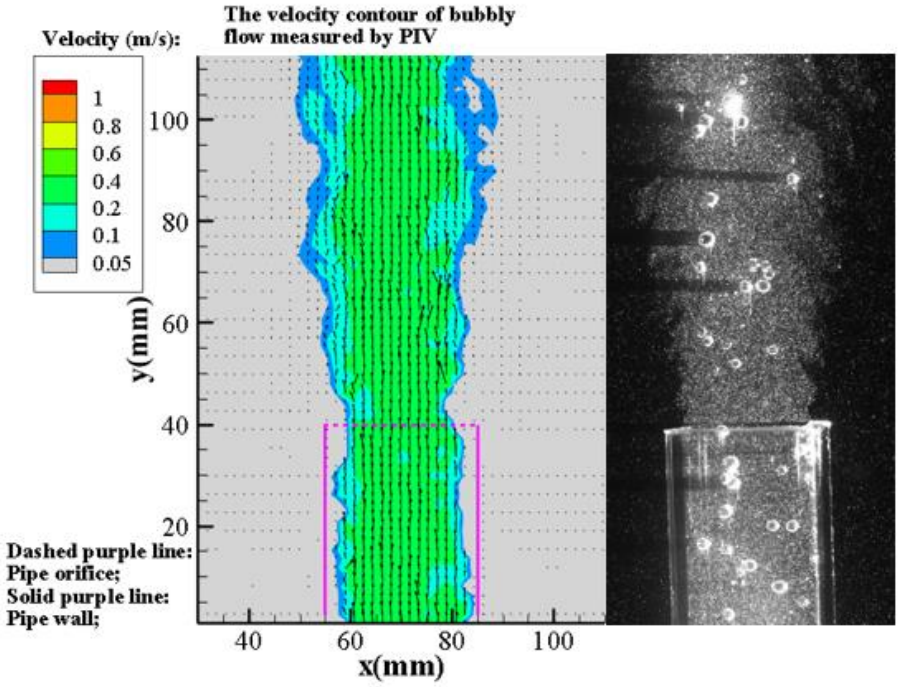

(a)

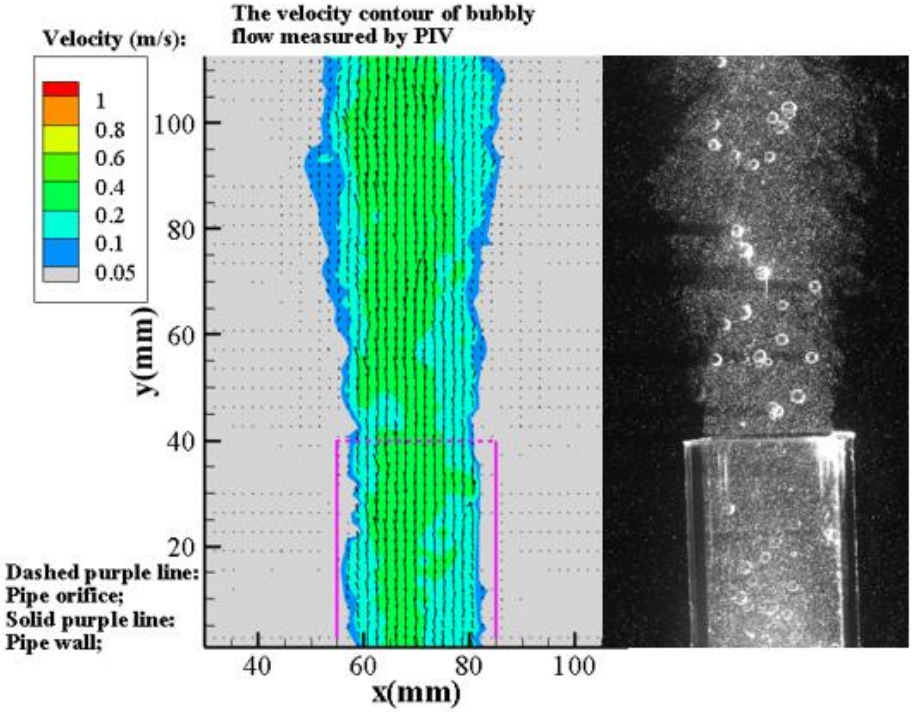

(b)

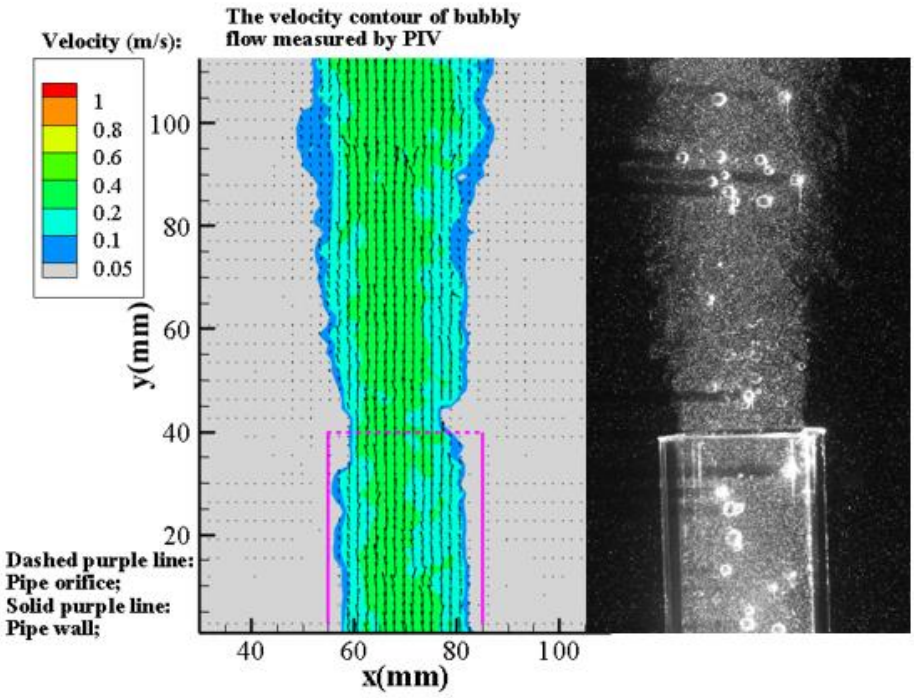

(c)

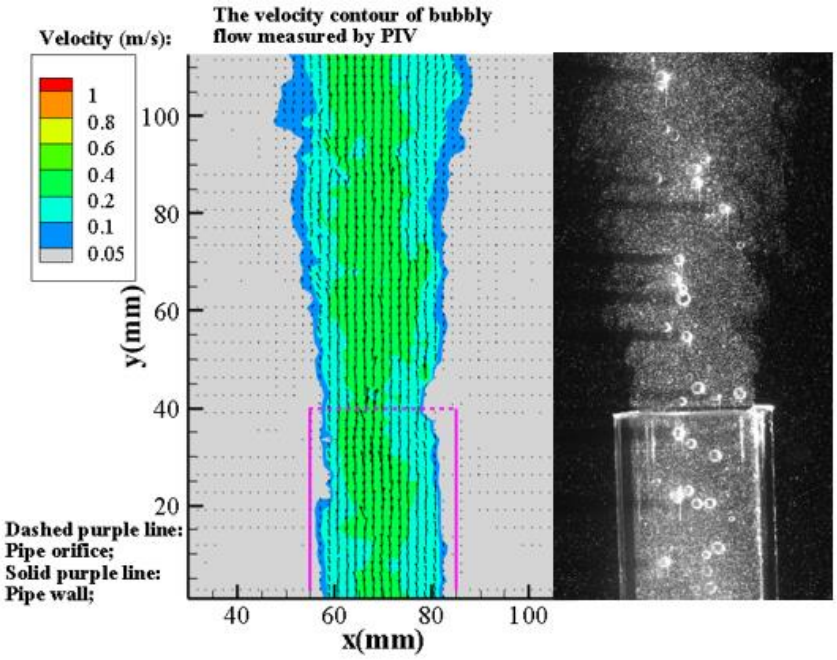

(d)

Figure 5.8 The instantaneous flow velocity of the bubbly flow from the PIV measurement. The left panel is the the velocity contour along with vectors and the right panel is the flow captured by the camera (a) t=0 s (b) t=0.1 s (c) t=0.2 s and (d) t=0.3 s. Figure 5.7a-d indicates five consecutive time levels with an interval of 0.1 s, in which t=0 indicates the start of the sampling.

Figure 5.9 shows the instantaneous velocity contours along with vectors at multiple consecutive time levels for the churn flow. As can be noticed, the flow velocity inside the pipe varies significantly, ranging from ~0.8-1.0 m/s upward to ~1.0 m/s downward with time. This is a typical churn flow behavior in the vertical pipe due to the violently and chaotically interacted air and water. The air evolves as one big air blob at the orifice and expands as it exits the orifice and continues to rise up. The bigger air blob eventually breakup into smaller bubbles at ~2 diameters above the orifice. The behavior of the air bubbles in churn flow periodically appears in the observation captured by the camera (see the right panels in Figure 5.8).

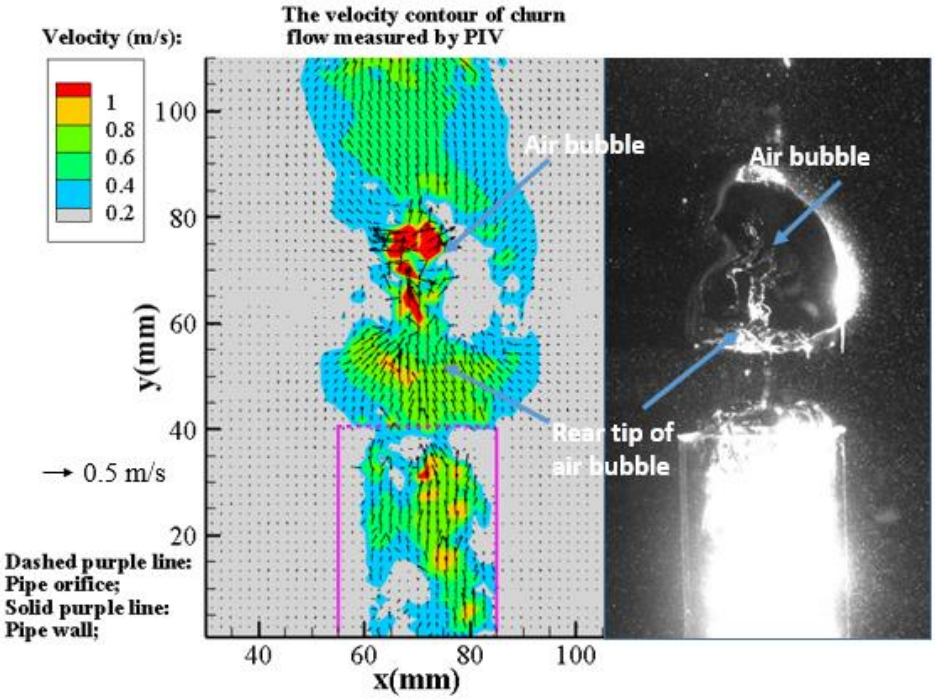
The velocity contour of churn flow measured by PIV
Velocity (m/s):
1
0.8
0.6
0.4
0.2
100
80
60
40
20
y(mm)
40
60
80
100
x(mm)
0.5 m/s
Dashed purple line:
Pipe orifice;
Solid purple line:
Pipe wall;
Air bubble
Air bubble
Rear tip of air bubble

(a)

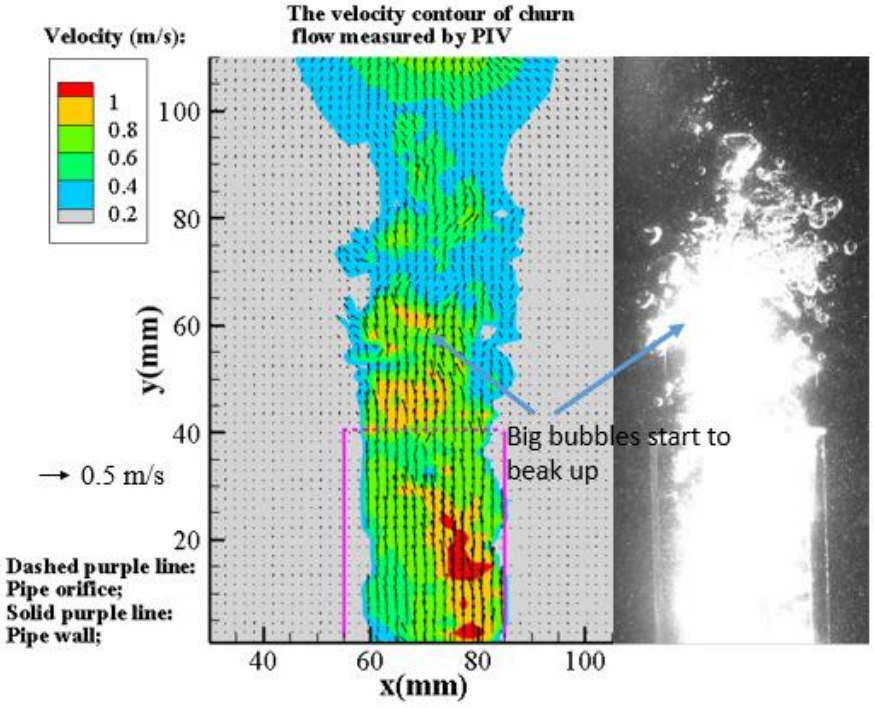
The velocity contour of churn flow measured by PIV
Velocity (m/s):
1
0.8
0.6
0.4
0.2
100
80
60
40
20
y(mm)
40
60
80
100
x(mm)
0.5 m/s
Dashed purple line:
Pipe orifice;
Solid purple line:
Pipe wall;
Big bubbles start to beak up

(b)

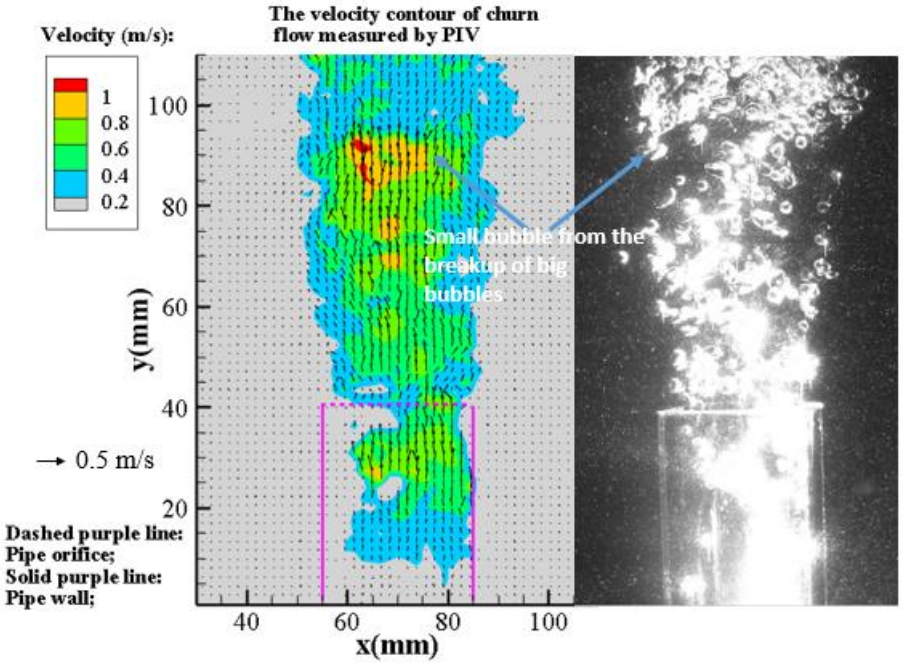

(c)

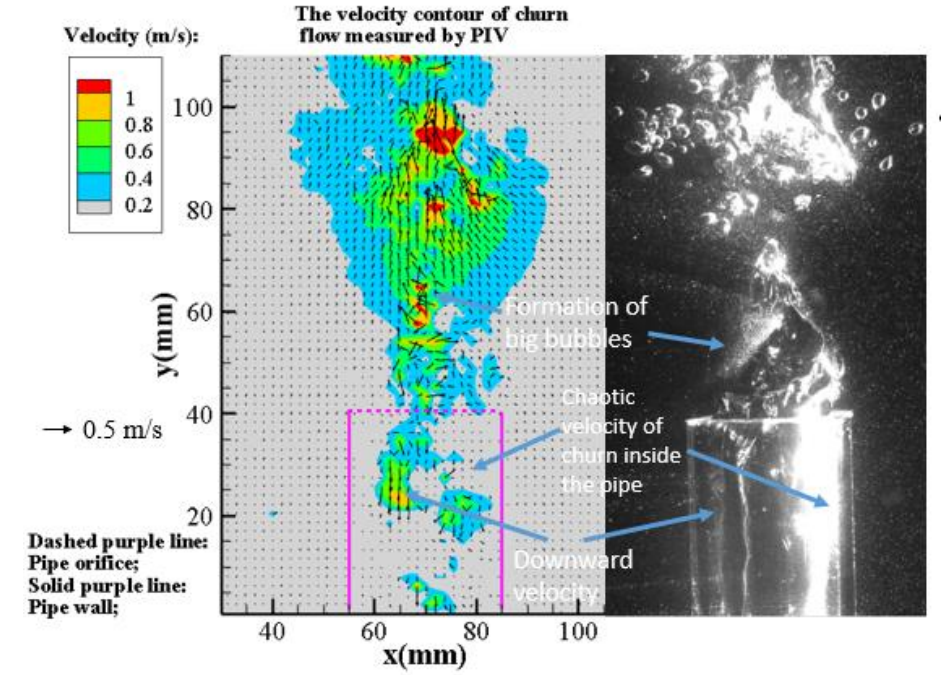

(d)

Figure 5.9 The instantaneous flow velocity of the churn flow from the PIV measurement. The left panel is the the velocity contour along with vectors and the right panel is the flow captured by the camera (a) t=0 s (b) t=0.1 s (c) t=0.2 s and (d) t=0.3 s. Figure 5.8a-d indicates five consecutive time levels with an interval of 0.1 s, in which t=0 indicates the start of the sampling.

5.5 Conclusions

In this chapter, a laboratory scale experiment was conducted for releasing the multiphase flow with air and water by using PIV method. The detailed hydrodynamics characteristics were studied under the bubbly and churn flow conditions. LES approach is simultaneously used to numerically compare with the experimental results obtained from PIV measurement. The main conclusions are summarized in the following aspects:

1. The air forms into discrete small bubbles for the bubbly flow and those air bubbles barely interact with one another while churn flow shows infinite unsteadiness and the air and water violently interacted with each other all the time. For the churn flow, big air blobs are formed at the orifice and then pinched off and rose up in the vertical direction, those big air blobs finally breakup into small air bubbles after a short distance exiting the orifice (~1-2 diameters of the pipe).

2. The half jet angle of the churn jet is larger than that of the bubbly jet, which suggests more entrainment of water from the ambient environment.

3. The velocity profile of the churn flow in the radial direction is generally “flatter” than that of the bubbly flow at the same elevation and the churn flow has relative larger velocity at the edge of the plume at the same elevation, which indicates that the churn flow might entrain more water due to the relative lareger velocity at the plume edge. However, the scaled velocity at the edge of the plume is relatively smaller compared with PIV experiment results at the same elevation for a given x value, which may due to the fact that the individual bubble velocity due to buoyancy at the edge of the plume is not negligible but not accounted for in the CFD simulation using VOF method. The individual bubbles, either from big air blob breaking up as rising up in the churn flow condition or the smaller bubbles in the bubbly flow, accelerates the flow field especially at the edge of the plume.

CHAPTER 6

SUMMARY

The spread angle of oil jet premixed with dispersant, which is close to the spread jet angle of the single phase jet, relatively larger than that of the oil jet without dispersant. The relative larger spread angle of the oil jet with dispersant premixed might be due to the more water entrainment into the oil jet from the ambient environment as dispersant decreases the oil-water interfacial tension.

It is important to predict the spatial distribution of oil droplets of different diameters to allow for the accurate measurement of oil droplet size distribution. Based on the Lagrangian Particle Tracking (LPT) method coupled with CFD data obtained from Chapter 2, larger oil droplets have the larger buoyancy to overcome the turbulence mixing energy while smaller droplets are more likely to be uniformly mixed within the oil plume.

Chapter 4 studies the Deepwater Horizon oil blowout by Large Eddy Simulation (LES), which is a more advanced approach than the one used in Chapter 2. The results show that the churn flow may produce five times of energy loss in comparison to that in bubbly or single phase flow, which indicates the oil discharge rate from the Deepwater Horizon oil blowout might be overestimated by ignoring the churn flow. Furthermore, the axial velocity is more evenly distributed in the churn jet in comparison with the bubbly or single phase jet and the larger entrainment of water and turbulence dissipation rate of the churn jet may result in a smaller droplet size distribution compared to the bubbly jet by conserving the same momentum.

Chapter 5 further supports the findings in Chapter 4 by experimental measurement by Particle Imaging Velocimetry (PIV) and Large Eddy Simulation (LES). Compared with the RANS method used in Chapter 2, LES is a more reliable and accurate method to model the detailed turbulence structure, such as small eddies observed in the experiment, compared to the RANS model.

REFERENCES

ANSYS, 2009, Fluent 12.0 User's Guide, ANSYS, Inc., Lebanon, NH.

Ball, C. G., Fellouah, H., and Pollard, A., 2012, The flow field in turbulent round free jets: Progress in Aerospace Sciences, v. 50, p. 1-26.

Belcaid, A., Le Palec, G., and Draoui, A., 2015, Numerical and experimental study of Boussinesq wall horizontal turbulent jet of fresh water in a static homogeneous environment of salt water: Journal of Hydrodynamics, Ser. B, v. 27, no. 4, p. 604-615.

Birjandi, A. H., and Bibeau, E., 2009, Bubble effects on the Acoustic Doppler Velocimeter (ADV) measurements, no. 43734, p. 27-32.

Birkhoff, G., 1957, Jet, Wakes and cavities, New York, NY, Academic Press, Inc.

Boersma, B. J., Brethouwer, G., and Nieuwstadt, F. T. M., 1998, A numerical investigation on the effect of the inflow conditions on the self-similar region of a round jet: Physics of Fluids, v. 10, no. 4, p. 899-909.

Borghi, R., and Gonzalez, M., 1986, Applications of Lagrangian models to turbulent combustion: Combustion and Flame, v. 63, no. 1, p. 239-250.

Bosanquet, C. H., Horn, G., and Thring, M. W., 1961, The effect of density differences on the path of jets: Proceedings of the Royal Society of London. Series A. Mathematical and Physical Sciences, v. 263, no. 1314, p. 340-352.

Boufadel, M. C., Abdollahi-Nasab, A., Geng, X., Galt, J., and Torlapati, J., 2014, Simulation of the landfall of the Deepwater Horizon oil on the shorelines of the Gulf of Mexico: Environmental Science & Technology, v. 48, no. 16, p. 9496-9505.

Brackbill, J. U., Kothe, D. B., and Zemach, C., 1992, A continuum method for modeling surface tension: Journal of Computational Physics, v. 100, no. 2, p. 335-354.

Brakstad, O. G., Nordtug, T., and Throne-Holst, M., 2015, Biodegradation of dispersed Macondo oil in seawater at low temperature and different oil droplet sizes: Marine Pollution Bulletin, v. 93, no. 1–2, p. 144-152.

Brandvik, P. J., Johansen, Ø., Leirvik, F., Farooq, U., and Daling, P. S., 2013, Droplet breakup in subsurface oil releases – Part 1: Experimental study of droplet breakup and effectiveness of dispersant injection: Marine Pollution Bulletin, v. 73, no. 1, p. 319-326.

Burlutskiy, E., and Turangan, C. K., A computational fluid dynamics study on oil-in-water dispersion in vertical pipe flows: Chemical Engineering Research and Design, v. 93, p. 48-54.

Camilli, R., Di Iorio, D., Bowen, A., Reddy, C. M., Techet, A. H., Yoerger, D. R., Whitcomb, L. L., Seewald, J. S., Sylva, S. P., and Fenwick, J., 2012a, Acoustic measurement of the Deepwater Horizon Macondo well flow rate: Proceedings of the National Academy of Sciences, v. 109, no. 50, p. 20235-20239.

Camilli, 2012b, Acoustic measurement of the Deepwater Horizon Macondo well flow rate: Proceedings of National Academy of Science, v. 109, no. 50, p. 20235-20239.

Carazzo, G., kaminski, E., and Tait, S., 2006, The route to self-similarity in turbulent jets and plumes: Journal of Fluid Mechanics, v. 547, p. 137-148.

Chang, K., Ouellette, N. T., Xu, H., and Bodenschatz, E., Lagrangian particle tracking in high Reynolds number turbulence, Dordrecht, 2007, Springer Netherlands, p. 299-311.

Chapman, H., Purnell, K., Law, R. J., and Kirby, M. F., 2007, The use of chemical dispersants to combat oil spills at sea: A review of practice and research needs in Europe: Marine Pollution Bulletin, v. 54, no. 7, p. 827-838.

Chen, F., and Yapa, P. D., 2003, A model for simulating deep water oil and gas blowouts - Part II: Comparison of numerical simulations with "deepspill" field experiments: Journal of Hydraulic Research, v. 41, no. 4, p. 353-365.

Chen, F., and Yapa, P. D., 2004a, Three-dimensional visualization of multi-phase (oil/gas/hydrate) plumes: Environmental Modeling Software, v. 19, p. 751-760.

Chen, F., and Yapa, P. D., 2004b, Three-dimensional visualization of multi-phase (oil/gas/hydrate) plumes: Environmental Modelling and Software, v. 19, no. 7, p. 751-760.

Chen, H., An, W., You, Y., Lei, F., Zhao, Y., and Li, J., 2015, Numerical study of underwater fate of oil spilled from deepwater blowout: Ocean Engineering, v. 110, Part A, p. 227-243.

Cheung, V., and Lee, J. H. W., 1990, Generalized Lagrangian model for buoyant jets in current: Journal of Environmental Engineering, v. 116, no. 6, p. 1085-1106.

Deshpande, S. S., Trujillo, M. F., Wu, X., and Chahine, G., 2012, Computational and experimental characterization of a liquid jet plunging into a quiescent pool at shallow inclination: International Journal of Heat and Fluid Flow, v. 34, p. 1-14.

Dimou, K., 3D hybrid Eulerian-Lagrangian / particle tracking model for simulating mass transport in coastal water bodies, Ph.D.: Massachusetts Institute of Technology.

Ding, D., Benson, D. A., Paster, A., and Bolster, D., 2013, Modeling bimolecular reactions and transport in porous media via particle tracking: Advances in Water Resources, v. 53, p. 56-65.

El-Amin, M. F., Sun, S., and Salam, A., 2014, Simulation of buoyancy-induced turbulent flow from a hot horizontal jet: Journal of Hydrodynamics, Ser. B, v. 26, no. 1, p. 104-113.

Fabregat, A., Dewar, W. K., Özgökmen, T. M., Poje, A. C., and Wienders, N., 2015, Numerical simulations of turbulent thermal, bubble and hybrid plumes: Ocean Modelling, v. 90, p. 16-28.

Fabregat Tomàs, A., Poje, A. C., Özgökmen, T. M., and Dewar, W. K., 2016, Dynamics of multiphase turbulent plumes with hybrid buoyancy sources in stratified environments: Physics of Fluids, v. 28, no. 9, p. 095109.

Falcone, A. M., and Cataldo, J. C., 2003, Entrainment velocity in an axisymmetric turbulent jet: Journal of Fluids Engineering, v. 125, no. 4, p. 620-627.

Fischer, H., List, E., Koh, R., and Imberger, J., 1979, Mixing in inland and coastal waters, New York, Academic Press.

Francois, M., and Sicilian, J., 2007, Modeling interfacial surface tension in fluid flow, Oak Ridge National Laboratory.

Friehe, C., Van Atta, C., and Gibson, C., 1971, Jet turbulence: dissipation rate measurementa and correlations.

FRTG, Assessment of flow rate estimates for the Deepwater Horizon/Macondo well oil spill, Washington, DC, 2011, U.S. Department of the Interior.

Fuller, C., Bonner, J., Page, C., Ernest, A., McDonald, T., and McDonald, S., 2004, Comparative toxicity of oil, dispersant, and oil plus dispersant to several marine species: Environmental Toxicology and Chemistry, v. 23, no. 12, p. 2941-2949.

Geng, X., Boufadel, M. C., Ozgokmen, T., King, T., Lee, K., Lu, Y., and Zhao, L., 2016, Oil droplets transport due to irregular waves: Development of large-scale spreading coefficients: Marine Pollution Bulletin, v. 104, no. 1, p. 279-289.

Geng, X., Boufadel, M. C., Xia, Y., Li, H., Zhao, L., Jackson, N. L., and Miller, R. S., 2014, Numerical study of wave effects on groundwater flow and solute transport in a laboratory beach: Journal of Contaminant Hydrology, v. 165, p. 37-52.

Georgiadis, N. J., Rizzetta, D. P., and Fureby, C., 2010, Large-Eddy Simulation: current capabilities, recommended practices, and future research: AIAA Journal, v. 48, no. 8, p. 1772-1784.

Ghoniem, A. F., Zhang, X., Knio, O., Baum, H. R., and Rehm, R. G., 1993, Dispersion and deposition of smoke plumes generated in massive fires: Journal of Hazardous Materials, v. 33, p. 275-293.

Gopalan, B., and Katz, J., 2010, Turbulent shearing of crude oil mixed with dispersants generates long microthreads and microdroplets: Physical review letters, v. 104, no. 5, p. 054501.

Gorokhovski, M., and Herrmann, M., 2008, Modeling primary atomization: Annual Review of Fluid Mechanics., v. 40, p. 343-366.

Gros, J., Socolofsky, S. A., Dissanayake, A. L., Zhao, L., Boufadel , M. C., Reddy, C. M., and Arey, J. S., 2017, Petroleum dynamics in a the sea and influence on subsea dispersant injection during Deepwater Horizon: Proceedings of National Academy Science, in press.

Haan, P., 1999, On the use of density kernels for concentration estimations within particle and puff dispersion models: Atmospheric Environment, v. 33, no. 13, p. 2007-2021.

Hargreaves, D. M., Scase, M. M., and Evans, I., 2012, A simplified computational analysis of turbulent plumes and jets: Environmental Fluid Mechanics, v. 12, no. 6, p. 555-578.

Hirt, C. W., and Nichols, B. D., 1981, Volume of fluid (VOF) method for the dynamics of free boundaries: Journal of Computer Physics., v. 39, no. 1, p. 201-225.

Horn, G., and Thring, M. W., 1956, Angle of spread of free jets: Nature, v. 178, no. 4526, p. 205-206.

Houghtalen, R. J., Osman, A., and Hwang, N. H., 2016, Fundamentals of hydraulic engineering systems, Prentice Hall.

Hunt, C. D., Mansfield, A. D., Mickelson, M. J., Albro, C. S., Geyer, W. R., and Roberts, P. J. W., 2010, Plume tracking and dilution of effluent from the Boston sewage outfall: Marine Environmental Research, v. 70, no. 2, p. 150-161.

Iguchi, M., Okita, K., Nakatani, T., and Kasai, N., 1997, Structure of turbulent round bubbling jet generated by premixed gas and liquid injection: International Journal of Multiphase Flow, v. 23, no. 2, p. 249-262.

Iguchi, M., Ueda, H., and Uemura, T., 1995, Bubble and liquid flow characteristics in a vertical bubbling jet: International Journal of Multiphase Flow, v. 21, no. 5, p. 861-873.

Iguchi, M., Yamamoto, F., Uemura, T., and Morita, Z.-i., 1992, Multiphase Flows in Ironmaking and Steelmaking Processes: Japanese Journal of Multiphase Flow, v. 6, no. 1, p. 54-64.

Iqbal, M. O., and Thomas, F. O., 2007, Coherent structure in a turbulent jet via a vector implementation of the proper orthogonal decomposition: Journal of Fluid Mechenics, v. 571, p. 281-326.

ITOPF, 2014, Fate of marine oil spills, The International Tank Owners Pollution Federation Limited.

J.H.W. Lee, V. H. C., 2012, Turbulent Jets and Plumes, Kluwer Academic Publishers.

Jiang, Y., Guo, J., and Al-Dahhan, M. H., 2005, Multiphase flow packed-bed reactor modeling: combining CFD and cell network model: Industrial & Engineering Chemistry Research, v. 44, no. 14, p. 4940-4948.

Joao Pinto, Y. F., Luis Oliveira, Christian Tenaud, 2010, Numerical simulaiton of a two-phase flow in an oil filter couplilng a LES approach with a Lagrangian particle tracking V European Conference on Computational Fluid Dynamics ECCOMAS CFD 2010: Lisbon, Portugal.

Johansen, O., 2000, DeepBlow - a Lagrangian Plume model for deep water blowouts,

Spill Science and Technology Bulletin, v. 6, no. 2, p. 103-111.

Johansen, Ø., 2003, Development and verification of deep-water blowout models: Marine Pollution Bulletin, v. 47, no. 9, p. 360-368.

Johansen, Ø., Brandvik, P. J., and Farooq, U., 2013, Droplet breakup in subsea oil releases – Part 2: Predictions of droplet size distributions with and without injection of chemical dispersants: Marine Pollution Bulletin, v. 73, p. 327-335.

John C. Crittenden, R. R. T., David W. Hand, Kerry J. Howe and George Tchobanoglous, 2012, MWH's Water Treatment: Principles and Design, John Wiley & Sons, Inc.

Kaku, V. J., Boufadel, M. C., and Venosa, A. D., 2006, Evaluation of mixing energy in laboratory flasks used for dispersant effectiveness testing: Journal of Environmental Engineering, v. 132, no. 1, p. 93-101.

Korotenko, K. A., Mamedov, R. M., Kontar, A. E., and Korotenko, L. A., 2004, Particle tracking method in the approach for prediction of oil slick transport in the sea: modelling oil pollution resulting from river input: Journal of Marine Systems, v. 48, no. 1-4, p. 159-170.

Kotsovinos, 1975, A study of the entrainment and turbulence in a plane bouyant jet: California Institute of Technology.

Kresta, S. M., Wood, P. E., 1993, The flow field produced by a pitched blade turbine: Characterization of the turbulence and estimation of the dissipation rate: Chemical Engineering Science, v. 48, no. 10, p. 1761–1774.

Kumar, R., and Dewan, A., 2014, URANS computations with buoyancy corrected turbulence models for turbulent thermal plume: International Journal of Heat and Mass Transfer, v. 72, p. 680-689.

Laborde-Boutet, C., Larachi, F., Dromard, N., Delsart, O., and Schweich, D., 2009, CFD simulation of bubble column flows: Investigations on turbulence models in RANS approach: Chemical Engineering Science, v. 64, no. 21, p. 4399-4413.

Lee, H. W., and Chu, J., 2003, Turbulent Jets and Plumes, Massachusetts, USA, Kluwer Academic Publishers.

Leifer, I., Solomon, E., Schneider v. Deimling, J., Coffin, R., Rehder, G., and Linke, P., 2015, The fate of bubbles in a large, intense bubble plume for stratified and unstratified water: Numerical simulations of 22/4b expedition field data: Journal of Marine and Petroleum Geology, v. 68B, p. 806-823.

Leitch, A. M., and Baines, W. D., 1989, Liquid volume flux in a weak bubble plume: Journal of Fluid Mechanics, v. 205, p. 77-98.

Lessard, R. R., and DeMarco, G., 2000, The significance of oil spill dispersants: Spill Science and Technology Bulletin, v. 6, no. 1, p. 59-68.

Lima Neto, I. E., Zhu, D. Z., and Rajaratnam, N., 2008, Bubbly jets in stagnant water: International Journal of Multiphase Flow, v. 34, no. 12, p. 1130-1141.

Liu, Z., and Reitz, R. D., 1997, An analysis of the distortion and breakup mechanisms of high speed liquid drops: International Journal of Multiphase Flow, v. 23, no. 4, p. 631-650.

Lomas, C., 2011, Fundamentals of hot wire anemometry, Cambridge University Press.

Lucas, D., Prasser, H. M., and Manera, A., 2005, Influence of the lift force on the stability of a bubble column: Chemical Engineering Science, v. 60, no. 13, p. 3609-3619.

MacDonald, I. R., Leifer, I., Sassen, R., Stine, P., Mitchell, R., and Guinasso, N., 2002, Transfer of hydrocarbons from natural seeps to the water column and atmosphere: Geofluids, v. 2, no. 2, p. 95-107.

Manzar Sattarin, H. M., Mahmoud Bayata, Mohammad Teymori, 2007, New viscosity correlations for dead crude oils: Petroleum and Coal, v. 49, no. 2, p. 33-39.

Marianne M. Francois, J. M. S., 2007, Modeling interfacial surface tension in fluid flow: Oak Ridge National Laboratory.

McNutt, M., Camilli, R., Guthrie, G., Hsieh, P., Labson, V., Lehr, B., Maclay, D., Ratzel, A., and Sogge, M., 2011, Assessment of flow rate estimates for the Deepwater Horizon/Macondo well oil spill, Flow Rate Technical Group report to the National Incident Command, Interagency Solutions Group, March 10, 2011.

McNutt, M. K., Camilli, R., Crone, T. J., Guthrie, G. D., Hsieh, P. A., Ryerson, T. B., Savas, O., and Shaffer, F., 2012, Review of flow rate estimates of the Deepwater Horizon oil spill: Proceedings of National Academy of Science, v. 109, no. 50, p. 20260-20267.

Milgram, J. H., 1983, Mean flow in round bubble plumes: Journal of Fluid Mechanics, v. 133, p. 345-376.

Miller, R. S., Harstad, K., and Bellan, J., 1998, Evaluation of equilibrium and non-equilibrium evaporation models for many-droplet gas-liquid flow simulations: International Journal of Multiphase Flow, v. 24, no. 6, p. 1025-1055.

Montoya, G., Liao, Y., Lucas, D., and Krepper, E., Analysis and applications of a two-fluid multi-field hydrodynamic model for churn-turbulent flows, Proceedings 2013 21st International Conference on Nuclear Engineering2013, American Society of Mechanical Engineers, p. V006T016A033-V006T016A033.

Montoya, G., Lucas, D., Baglietto, E., and Liao, Y., 2016, A review on mechanisms and models for the churn-turbulent flow regime: Chemical Engineering Science, v. 141, p. 86-103.

Murphy, D. W., Li, C., d'Albignac, V., Morra, D., and Katz, J., 2015, Splash behaviour and oily marine aerosol production by raindrops impacting oil slicks: Journal of Fluid Mechanics, v. 780, p. 536-577.

Murphy, D. W., Xue, X., Sampath, K., and Katz, J., 2016, Crude oil jets in crossflow: Effects of dispersant concentration on plume behavior: Journal of Geophysical Research: Oceans, v. 121, no. 6, p. 4264-4281.

Nauw, J., Linke, P., and Leifer, I., 2015, Bubble momentum plume as a possible mechanism for an early breakdown of the seasonal stratification in the northern North Sea: Journal of Marine and Petroleum Geology, v. 68, p. 789-805.

Neto, I. E. L., Zhu, D. Z., and Rajaratnam, N., 2008, Effect of Tank Size and Geometry on the Flow Induced by Circular Bubble Plumes and Water Jets: Journal of Hydraulic Engineering, v. 134, no. 6, p. 833-842.

New, T. H., Lim, T. T., and Luo, S. C., 2006, Effects of jet velocity profiles on a round jet in cross-flow: Experiments in Fluids, v. 40, no. 6, p. 859-875.

Nguyen, T. H. T., Ku, H., Hwang, J. H., and Jang, D., 2016, The multiphase flow simulations of CO2 plume and jet under the background current: KSCE Journal of Civil Engineering, v. 20, no. 6, p. 2569-2577.

Norman, T. L., and Revankar, S. T., 2010, Jet-plume condensation of steam–air mixtures in subcooled water, Part 1: Experiments: Nuclear Engineering and Design, v. 240, no. 3, p. 524-532.

North, E. W., Adams, E. E., Sherwood, C. R., He, R., Hyun, K. H., Socolofsky, S. A., and Schlag, Z., 2011, Simulating oil droplet dispersal from the Deepwater Horizon spill with a Lagrangian approach.

NRC, 1989, Using Oil Spill Dispersants on the Sea: Washington, D.C., National Academy Press.

NRC, 2003, Oil in the sea III: inputs, fates, and effects, National Research Council, National Academies Press: Washington, D.C.

NRC, 2005, Oil Spill Dispersants: Efficacy and effects Washington, DC.

NRC, 2013, An ecosystem approach to accessing the impacts of the Deepwater Horizon Oil Spill in the Gulf of Mexico: National Academies Press, Washington, DC.

Olsen, J. E., and Skjetne, P., 2016, Current understanding of subsea gas release: A review: The Canadian Journal of Chemical Engineering, v. 94, no. 2, p. 209-219.

Than, P., Preziosi, L., Joseph, D., Arney, M., 1988, Measurement of interfacial tension between immiscible liquids with the spinning rod Tensionmeter: Journal of Colloid and Interface Science, v. 124, no. 2, p. 552-559.

Pan, Z., Zhao, L., Boufadel, M. C., King, T., Robinson, B., Conmy, R., and Lee, K., 2017, Impact of mixing time and energy on the dispersion effectiveness and droplets size of oil: Chemosphere, v. 166, p. 246-254.

Parsi, M., Vieira, R. E., Torres, C. F., Kesana, N. R., McLaury, B. S., Shirazi, S. A., Schleicher, E., and Hampel, U., 2015, Experimental investigation of interfacial structures within churn flow using a dual wire-mesh sensor: Int. J. Multiphase Flow, v. 73, p. 155-170.

Pezeshki, S. R., Hester, M. W., Lin, Q., and Nyman, J. A., 2000, The effects of oil spill and clean-up on dominant US Gulf coast marsh macrophytes: a review: Environmental Pollution, v. 108, no. 2, p. 129-139.

Picano, F., and Casciola, C. M., 2007, Small-scale isotropy and universality of axisymmetric jets: Physics of Fluids, v. 19, no. 11, p. 118106.

PlumeCalculationTeam, 2010, Deepwater Horizon release estimate of rate by PIV.

Poole, B., and Hall, J. W., 2014, Turbulence measurements in the corner wall jet: Proc. ASME Int. Mech. Eng. Congr. Expo, 2014, no. 46545, p. V007T009A092.

Pope, S., 2000, Turbulent Flows, Cambridge University Press.

Rahai, H. R., and Wong, T. W., 2002, Velocity field characteristics of turbulent jets from round tubes with coil inserts: Applied Thermal Engineering, v. 22, no. 9, p. 1037-1045.

Ramseur, J. L., 2010, Deepwater Horizon Oil Spill: The Fate of the Oil Congressional Research Service.

Rathore, S. K., and Das, M. K., 2016, Numerical investigation on the performance of low-Reynolds number model for a buoyancy-opposed wall jet flow: International Journal of Heat and Mass Transfer, v. 95, p. 636-649.

Reddy, C. M., Arey, J. S., Seewald, J. S., Sylva, S. P., Lemkau, K. L., Nelson, R. K., Carmichael, C. A., McIntyre, C. P., Fenwick, J., Ventura, G. T., Van Mooy, B. A. S., and Camilli, R., 2012, Composition and fate of gas and oil released to the water column during the Deepwater Horizon oil spill: Proceedings of the National Academy of Sciences, v. 109, no. 50, p. 20229-20234.

Reed, M., Johansen, Ø., Brandvik, P. J., Daling, P., Lewis, A., Fiocco, R., Mackay, D., and Prentki, R., 1999, Oil Spill Modeling towards the Close of the 20th Century: Overview of the State of the Art: Spill Science & Technology Bulletin, v. 5, no. 1, p. 3-16.

Rensen, J., Luther, S., and Lohse, D., 2005, The effect of bubbles on developed turbulence: Journal of Fluid Mechanics, v. 538, p. 153-187.

Richard, J.-B., Thomson, J., Polagye, B., and Bard, J., 2013, Method for identification of Doppler noise levels in turbulent flow measurements dedicated to tidal energy: International Journal of Marine Energy, v. 3-4, p. 52-64.

Robin, B. C., 2014, Environmental Fluid Mechanics, John Wiley & Sons, Inc.

Rodi, W., 1982, Turbulent Buoyant Jets and Plumes, Germany, Pergamon.

Ruzicka, M. C., 2000, On bubbles rising in line: International Journal of Multiphase Flow, v. 26, no. 7, p. 1141-1181.

Sagaut, P., 2005, Large eddy simulation for incompressible flows, Springer.

Shim, Y. M., Sharma, R. N., and Richards, P. J., 2013, Proper orthogonal decomposition analysis of the flow field in a plane jet: Experimental Thermal Fluid Science, v. 51, p. 37-55.

Shinjo, J., and Umemura, A., 2010, Simulation of liquid jet primary breakup: Dynamics of ligament and droplet formation: International Journal of Multiphase Flow, v. 36, no. 7, p. 513-532.

Sivakumar, S., Sangras, R., and Raghavan, V., 2012, Characteristics of turbulent round jets in its potential core region: International Journal of Mechanical and Mechatronics Engineering, v. 6, no. 1, p. 156-161.

Smith, S. H., and Mungal, M. G., 1998, Mixing, structure and scaling of the jet in crossflow: Journal of Fluid Mechanics, v. 357, p. 83-122.

Spaulding, M. L., 1988, A state-of-the-art review of oil spill trajectory and fate modeling: Oil and Chemical Pollution, v. 4, no. 1, p. 39-55.

Sridhar, G., and Katz, J., 1995, Drag and lift forces on microscopic bubbles entrained by a vortex: Physics of Fluids, v. 7, no. 2, p. 389-399.

Stefano, G. D., Vasilyev, O. V., and Goldstein, D. E., 2008, Localized dynamic kinetic-energy-based models for stochastic coherent adaptive large eddy simulation: Physics of Fluids, v. 20, no. 4, p. 045102.

Suyambazhahan, S., Das, S. K., and Sundararajan, T., 2009, The effect of buoyancy on flow fluctuations for horizontal plane jets in low speed applications: Experimental Thermal and Fluid Science, v. 33, no. 7, p. 1119-1127.

Sykes, R. I., Lewellen, W. S., and Parker, S. F., 1986, On the vorticity dynamics of a turbulent jet in a crossflow: Journal of Fluid Mechanics, v. 168, p. 393-413.

Tomiyama, A., 1998, Struggle with computational bubble dynamics, Third International Conference on Multiphase Flow, ICMF ’98: Lyon, France.

Toschi, F., and Bodenschatz, E., 2009, Lagrangian Properties of Particles in Turbulence: Annual Review of Fluid Mechanics, v. 41, no. 1, p. 375-404.

Valentine, D. L., Mezić, I., Maćešić, S., Črnjarić-Žic, N., Ivić, S., Hogan, P. J., Fonoberov, V. A., and Loire, S., 2012, Dynamic autoinoculation and the microbial ecology of a deep water hydrocarbon irruption: Proceedings of National Academy of Science, v. 109, no. 50, p. 20286-20291.

Versteeg, H. K., and Malalasekera, W., 1996, An Introduction to Computational Fluid Dynamics: The Finite Volume Method Approach, Prentice Hall.

Wang, Z., DiMarco, S. F., and Socolofsky, S. A., 2016, Turbulence measurements in the northern gulf of Mexico: Application to the Deepwater Horizon oil spill on droplet dynamics: Deep Sea Research Part I: Oceanographic Research Papers, v. 109, p. 40-50.

Weisman, J., 1983, Two-phase flow patterns, Handbook of fluidsin motion, Ann Arbor Science, p. 409-425.

Westerwheel, J., M., P. J., and Hunt, J. C. R., 2009, Momentum and scalar transport at the turbulent/non-turbulent interface of a jet: Journal of Fluid Mechanics, v. 631, p. 199-230.

Wu, H., Patterson, G. K., and Van Doorn, M., 1989, Distribution of turbulence energy dissipation rates in a Rushton turbine stirred mixer: Experiments in Fluids, v. 8, no. 3, p. 153-160.

Wygnanski, I., and Fiedler, H. E., 1969, Some measurements in the self-preserving jet: Journal of Fluid Mechanics, v. 38, p. 577-612.

Xiao, F., Dianat, M., and McGuirk, J. J., 2014, LES of turbulent liquid jet primary breakup in turbulent coaxial air flow: International Journal of Multiphase Flow, v. 60, p. 103-118.

Yamashita, H., Kushida, G., and Takeno, T., 1996, An experimental study on the transition and mixing process in a coaxial jet, Atlas of Visualization, CRC Press.

Yan, Z., and Holmstedt, G., 1999, A two-equation turbulence model and its application to a buoyant diffusion flame: International Journal of Heat and Mass Transfer, v. 42, no. 7, p. 1305-1315.

Yapa, B. P. D., Dasanayaka, L. K., Bandara, U. C., and Nakata, K., Modeling the impact of an accidental release of methane gas in deepwater, Proceedings OCEANS 200815-18 Sept. 2008 2008, p. 1-10.

Zare, S., Jamalkhoo, M. H., and Passandideh-Fard, M., 2018, Experimental study of direct contact condensation of steam jet in water flow in a vertical pipe with square cross section: International Journal of Multiphase Flow, v. 104, p. 74-88.

Zhao, L., Boufadel, M. C., Adams, E., Socolofsky, S. A., King, T., Lee, K., and Nedwed, T., 2015, Simulation of scenarios of oil droplet formation from the Deepwater Horizon blowout: Marine Pollution Bulletin, v. 101, no. 1, p. 304-319.

Zhao, L., Boufadel, M. C., King, T., Robinson, B., Gao, F., Socolofsky, S. A., and Lee, K., 2017a, Droplet and bubble formation of combined oil and gas releases in subsea blowouts: Marine Pollution Bulletin, v. 120, no. 1, p. 203-216.

Zhao, 2017b, Droplet and bubble formation of combined oil and gas releases in subsea blowouts: Marine Pollution Bulletin v. 120, no. 1, p. 203-216.

Zhao, L., Boufadel, M. C., Socolofsky, S. A., Adams, E., King, T., and Lee, K., 2014, Evolution of droplets in subsea oil and gas blowouts: Development and validation of the numerical model VDROP-J: Marine Pollution Bulletin, v. 83, no. 1, p. 58-69.

Zhao, L., Gao, F., Boufadel, M., King, T., Robinson, B., Lee, K., and Conmy, R., 2017c, Oil jet with dispersant: Macro-scale hydrodynamics and tip streaming: AIChE Journal, v. 63, no. 11, p. 5222-5234.

Zhao, L., Shaffer, F., Robinson, B., King, T., D'Ambrose, C., Pan, Z., Gao, F., Miller, R. S., Conmy, R. N., and Boufadel, M. C., 2016a, Underwater oil jet: Hydrodynamics and droplet size distribution: Chemical Engineering Journal, v. 299, p. 292-303.

Zhao, 2016b, Underwater oil jet: Hydrodynamics and droplet size distribution: Chemecal Engineering Journal, v. 299, p. 292-303.

Zheng, L., Yapa, P. D., and Chen, F., 2003, A model for simulating deepwater oil and gas blowouts - Part I: Theory and model formulation: Journal of Hydraulic Research, v. 41, no. 4, p. 339-351.